Dissertation
submitted to the
Combined Faculties for the Natural Sciences and for Mathematics
of the Ruperto-Carola University of Heidelberg, Germany
for the degree of
Doctor of Natural Sciences

Put forward by

Diplom-Physiker: **Mark Heisel**

Born in: **Hamburg**

Oral examination: April 13, 2011

LArGe

—

A liquid argon scintillation veto for GERDA

Referees: **Prof. Dr. Wolfgang Hampel**
Prof. Dr. Wolfgang Krätschmer

Zusammenfassung

LArGe
Ein Flüssigargon-Szintillationsveto
für GERDA

LArGe ist ein GERDA low-background Teststand zur Entwicklung neuartiger Methoden der Untergrundunterdrückung für einen möglichen Einsatz in GERDA. GERDA sucht nach dem neutrinolosen Doppelbetazerfall in ^{76}Ge, und verwendet dazu nackte Germaniumdetektoren in 65 m^3 flüssigem Argon. Auf vergleichbare Weise betreibt LArGe Ge-Detektoren in 1 m^3 (1.4 Tonnen) flüssigem Argon, welches zusätzlich mit Photomultipliern zum Nachweis von Szintillationslicht instrumentiert ist. Das Licht wird in Antikoinzidenz mit den Ge-Detektoren dazu verwendet, jene Untergrundereignisse effektiv zu unterdrücken, die Energie im flüssigen Argon deponieren. Die Arbeit behandelt die Entwicklung, den Aufbau und den Testbetrieb von LArGe. Die Effizienz der Untergrundunterdrückung wurde zusammen mit einer Pulsformdiskriminationstechnik (PSD) für verschiedene Quellen untersucht, die charakteristische Untergrundbeiträge von GERDA repräsentieren. Unterdrückungsfaktoren von einigen 10^3 wurden erreicht. Erste Daten einer Untergrundmessung in LArGe (ohne PSD) ergaben einen Untergrundindex von (0.12-4.6)$\cdot 10^{-2}$ cts/(keV$\cdot$kg$\cdot$y) (90% c.l.), was im Bereich der Designvorgabe von GERDA Phase I liegt. Weiterhin wurde zum ersten Mal die natürliche ^{42}Ar Konzentration gemessen (parallel zu GERDA), und es gibt Hinweise auf den $2\nu\beta\beta$-Zerfall in natürlichem Germanium.

Abstract

LArGe
A liquid argon scintillation veto
for GERDA

LArGe is a GERDA low-background test facility to study novel background suppression methods in a low-background environment, for possible applications in the GERDA experiment. GERDA searches for the neutrinoless double-beta decay in ^{76}Ge, by operating naked germanium detectors submersed into 65 m^3 of liquid argon. Similarly, LArGe runs Ge-detectors in 1 m^3 (1.4 tons) of liquid argon, which in addition is instrumented with photo multipliers to detect argon scintillation light. The light is used in anti-coincidence with the germanium detectors, to effectively suppress background events that deposit energy in the liquid argon. This work adresses the design, construction, and commissioning of LArGe. The background suppression efficiency has been studied in combination with a pulse shape discrimination (PSD) technique for various sources, which represent characteristic backgrounds to GERDA. Suppression factors of a few times 10^3 have been achieved. First background data of LArGe (without PSD) yield a background index of (0.12-4.6)$\cdot 10^{-2}$ cts/(keV$\cdot$kg$\cdot$y) (90% c.l.), which is at the level of the GERDA phase I design goal. Furthermore, for the first time we measure the natural ^{42}Ar abundance (in parallel to GERDA), and have indication for the $2\nu\beta\beta$-decay in natural germanium.

in Erinnerung
an meinen lieben Vater
—
Jürgen Heisel

Contents

Chapter 1

Introduction

This work is about the construction and measurements of the LArGe setup, which is a test facility of the GERDA experiment. To provide context for the experimental efforts, a brief résumé of neutrino physics and the GERDA experiment shall be given here. The introduction concludes with the motivation for the LArGe project.

1.1 Neutrino physics

The neutrino was first postulated 1930 by W. Pauli to save the energy-momentum conservation of the nuclear β-decay, and was later given its name by E. Fermi. The experimental discovery came not less than 26 years later, 1956, due to the small cross section of the neutrino. It was made by F. Reines and C. Cowan, who detected anti-neutrinos from nuclear reactors via the induced $p(\overline{\nu}, \mathrm{e}^+)n$ reaction in the Savannah River experiment [1].

In the standard model of particle physics the neutrinos are postulated as massless leptons, which only interact via the weak force. Neutrinos appear in three different flavors (e, μ, τ), by which they are associated with the corresponding charged lepton. According to the standard model, the overall lepton number and the lepton number within each flavor family are conserved.

1.1.1 Neutrino oscillation and masses

First evidence that the description of neutrinos in the standard model is incomplete, came up with the emergence of the 'solar neutrino problem' in 1970: the Homestake Chlorine Detector measured a deficit in the solar neutrino flux [2], compared to predictions from the standard solar model [3, 4]. Subsequently, the observation was strengthened by Kamiokande [5], and other solar neutrino experiments, that measured the flux of solar pp-neutrinos (Gallex [6], Gno [7], Sage [8]). Kamiokande, along with the IMB [9] and Soudan-2 [10] experiments, also found similar discrepancies in the atmospheric neutrino flux, which can be calculated from cosmic ray interactions in the earth's atmosphere.

The problem was resolved as more and more evidence confirmed *neutrino flavor oscillations*, a theory proposed by B. Pontecorvo in 1957 [11]. Neutrino flavor changes can occur on different characteristic length scales: the SNO experiment showed the 'disappearance' of *solar*

electron neutrinos by measuring their flux via charged-current interactions, while simultaneously confirming the predicted total solar neutrino flux via neutral-current measurements [12]. Evidence for *atmospheric* neutrino oscillations came from Super-Kamiokande, which showed an asymmetry between upward and downward atmospheric neutrinos [13]. And ultimately, further confirmation was obtained from the reactor neutrino experiment KamLAND [14], and the accelerator experiments K2K [15] and MINOS [16].

Neutrino oscillations require that neutrinos have masses >0, which evokes an extension of the standard model. Then, in analogy to quark mixing, a given flavor eigenstate $|\nu_l\rangle$ ($l = e, \mu, \tau$) can be described as a linear superposition of mass eigenstates $|\nu_i\rangle$ ($l = 1, 2, 3$), and vice versa. Their interrelation is given by the unitary Pontecorvo-Maki-Nakagawa-Sakata (PMNS, [17]) mixing matrix U_{li}:

$$|\nu_l\rangle = \sum_i U_{li} |\nu_i\rangle$$

Standard model neutrino interactions happen only via their flavor eigenstates. Therefore, when a neutrino is created or absorbed, it is in a flavor eigenstate and has a particular energy E. When propagating, the different mass eigenstates (with masses m_i) travel at different velocities, which leads to a *phase difference* related to the travelled distance L:

$$m_i^2 \frac{L}{2E}$$

If the neutrino is finally detected, the superposition of mass eigenstates has evolved and may collapse into a different flavor eigenstate than the neutrino had at its creation. The probability for such a flavor transition (oscillation) is given by

$$|\langle \nu_\beta | \nu_\alpha \rangle|^2 = \sum_i U^*_{\alpha i} e^{-i m_i^2 \frac{L}{2E}} U_{\beta i}$$

When neutrinos propagate through matter, the flavor oscillation probability can be enhanced by the Mikheyev-Smirnov-Wolfenstein (MSW) effect [18, 19]. The reason is that (only) electron neutrinos can interact with matter via the charged current, which changes their propagation compared to other flavors, and thereby effects their oscillation probability.

The combined results of the neutrino oscillation experiments have determined some of the parameters of the PMNS matrix. In particular known are the squared mass differences Δm^2_{12}, $|\Delta m^2_{23}|$, and the mixing angles Θ_{12} and Θ_{23}. So far, for Θ_{13} there is only an upper limit from the CHOOZ experiment [20]. The CP-violating phase[1] remains unknown.

Neutrino oscillation experiments are only sensitive to mass differences, but can not access the absolut mass scale, nor the mass hierachy. The mass eigenstates can either be in *normal* hierachy ($m_1 < m_2 < m_3$), or in *inverted* hierachy ($m_3 < m_1 < m_2$). In the special case, that the mass of the lightest neutrino is large compared to the mass differences, the two hierachies are *degenerate*. For the lighest neutrino mass there is an upper limit from the tritium-β-decay experiments Mainz [21] and Troisk [22], $m_0 \leq 2.3$ eV. And an upper bound on the sum of neutrino masses can be deduced from cosmology, $m_{\Sigma i} \leq (0.5-1.7)$ eV [23, 24].

[1] there is one CP-violating phase if neutrinos are Dirac particles (standard model), and three phases if neutrinos are Majorana particles.

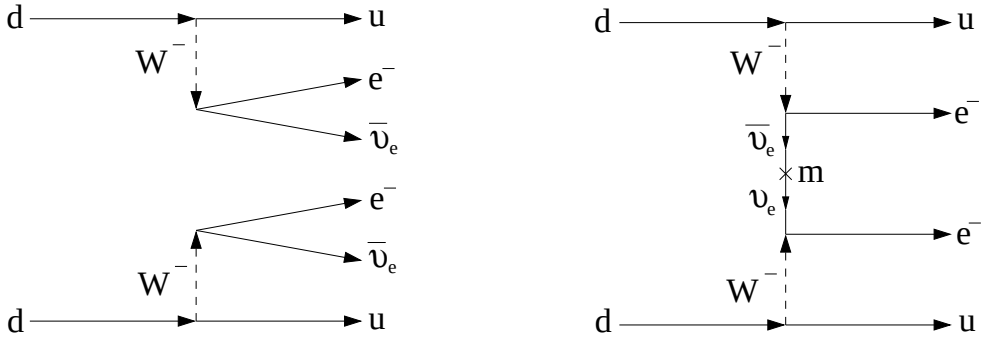

(a) $2\nu\beta\beta$-decay **(b)** $0\nu\beta\beta$-decay

Figure 1.1: Feynman diagrams of the $2\nu\beta\beta$ and the $0\nu\beta\beta$-decay. The $0\nu\beta\beta$-decay is possible under the exchange of a massive Majorana neutrino.

1.1.2 Neutrinoless double beta decay

A fundamental question about the neutrino is still unanswered: is the neutrino a Majorana particle? The Majorana condition requires a particle to be identical under charge conjugation $\nu_i^c = \nu_i$. The helicity of the (left-handed) neutrino ν would be its only distinction from the (right-handed) anti-neutrino $\overline{\nu}$. However, helicity is not a 'good' quantum number for massive particles, since it is only conserved for particles at the speed of light. As it is known from neutrino oscillations that neutrinos have masses, lepton number violating processes would be possible. Since the violation of helicity conservation depends on mass over energy (m/E), such processes would allow to probe the neutrino mass scale. Moreover, the Majorana nature of neutrinos is required by most seesaw models [25], and would provide an explanation for the baryon asymmetry of the universe [26]. It is therfore highly anticipated by several extensions of the standard model.

The only known practical way to probe the Majorana nature of neutrinos experimentally is via the discovery of the neutrinoless double beta ($0\nu\beta\beta$) decay. In some even-even nuclei the single β-decay is energetically forbidden, whereas the simultaneous but independent β-decay of two nucleons is allowed – called the two-neutrino double beta ($2\nu\beta\beta$) decay (figure 1.1a). This second-order process, in which two neutrinos are emitted, has been observed in 10 isotopes (^{48}Ca, ^{76}Ge, ^{82}Se, ^{96}Zr, ^{100}Mo, ^{116}Cd, ^{128}Te, ^{130}Te, ^{150}Nd, ^{238}U). A variation of this decay without the emission of neutrinos is the $0\nu\beta\beta$-decay (figure 1.1b): if neutrinos are Majorana particles, a right-handed neutrino can be emitted in one vertex, and be absorbed at the second vertex as a left-handed neutrino – provided that a 'helicity flip' occurs. The lepton number in this process changes by 2, and thus violates lepton number conservation. The half life is given by

$$\frac{1}{T_{1/2}^{0\nu\beta\beta}} = G_{0\nu}(E,Z)|M_{0\nu}(A,Z)|^2|m_{ee}|^2$$

where $G_{0\nu}(E,Z)$ is the known phase space integral, $M_{0\nu}(A,Z)$ is the nuclear matrix element, and $m_{ee} = \sum_i U_{ei}^2 m_i$ is the effective Majorana neutrino mass [27]. Currently, the available predictions for the nuclear matrix element are very model dependent. Yet, with them, a

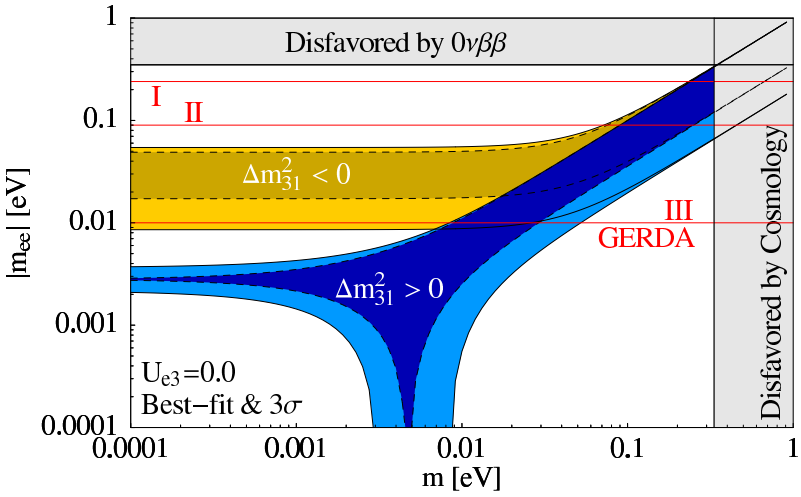

Figure 1.2: Predictions for the effective Majorana mass m_{ee} as a function of the lightest neutrino mass m, for the case of normal (blue) and inverted (yellow) mass hierachy. For $m \gg \Delta m_{13}$ the mass scheme is degenerate. The colored bands are calculated on the basis of the mixing parameters from oscillation experiments. The darker areas exclude the experimental error to emphasize the contribution of the Majorana CP-phases. The red lines indicate the projected sensitivity of the two GERDA phases, and a future 1 ton ^{76}Ge experiment ('GERDA phase III'). By courtesy of Werner Maneschg [28].

measurement of the $0\nu\beta\beta$ half-life would yield the effective Majorana neutrino mass[2], and allow to determine the mass hierachy – see figure 1.2.

Experimentally, several approaches are persued to detect the $0\nu\beta\beta$-decay in various isotopes (^{100}Mo, ^{150}Nd, ^{130}Te, ^{136}Xe). At present, the most stringend limits on the half life come from ^{76}Ge experiments, namely Heidelberg-Moscow (HdM) with $T_{1/2} > 1.9 \cdot 10^{25}$ years [29], and IGEX with $T_{1/2} > 1.6 \cdot 10^{25}$ years [30] (both 90% c.l.). Part of the HdM collaboration published a claim of a 4.2 σ evidence for the detection of the $0\nu\beta\beta$-decay with $T_{1/2} \approx 1.2 \cdot 10^{25}$ years, corresponding to $|m_{ee}| = 0.24 - 0.58$ eV [31]. However, this claim has been disputed [32], and requires independent experimental scrutinization.

1.2 GERDA

The GERmanium Detector Array (GERDA) is an experiment to search for the $0\nu\beta\beta$-decay in ^{76}Ge. It has been proposed in 2004 [33], and celebrated its inauguration with a completed setup in November 2010. Currently, GERDA is in commissioning phase taking first data.

1.2.1 Detection principle

GERDA operates high-purity germanium (HPGe) detectors enriched to 86% in ^{76}Ge, which are submersed naked into liquid argon (LAr). The Ge-crystals are simultaneously used as

[2] strictly speaken, this would only give an upper limit on m_{ee}, since other competing decay channels beyond the standard model can not be excluded.

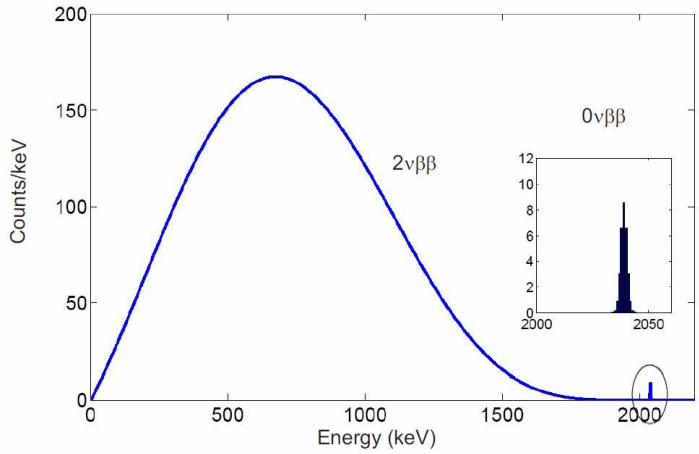

Figure 1.3: Calculated spectrum of the sum of electron energies from the $\beta\beta$-decay of ^{76}Ge. The $2\nu\beta\beta$-spectrum is continuous, since energy escapes with the neutrinos, whereas the $0\nu\beta\beta$-decay creates a small peak at $Q_{\beta\beta} = 2039$ keV. For the calculation, a typical energy resolution of 3 keV FWHM at 2039 keV is assumed; the utilized half lifes are $T_{1/2}^{2\nu\beta\beta} = 1.7{\cdot}10^{21}$ years, and $T_{1/2}^{0\nu\beta\beta} = 1.2{\cdot}10^{25}$ [34].

a source and as a detector for the $0\nu\beta\beta$-decay. As a detector, germanium has an excellent energy resolution, and is a well known routinely used technique. It is one of the purest solid materials available, which allows to reach the ultra-low background level required to detect half lifes of $> 10^{25}$ years. The double beta ($\beta\beta$) decay signal is caused by the full absorption of the two emitted electrons in the detector; a calculation of the expected spectrum is shown in figure 1.3: events in the continuous $2\nu\beta\beta$-spectrum exhibit an energy deficit towards $Q_{\beta\beta}$ = 2039 keV, because the neutrinos escape with a part of the total energy. Since no neutrino can escape from the $0\nu\beta\beta$-decay, the detected electron energy sums up to $Q_{\beta\beta}$, such that a small peak appears at 2039 keV. The count rate of the peak can be translated into the half life $T_{1/2}^{0\nu\beta\beta}$. In order to detect this peak, the region of interest (ROI) must be kept quasi background free, which poses the key challenge to GERDA.

1.2.2 Setup description

GERDA is build-up underground at the Laboratori Nazionale del Gran Sasso (LNGS) [35] in a depth of 1400 m (3800 m water equivalent), to be shielded against background from cosmic radiation – see figure 1.4. At this depth, the muon flux is reduced by $\sim 10^6$. For the sake of a low background, the Ge-detectors are deployed naked into the 65 m^3 of LAr, to minimize the amount of surrounding material. The LAr serves both as a coolant for the Ge-diodes, and as a high purity shield. The detectors are mounted into low mass copper holders, which can be connected to strings and be arranged in an array at the center of the cryostat. A lock system in a clean room on top of the cryostat is used for detector handling, and for deployment of the detector strings. The cryostat is made from low background steel (^{232}Th and ^{238}U at $\sim$1 mBq/kg), is equipped with a high purity copper shield on the inside wall. An outer water tank containing 650 m^3 of purified H_2O completes the shielding. The water is also used as an active veto against residual high-energy muons, by detecting their

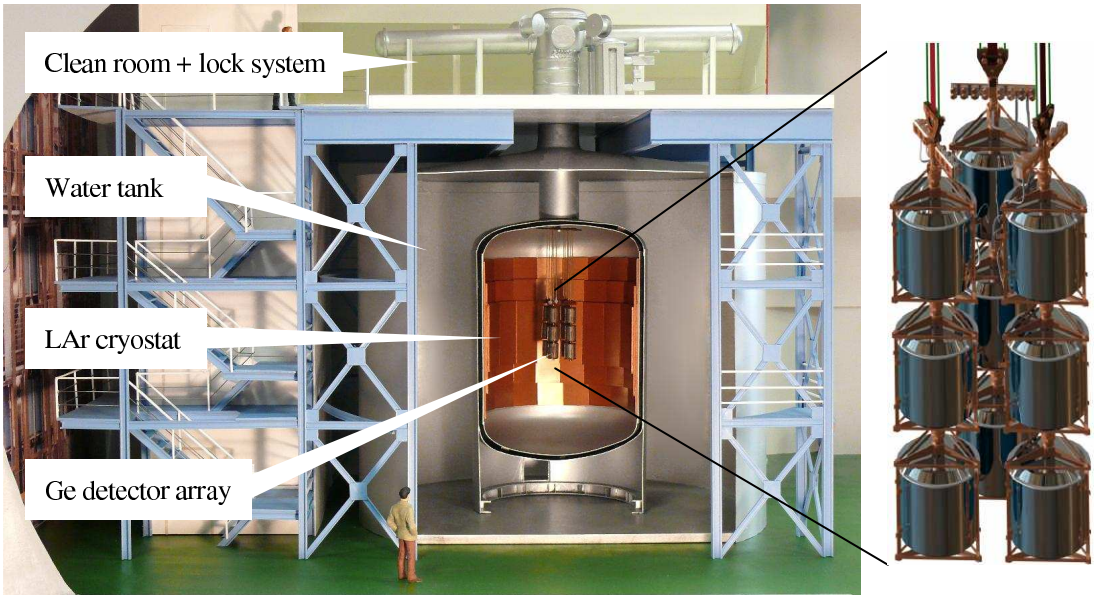

Figure 1.4: Artistic model of the GERDA experiment (not in scale), and the enriched HPGe detector array for GERDA phase I.

Cherenkov light in the tank with photomultiplier tubes.

The dominating background of GERDA is expected from ^{68}Ge and ^{60}Co inside the Ge-diodes. These isotopes are cosmogenically produced in the germanium at the earth's surface, by activation through the hadronic component of cosmic rays. Therefore, an effort is made to minimize the exposure of the detectors above ground during production and processing phases. The next relevant sources of background are impurities in the holder material, front-end electronics, and cables in the vicinity of the detectors. Here, the critical radiation are gamma rays from ^{208}Tl and ^{214}Bi, both of which have energies above $Q_{\beta\beta}$, and are naturally abundant. Further background sources are surface contaminations on the crystals, radon in the LAr, external gamma background, and cosmic muons with delayed muon induced background.

1.2.3 Physics reach

GERDA is planned to operate in two phases. In phase I, the former HdM and IGEX HPGe detectors are employed; these are eight detectors (18 kg) enriched to 86% in ^{76}Ge. Six natural HPGe detectors are reprocessed from Genius-TF (GTF) and can be used for reference measurements and testing. The background index in phase I is aspired to be lower by at least one order of magnitude compared to the predecessor experiments, that is $< 10^{-2}$ cts/(keV·kg·y).[3] Assuming an exposure of 15 kg·y and a resolution of 3.6 keV, one expects 0.5 background events in the ROI. For one background event this translates to an upper limit of $T_{1/2} > 2.2 \cdot 10^{25}$ y (90% c.l.), and a corresponding effective neutrino mass of m_{ee} <0.28 - 0.9 eV (using the nuclear matrix element from [27]). Thereby, GERDA would scrutinize the HdM claim [31] within one year of data taking.

[3] kg refer to the total mass of germanium, y = years.

For phase II, it is planned to add $\sim$ 20 kg of new enriched Ge-detectors, and achieve a total exposure of 100 kg·y within $\approx$3 years of data taking. Different background suppression methods are forseen to be implemented, two of which are topic of this work (pulse shape discrimination and LAr anticoincidence). After all, GERDA phase II strives for a background reduction by another order of magnitude, down to a background index of $< 10^{-3}$ cts/(keV·kg·y). With a large chance of observing zero background events, one would obtain a limit of $T_{1/2} > 2 \cdot 10^{26}$ y, and an effective neutrino mass of m_{ee} <0.09 - 0.29 eV, depending on the nuclear matrix elements used.

Conceivable future prospects are to merge different $0\nu\beta\beta$-collaborations in a common effort to build an ultimate ^{76}Ge-experiment, with one tonne of enriched germanium, to tackle the 10 meV mass range. The expected sensitivities of the experimental phases to m_{ee} are indicated in figure 1.2.

1.3 Introduction to the LArGe project

LArGe is the LAr Germanium test facility of GERDA, which can operate up to 9 Ge-detectors in 1 m^3 of LAr in a low-level environment. In contrast to GERDA, the LAr is equipped with 9 photomultiplier tubes (PMTs), which can detect argon scintillation light.

1.3.1 Liquid argon as anti-coincidence veto

Liquid argon scintillates upon the interaction with ionizing radiation, and produces $\sim$40000 photons per MeV deposited energy at 128 nm wavelength. The idea is to use the argon scintillation light as an anti-coincidence veto for Ge-detectors in GERDA, to suppress background in the ROI of $Q_{\beta\beta}$, and elsewhere. Background events in the ROI typically have excess energy, which they deposit outside the Ge-detector in the surrounding medium, in our case the scintillating LAr. Conversely, $0\nu\beta\beta$-events are confined to the Ge-diode, so that no scintillation light is triggered. An observation of the light is therefore a good indicator for a background event, and can be used to veto the coincident Ge-signal. For that purpose, the LAr must be instrumented to detect the light; in case of LArGe PMTs are used. The light is guided to the PMTs with reflecting foils on the inner cryostat wall, and is shifted in its wavelength to match the sensitive range of the PMTs.

1.3.2 Preceeding work

In the preparatory phase of GERDA, the operation of naked HPGe detectors in LAr was studied with a focus on the LAr properties. One aspect was the investigation of argon scintillation light in anti-coincidence with Ge-detector signals. A feasibility study was conducted with the LArGe-testbench at MPIK, which prepared the ground for the construction of the improved Mini-LArGe setup [36]. Mini-LArGe has an active LAr volume of 13.5 l (19 kg of LAr), it is equipped with a 8" PMT, and can simultaneously operate a bare Ge-detector. For the first time, suppression factors of an argon scintillation veto were systematically measured for different sources, e.g. a factor 3 has been achieved for the suppression of ^{60}Co in the ROI of $Q_{\beta\beta}$, and a factor 17 for ^{232}Th. Yet, the suppression in this setup was limited by the small active volume (radius 10 cm). In addition, however,

scintillation pulse shape analysis was successfully used to efficiently discriminate particles of different ionization density; namely γ's from α's, and γ's from neutrons, which is a powerful tool for background diagnostics. This was possible with the development of a stable wavelength shifter/reflector combination, which made a high photo electron yield of 1.24 pe/keV [37, 38] possible.

1.3.3 Objectives of LArGe

The LArGe setup is build to investigate the achievable background suppression by using a LAr scintillation veto in a low-background setup, for possible applications in GERDA phase II and beyond. It is the first time that naked Ge-detectors are operated in a low-background environment with 1 m^3 (1.4 tons) instrumented LAr. The background suppression can be studied with different sources in different locations, that represent characteristic background sources to GERDA. Also, it shall be demonstrated, that the benefit of LAr-suppression is not outweighted by additional background from the LAr-instrumentation. On the contrary, by using the LAr veto, LArGe aspires to reach a background index of $< 10^{-2}$ cts/(keV·kg·y), the design goal of GERDA phase I. Due to its low-background, LArGe can be used to verify the low background of HPGe detectors prior to their operation in GERDA, and establish detector handling procedures.

Chapter 2

The experimental setup

The constructional design of the LArGe setup is described in the first section of this chapter. The following sections provide insight on design details and testing of the critical components, which predated the assembly, and the front-end electronics & data aquisition (DAQ) system. While LArGe is build-up at LNGS, most of the preceding work, including an integration test, was carried out at MPIK Heidelberg.

2.1 Setup description

2.1.1 Overview

The LNGS [35] underground facility is located along a highway tunnel through the Gran Sasso mountain, Italy, and has a depth of 3800 m water equivalent. LArGe is situated in the GDL (Germanium Detector Lab) in the interferometer tunnel, a GERDA facility close to the GERDA site in Hall A. The GDL barrack is operated as a cleanroom. Its air volume (300 m^3) is exchanged once per hour through HEPA-filters, temperature and humidity are controlled. The LArGe setup itself is placed at the north side of the lab, with cryogenic infrastructure, a slow control, and the data aquisition system adjacent. Storage tanks for liquid nitrogen (LN_2) and liquid argon (LAr) are placed outside of the GDL, and are directly connected with the cryogenic system inside.

Figure 2.1 gives an outline of the LArGe setup. The heart of the experiment is a cylindrical, vacuum-insulated copper cryostat of 90 cm inner diameter and a height of 210 cm. It carries 1000 l (1.4 t) of liquid argon. Nine 8" ETL 9357 photomultiplier tubes are immersed with their photocathode into the LAr from the top. The PMTs are mounted in a support structure made from electrolytic copper and Teflon® (PTFE). The filling level of the LAr is adjusted slightly above the PMTs' equator, leaving the upper part of the cryostat in the gas phase of argon. The inner cryostat walls are lined with VM2000 radiant mirror foil[1]. Mirror foil and PMTs are covered with a 1-4 μm thin layer of wavelengthshifter (WLS). An active cooling system using LN_2 as coolant is employed to reduce the LAr loss due to evaporation to zero.

[1] product of the company 3M

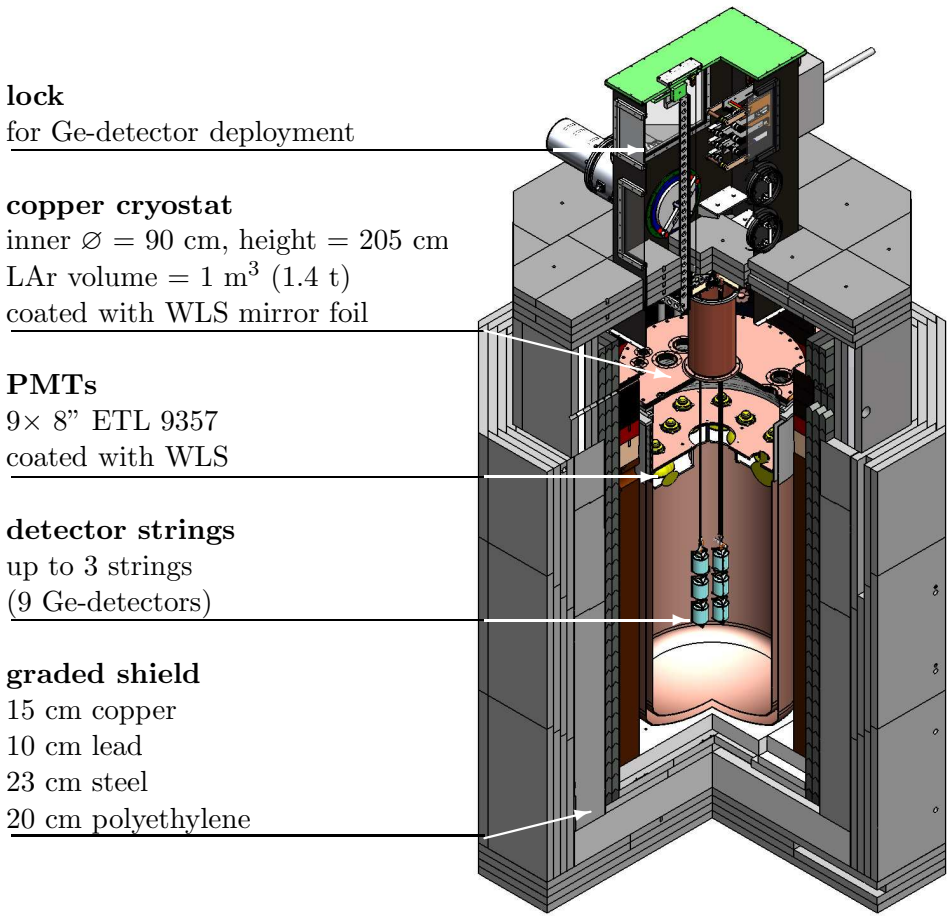

Figure 2.1: Cutaway view of the LArGe setup. The cryogenic infrastructure, a slow control system, and the DAQ are located adjacent to this setup. WLS = wavelength shifter.

The cryostat is surrounded by a graded shield of increased radiopurity to suppress the external background. The outermost layer consists of 20 cm polyethylene, mainly to attenuate neutrons. This is followed by 23 cm of steel, 10 cm of low-activity lead, and 15 cm of electrolytic copper against external gamma background. Finally, the innermost layer are ∼41 cm of LAr, assumed for a centrally positioned Ge-detector of 4 cm radius. Altogether, the goal is to reach a background index of $< 10^{-2}$ cts/(keV·kg·y) with an active LAr veto, which is at the level of GERDA phase I.

A double chamber lock system on top of the shielding serves as an access port for the deployment of Ge-detectors and internal radioactive sources. It can support up to three strings holding three Ge-detectors each. So far, only one detector has been inserted at a time. During detector insertion, the lock is connected to the cryostat via the 'access cylinder' (inner ∅ = 25 cm). The lock and the open volume between cryostat and shield are permanently flushed with gaseous argon (GAr) at slight overpressure. The pressure gradient from the cryostat, via lock and shield, to the outside acts as a safeguard against air-trace contamination of the LAr and avoids background from airborne ^{222}Rn.

Timeline of construction

After the proposal for the LArGe project in 2004 [33], the construction commenced with the modification of the GDL barack in february 2005; these works included an enlargement of the northern part of the barack – the LArGe site, the installation of laboratory infrastructures, and the transformation into a cleanroom. Subsequently, the inner part of the graded shield was installed, using the modified former shield of the LENS solar neutrino experiment [40]. In parallel, the cryostat was fabricated by the company Pützschler & Weiler GmbH in Düren/Germany, the lock and other components were build at the workshops at MPIK. The installation was suspended until completion of the Mini-LArGe studies, and resumed with the design & testing of critical components, which is a major topic of this work:

- 2008-2009: preparatory work. In particular this includes, (a) the selection & testing of PMTs, construction of a support structure and a LED calibration system, (b) coating of the VM2000 mirror foil and PMTs with WLS solution, (c) compilation of the cryogenic system & the slow control, (d) cleaning & shipping of all components to LNGS.
- March 2009: an integration test of the cryostat, the cryogenic system, and the PMT support structure is carried out at MPIK: The cryostat is filled with LAr, the performance of the PMTs inside and the active cooling system are tested.
- September 2009: final assembly of the cryostat with all inner components, the cryogenic system, the slow control, and the DAQ under clean conditions in GDL.
- Commissioning phase, following the assembly: First scintillation light is observed in GAr with a ^{148}Gd alpha-source. After a 1st filling with LAr in November '09, the scintillation light turns out to be strongly quenched due to argon impurities. The cryostat is modified and refilled with LAr in February '10, with the light now remaining stable.
- May 2010: The lock is installed and the copper shield is completed. A 'nacked' BEGe detector is deployed into LArGe. Measurements with different sources determine the suppression efficiency of the LAr-scintillation veto and pulse shape discrimination with BEGe. Also background measurements are performed.
- Since September 2010: The shield is closed further (yet, it is not fully completed), LAr is refilled for higher purity argon, and the Ge-detector is exchanged for the GTF 44 detector of the former GENIUS test facility. Background measurements focus on the ^{42}K abundance in LAr, a critical background to GERDA.

A series of photographs in appendix A illustrates the assembly and commissioning of the LArGe setup at GDL.

2.1.2 Shielding

The design of the LArGe shield is devised to have the gamma background dominated by the radioimpurity of the innermost copper layer (<19μBg/kg ^{228}Th). The radiopurity screening results for different LArGe components are given in table 2.1. The copper itself was

Table 2.1: Gamma-spectroscopy measurements of radioimpurities in LArGe materials. Given is the specific activity in units [mBq/kg]. The origin of the materials is; Copper LENS: NOSV copper from NAA Hamburg. Lead LENS: 'DowRun'-quality from JL Goslar. Steel (shield): carbon steel from Dillinger Hütte GTS. PE (shield): polyethylene from Simona AG. VM2000: radiant mirror foil (with glue) from 3M. Araldit (resin): AW106. Araldit (hardener): HV953V. PMT glass (neck & bulb): ultra-low background glass from ETL (now ET Enterprise Ltd).

material	specific activity				
	^{226}Ra (^{214}Bi,^{214}Pb)	^{228}Ra	^{228}Th (^{212}Pb,^{208}Tl)	^{40}K	others
copper LENS[a,1]	<0.016		<0.019	<0.088	<0.01 ^{60}Co
lead LENS[a,1]	<0.029		<0.022	0.44(14)	0.18(2) ^{60}Co, 0.098(24)^{207}Bi, 27(4)·10^{3} ^{210}Pb
steel (shield)[b,2]	2.04(33)	1.63(41)	5.34(69)	<4.2	<0.3 ^{60}Co
PE (shield)[b,2]	<2.5	11.2(32)	<3.4	10.8(67)	
VM2000[a,2]	<1.6	<2.2	<1.2	140(10)	<0.44 ^{60}Co, <0.45 ^{137}Cs
Araldit (resin)[a,2]	<0.38	<0.30	<0.19	1.3(7)	<0.052 ^{137}Cs
Araldit (hardener)[a,2]	0.3(1)	0.3(2)	0.4(1)	4(1)	<0.051 ^{137}Cs, 17(8) ^{234}Th, 1.0(5) ^{235}U
PMT glass (neck)[b,2]	2040(210)	1620(420)	290(70)	2470(590)	<370 ^{137}Cs
PMT glass (bulb)[b,2]	2010(190)	2010(480)	210(60)	1750(430)	<370 ^{137}Cs

[a] measured with the GEMPI spectrometer at LNGS. [42]

[b] measured in the Low-Level Lab at MPIK Heidelberg. [43]

[1] upper limits given for k=2, 97.7% confidence level

[2] upper limits given for k=1.645, 95% confidence level

produced in close coordination with the manufacturer, which allowed to keep the exposure time for cosmic activation low (<10μBg/kg ^{60}Co). The relatively high content of ^{228}Th in the carbon steel (∼5.3 mBq/kg) of the former LENS shield, led to an additional layer of low-activity lead (<22μBg/kg ^{228}Th) between copper and steel. Together, all three layers attenuate an external gamma from the 2615 keV line of ^{208}Tl to 5·10^{-8} of the initial flux. At the inside of the cryostat, the PMT glass and the VM2000 mirror foil yield the highest radioimpurities. For the mirror foil, the low area density of 86 g/m^2 leads to a surface activity <0.1 mBq/m^2 ^{228}Th, below that of the copper (<5.4 mBq/m^2). For the PMTs, in contrast, a low mass of 700 g each and a minimum distance of 100 cm to the Ge-detectors reduce their effective surface activity to merely ∼18 mBq/m^2 ^{228}Th. The background index from ^{208}Tl at $Q_{\beta\beta}$ (2039 keV) is calculated to be 0.04 cts/(keV·kg·y). Together with an active LAr shield, Monte Carlo simulations predict that a total background index of $< 1 \cdot 10^{-3}$cts/(keV·kg·y) is possible [41].

The installation of the shield, as it is shown in figure 2.1, is not finalized at present. The steel layer is completed to 2/3 of its planned height, the lead shield to about half. The

Figure 2.2: The LArGe passive shield during construction. All four layers depicted in figure 2.3 are visible.

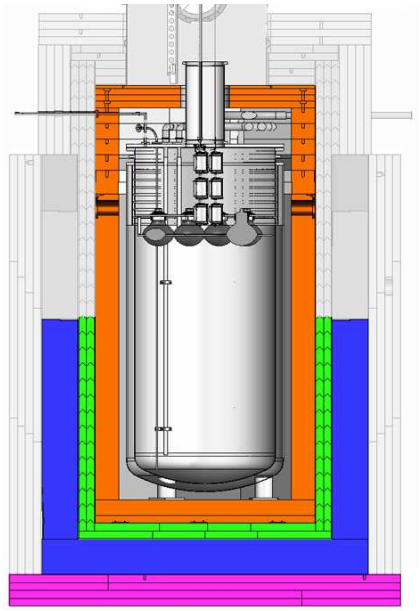

Figure 2.3: A schematic view of the passive shield with closed copper layer, as it is used for the suppression efficiency measurements: Polyethylene (magenta), steel (blue), lead (green), and copper (orange).

polyethylene shield is installed only at the bottom. The copper shield remained opened at the top during commissioning phase, and was fully closed with installation of the lock. Figure 2.2 shows a photograph of the shielding layers during the assembly of the inner part in 2005. The status of the closed shield available for the measurements of the suppression efficiencies is illustrated in figure 2.3.

On the side of the shielding, tubes from the cryogenic infrastructure, cables from sensors, PMTs, and optical fibres exit the shielding through flanges. All flanges are sealed with low emanation rubber O-rings, and gas tight cable feedthroughs are used. The cryogenic tubes and the gaps of the copper bricks are sealed with acid-free silicone. Flanges in the side of the Cu-shield give access to place external radioactive sources between shield and cryostat.

2.1.3 Cryostat

The main body of the double-wall LArGe cryostat is made from electrolytic copper; top collar and a bellow are made from stainless steel. The PMT support structure rests on a rim at this copper-steel transition. The LAr filling level is adjusted 1-7 cm below the rim. The cryostat is closed by a lid, a 38 mm thick flange from electrolytic copper (called 'top flange'), which itself is equipped with various smaller flanges for cable feedthroughs and tubes from the cryogenic system; dimensions and labeling of the parts are shown in figure 2.4.

Heat loss is primarily prevented by the insulation vacuum of 10^{-5} to 10^{-6} mbar, the pressure

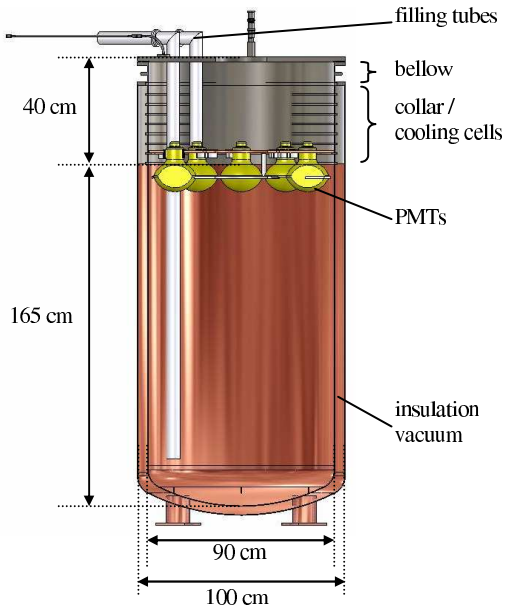

Figure 2.4: Illustration of the cryostat with dimensions and labels of the main components. The PMTs on their support structure rest on a metal rim at the copper-steel transition.

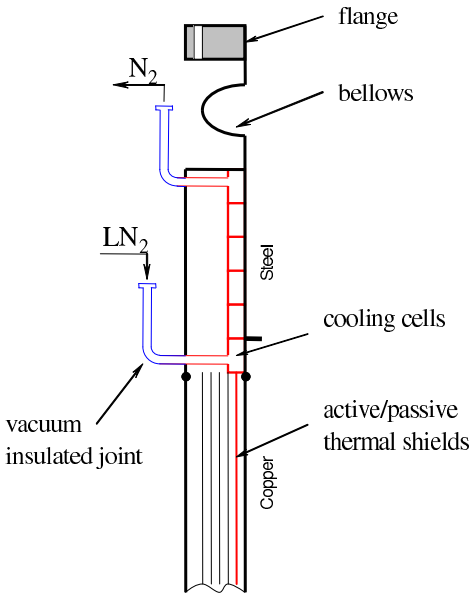

Figure 2.5: Schematic cross section of the upper cryostat wall with the integrated active cooling system and IR shields.

of which is supervised by the slow control; the vacuum can be pumped from the outside at any time. For insulation of the lid, multiple thin layers of copper, Teflon®, and Teflon-mesh are mounted on the inside. A strong temperature gradient builds up from the copper at LAr temperature, to the lid, which itself stays above the freezing point. In order to minimize the thermal conductivity of the intermediate part, the collar is made from stainless steel – rather than copper, and the bellow was inserted. The insulation vacuum of the copper body is equipped with several thin copper sheets, which act as infrared (IR) shields – see figure 2.5. An active cooling system cools the innermost IR shield to LAr temperature, and carries heat away from the steel collar: LN_2 enters cooling cells at the copper-steel transition, were the IR shield is fixed. The LN_2 runs up the cells in a spiral on the inner wall inside the collar, evaporates by picking up heat, and exits as a gas below the bellow. The nitrogen flow is controlled by the slow control; the operation is described below in section 2.3.1. It turned out, that during normal operation a LN_2 flow of 2.5 kg/h is sufficient to compensate the total heat load of $\lesssim$90 W on the cryostat, and reduce the LAr loss to zero. Design calculations of the heat load are summarized in table 2.2. Moreover, the heat load was measured at MPIK by the evaporation rate R of LN_2, by which the cryostat was filled for that test: For the unmodified cryostat and a 15 cm foamed-polystyrene lid (instead of the top flange) the total heat load is 149 W (R=2.7 kg/h). With an improved lid and additional 5 cm of polystyrene cleading around the cryostat's body, the heat load was reduced to 77 W (R=1.4 kg/h), well below the design value of 90 W. Thereby, the foamed-polystyrene cleading was kept in the final configuration, whereas the lid is replaced by the top flange.

Due to the complexity of the cryostat, with its large number of flanges, feed-throughs, and couplings – which are not always metal-sealed, it is not perfectly tight. Therefore, in order

Table 2.2: Heat load on the cryostat from different contributions. Calculation by VeriCold Technologies GmbH.

contribution	P [W]
collar (conduction)	56
active IR shield	20
copper lid	10
collar (radiation)	∼0

to prevent air from entering the cryostat, it must be operated at slight overpressure. The normal pressure in the lab is ∼900 mbar; the standard working pressure in the cryostat is 930-970 mbar. By hindsight, a mechanical support of the bellow was added that permits to evacuate the cryostat, and allows a maximum overpressure of +300 mbar. This became important to enable pumping-pressure-cycles, in order to remove traces of humidity from the cryostat prior to filling. For safety, a rupture disc and an overpressure release valve are installed. The pressure is supervised by the slow control. As another measure against LAr contamination, as stated earlier, the shielding around the cryostat is permanently flushed with GAr to avoid diffusion of air constituents, such as Rn, O_2, or N_2, through the seals.

2.1.4 Photomultiplier support structure

The main purpose of the PMT support structure is to fix the phototubes safely in vertical position, with the photocathode pointing downwards into LAr, and without threatening to break the glass body. The different thermal expansion coefficients of the holder plate (copper) and the PMT glass require a flexible suspension system, which compensates the differential thermal shrinking of the two materials from room temperature to LAr at -186 °C. The design was tested in LN_2 (-196 °C) with a mockup for one PMT, shown in figure 2.6: At room temperature, the PMT rests on three thin Teflon® brackets, which shadow the photocathode as little as possible. Immersed in liquid gas, the phototube becomes buoyant, and is hold in place from the top by a ductile Teflon collar. The collar is fixed to the copper plate by a three-point bayonet coupling, towards which the contact surfaces with the glass are rotated by 60°. The length and inner diameter of the Teflon collar is tailored for each PMT individually, so that it is hold firm vertically at liquid gas temperature – when the collar shrinks, and being loose at room temperature.

The final LArGe PMT support structure holds nine PMTs using this system; pictures can be found in the photo series in appendix A. The main plate of 89 cm diameter is made from Lens copper. A central hole of 25 cm diameter permits the insertion of Ge-detector strings. Two LAr filling tubes pass through cut-outs on the side. Teflon plates are mounted 8 cm below the copper plate at the height of the PMT equator, to fill in the gaps between the phototubes: The plates have a high (diffuse) reflectivity, and prevent the loss of scintillation light. The light sensitive photocathodes cover 44% of the horizontal surface. The LAr filling level is adjusted between the Teflon and copper plate, being monitored by seven PT1000 temperature sensors between the plates in 1 cm spacing, and four sensors below. One temperature sensor measures the temperature of the cryostat wall above the LAr level. At

Figure 2.6: Left: PMT support mockup. The range of the LAr filling level between copper plate and PMT equator is indicated. **Center top:** ductile Teflon® collar. **Center bottom:** Teflon bracket. **Right:** mockup submersed in LN_2.

the inside of the central hole, three LED light diffusors are mounted for PMT calibration. The top side of the copper plate is equipped with various Teflon clamps, to fix and guide PMT cables and optical fibres from the diffusors towards their designated flanges in the big top flange of the cryostat.

2.1.5 Lock system & detector deployment

The lock on top of the LArGe setup serves for the deployment of Ge-detector strings and internal wire sources into the cryostat. The main body is a stainless steel glove box with acrylic windows – details of the lock are depicted in figure 2.7. Two secondary air-locks are attached at the side: an 'intermediate lock' (b) and a portable 'transportation lock' (c). All three lock volumes can be flushed with external GAr independently. During normal operation, the main lock is constantly flushed with an argon flow from the shield volume, which in turn is supplied by the evaporation from an external LAr dewar; the hatch towards the intermediate lock is closed.

The Ge-detectors are mounted to a low-mass holder in a separate cleanbench in gaseous nitrogen (GN_2) atmosphere, and loaded to the transportation lock. The lock is pressurized with GN_2, and then transfered and mounted to the intermediate lock, in which the detector is put on a sliding table. When the hatch to the main lock is opened, the table with the detector can be moved in. Throughout the procedure, all locks are kept under GN_2 or GAr atmosphere to prevent the Ge-detector from being exposed to air.

Before the table with the Ge-detector is moved into the main lock, the cryostat is opened. It is critical to keep constant overpressure in the cryostat and the main lock, to avoid air-trace contamination of the LAr. For this purpose, the active cooling system is temporarily interrupted and additional GAr is pushed into the cryostat. The cryostat is accessibly

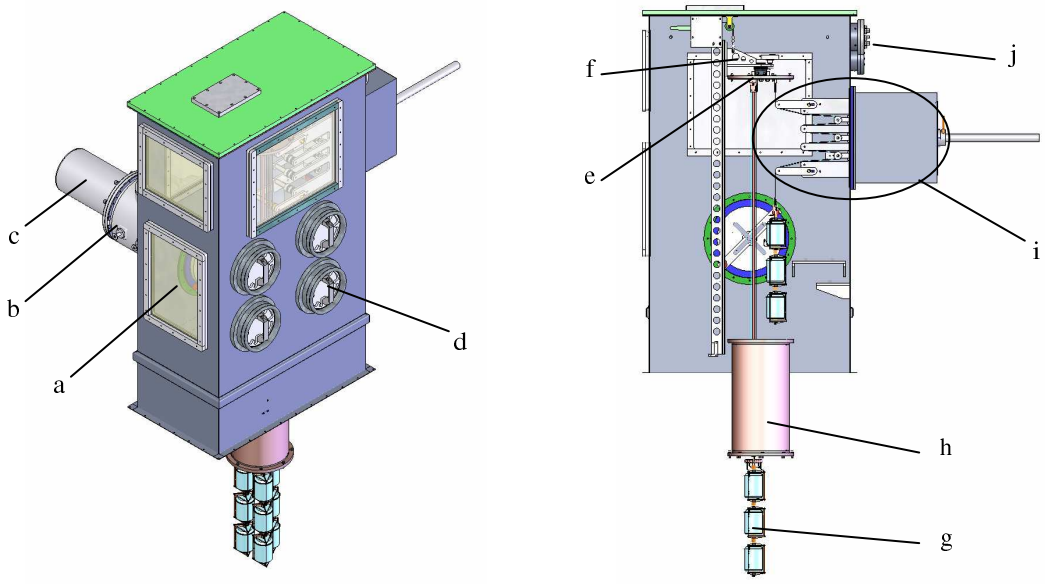

Figure 2.7: Illustration of the main lock and its components: **(a)** stainless steel casing with PE windows, **(b)** intermediate air lock, **(c)** transportation lock, **(d)** butyl gloves, **(e)** copper flange of access cylinder, **(f)** vertically movable aluminum slide, **(g)** detector string, **(h)** access cylinder on cryostat, **(i)** multi-arm lowering mechanics with step motor, **(j)** flanges with gastight HV feedthroughs.

through the 'access cylinder' made from copper and stainless steel (h), the flange of which (e) is now lifted vertically by a movable aluminum slide (f). Now, the table is moved in and the detector is mounted below the flange with a long stainless steel strip. Later, the detector will hang on this strip, whose length determines the detector's vertical position in the cryostat. The steel strip is engaged in a mechanical device (i), which is driven by a step motor, and can automatically lower the detector string into the LAr at a speed of a few cm/min. Such a low speed reduces thermal stress and oscillations of the string.

The copper flange has three smaller flanges (one for each potential detector string), through which the signal- and high-voltage cables are fed through: The cables are glued into a 1/4" Swagelok®, which is connected to copper tubes in the small flanges; the purpose is to reduce the number of feedthroughs to avoid signal reflections and spark discharges in the argon gas. Eventually the cables are connected via gastight HV feedthroughs (j) in the main lock with the DAQ system outside. Once a detector string is fully mounted, the steel strip is led down by the lowering mechanics, and the copper flange is lowered to close the cryostat. After the active cooling is switched on and stable thermal conditions are established, the HV power-supply of the PMTs and Ge-diodes may be ramped-up and resume operation.

For the removal of the detectors the procedure is followed in reverse order, with one additional step: Directly after dismounting, the cold crystals are submerged in a warm methanol bath to warm up. When they finally reach the cleanbench, the diodes are stored under vacuum (10^{-5} mbar) in designated containers. These measures are adopted from the Ge-detector manufacturer Canberra, Olen, in Belgium.

Wire source mounting

Internal wire sources can be inserted directly adjacent to the Ge-diodes in the argon. A special 'source flange' occupies one of the three small flanges on the cylinder flange: The wire, with the encapsulated source at the end, is inserted through a metal tube on the flange, and fixed to it at the proper length. A 50 cm long black shrink-hose over the metal tube and the outer end of the wire prevents light- and gas penetration into the cryostat. Below the flange, the source hangs down to the side of the crystal, approximately 7 cm from the string axis. To keep the wire straight, it is charged with a 5 g copper weight 5 cm above the source. When the source is removed, the metal tube can be closed with a ball valve.

2.2 Wavelength shifter application

As pointed out earlier, the purpose of the VM2000 radiant mirror-foil is to guide argon scintillation light towards the PMTs, as well as to shift their wavelength from 128 nm into the ultraviolet, towards the sensitive range of the PMTs around 370 nm. The mirror foil itself has fluorescent properties, which we nevertheless strive to improve in order to increase the photo-electron yield by coating the foil with a wavelength-shifting (WLS) fluorescent dye. Also, the glass window of the PMTs' photocathodes are coated with the same fluorescent dye. The composition and application method of the WLS solution has been established in an extensive test series within the Mini-LArGe work, presented in the PhD thesis of Peter Peiffer [36]. The aspired coating thickness for mirror foil and PMTs is 1-4 μm, which is a compromise between the absorptivity of scintillation light – seeking a thick layer, and the mechanical stability at LAr temperature – favoring a thin layer. Too thick layers result in cracks and/or micro-crystals on the coating, which impede the light collection, and small detached particles cause a threat to the surface of the naked Ge-detectors. Therefore, our priority for coating is the mechanical stability, rather than an optimized photo-electron yield.

2.2.1 WLS solution

The concept of the WLS is to use a fluorescent dye embedded into a polymer matrix. The optimized composition is polystyrene (PST) as a polymere, with a concentration of 10% by weight tetraphenyl-butadiene (TPB) as a dye. Both substances are dissolved in toluene. When applied and the toluene evaporates, the polymerisation creates a strong bond to the mirror foil or the photocathodes' surface. The bond is enhanced for the mirror foil, since its material, PEN, is also weakly soluble in toluene.

The wavelength shifting process is as follows: scintillation light is absorbed by the PST, which has an absorption maximum of 260 nm. The energy is then transferred non-radiatively to the TPB, which in succession emits light with an emission maximum of 450 nm. The PST is transparent to the fluorescent light, and the emission wavelength spectrum overlaps largely with the PMTs spectral sensitivity curve.

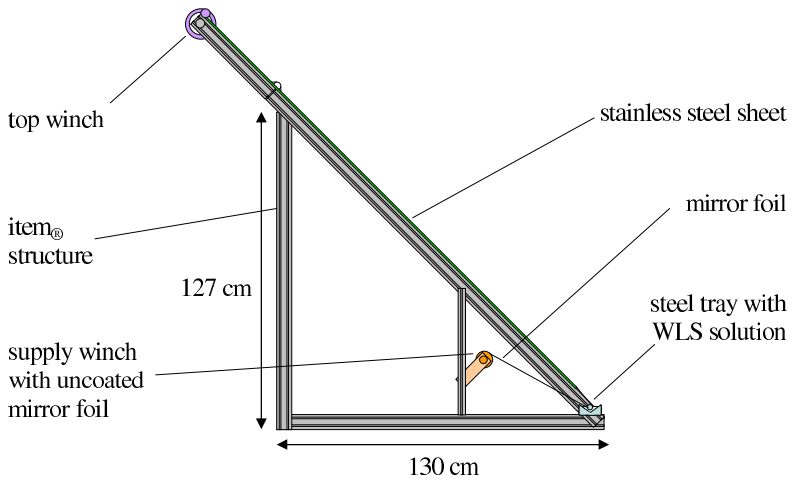

Figure 2.8: Side view on the second generation mirror-foil coating-machine. The total width of the machine is 152 cm, the parts guiding the mirror-foil are ≥128 cm. The total useable length of coated foil is 170 cm per run, and 30-40 cm waste. The coating procedure is explained in the text.

2.2.2 Mirror foil coating

The VM2000 mirror foil as a roll is delivered only with a one-sided self-adhesive surface; the glue has to be removed with acetone before coating. Mini-LArGe experience suggests that the best way for coating the VM2000 mirror foil is to pull the foil through a tray of WLS solution in a homogeneous speed of approximately 10 cm/s, and in an angle of 45°. For LArGe, however, the coating must work on a larger scale; preferentially for pieces of 123 cm width – the width of the foil, and a length of ≥150 cm – the height of the cryostat's inner wall. A total surface of 7 m^2 has to be lined with foil. For this purpose, a coating machine was constructed, and a first batch of mirror foil was coated in a clean room at LNGS in March 2008 – see photograph A.5 in appendix A. The mirror foil is unwind from a supply winch, is pulled under tension through a stainless steel tray with WLS, and hung-up for drying at 45°. Unfortunately, the coated mirror foil sheets exhibited drip marks and other surface imperfections, which may crack in LAr. The machine was therefore reconstructed with two main improvements: 1) a 130×170 cm^2 stainless steel sheet with 45° inclination was installed to support the foil against sagging while it is drying. 2) a second winch is installed at the top to pull the foil out of the tray across the steel sheet, and thus enable a better control over the pulling speed. The winch is also necessary to overcome the strong adhesion force between foil and steel sheet. A drawing of this coating machine is shown in figure 2.8. The second coating run was done in a cleanroom at MPIK in August 2008. The uniformity of the coating towards the first attempt has visibly improved, and the number of drip marks were strongly reduced.

The spectral quality of the coated foil is assessed with a UV fluorescence spectrometer. For two samples of each sheet emission spectra were taken, and compared to the uncoated VM2000 foil: the samples are illuminated with an exitation wavelength of 260 nm, and the fluorescence light is measured by the spectrometer. The direct excitation with 128 nm, the wavelength of LAr scintillation, was not possible, since no light source in this extreme UV region was available. Instead, we chose an excitation of 260 nm, the absorption maximum

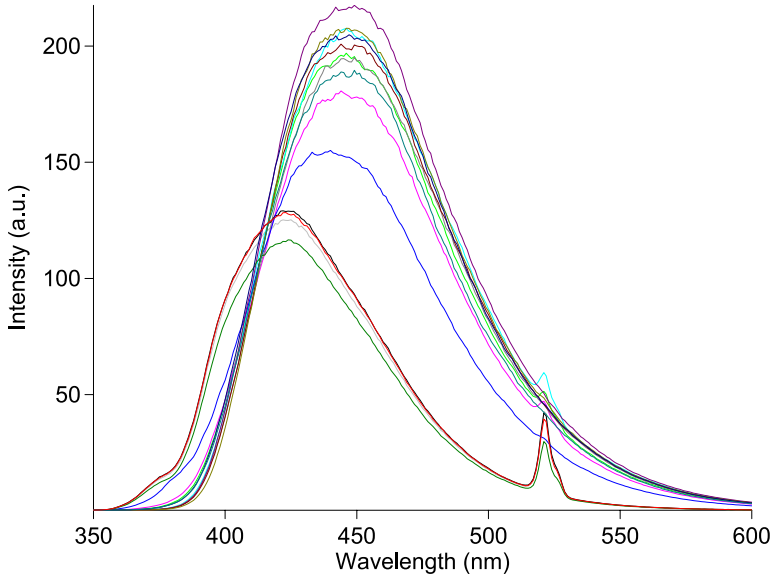

Figure 2.9: Fluorescence emission spectra of the VM2000 mirror-foil. The four lowest curves are reference spectra of uncoated foil. All other curves are taken from samples of the foil coated with WLS-solution. The excitation wavelength is 260 nm. The small peak at 520 nm is due to scattered light from the excitation beam. Since a diffraction grating is used as an analysator, this second order peak at the double wavelength is also registered.

of PST. Also, this is the reference wavelength for the coating optimization done for Mini-LArGe. The emission spectra of our samples are shown in figure 2.9: The four curves with the lowest intensity are the uncoated VM2000 reference samples. The coated samples reach a peak intensity about 1.6 times higher than the reference samples. This ratio is worse than the best sample from the Mini-LArGe investigations, for which a factor 2.1 was achieved. But given our conservative commitment to mechanical stability on the cost of spectral quality, the result is acceptable. All coated samples passed strong mechanical stress-tests in LN_2 successfully.

2.2.3 Mirror foil installation

Prior to the installation of the mirror foil, the inner copper wall of the cryostat was cleaned in several steps: First, the surface was grinded to remove coarse surface contaminations and an oxide layer. Then it was cleaned and degreased using isopropanol and a detergent, to prepare it for surface etching: the etching was done with a sprayball inside the closed cryostat, and an acid-proof PTFE pump, which circulates the acids from the cryostat's bottom through the sprayball. The etching is done in three steps: 1) a few μm surface is removed using a solution of 1% H_2SO_4 (sulfuric acid) and 3% H_2O_2 (hydrogen peroxide) in deionized water. 2) 1% $C_6H_8O_7$ (citric acid) solution passivates the surface against oxidation. 3) the cryostat is rinsed with deionized water. The procedure is well established in the construction of low-level devices. The work was carried out at MPIK in June/July 2009. Finally, after the transportation of the cryostat to LNGS, and directly before the installation of the foil, the surface was wiped with acetone.

The mirror foil is glued into the cryostat using two component epoxy-resin. A thin resin-layer of $\sim$3 mg/cm^2 is applied, corresponding to a total amount of 209 g – the specific activiy of which is given in table 2.1 in section 2.1.2. Special care was taken to avoid air entrapment, since the air volume may expand when the cryostat is evacuated and tear down the foil. Also, the trapped air may contaminate the LAr. Again, the cleaning and installation process is documented on photographs in appendix A.

2.2.4 PMT coating

According to Mini-LArGe experience, the best way to coat the spherical photocathodes is by painting. In order to determine the best coating procedure for a homogeneous thickness between 1-4 μm, we carried out a test series on glass samples, varying the TPB/PST concentration in toluene – thus varying the viscosity of the solution, and the number of painted layers. We obtained the best result with 11 g/l TPB+PST in toluene in four layers. From the amount of applied solution we calculate a coating thickness of 1.8 μm. The glass samples underwent rough mechanical strain in LN_2, to proof their stability.

Subsequently, we coated the former Mini-LArGe PMT and tested it in the Mini-LArGe setup for three months of operation. During this period, several MCA spectra with an internal 9 kBq Th^{228} source were taken to measure the photo-electron yield. The setup was refilled with LAr every two or three days. Since the measurements are carried out equivalently to what is described in Peter Peiffers PhD thesis, please refer to his work for details [36]. The achieved photo-electron yield with the tested PMT remained stable at 1850 pe/MeV throughout the testing period. This is a factor 1.5 higher, compared to 1240 pe/MeV of the preceding Mini-LArGe investigations. Although the photo-electron yield is affected by other parameters, that might have changed between these measurements – e.g. the LAr quality, the comparison shows that the coating quality does not impose a crucial limitation on the electron yield, nor does it degradate over time.

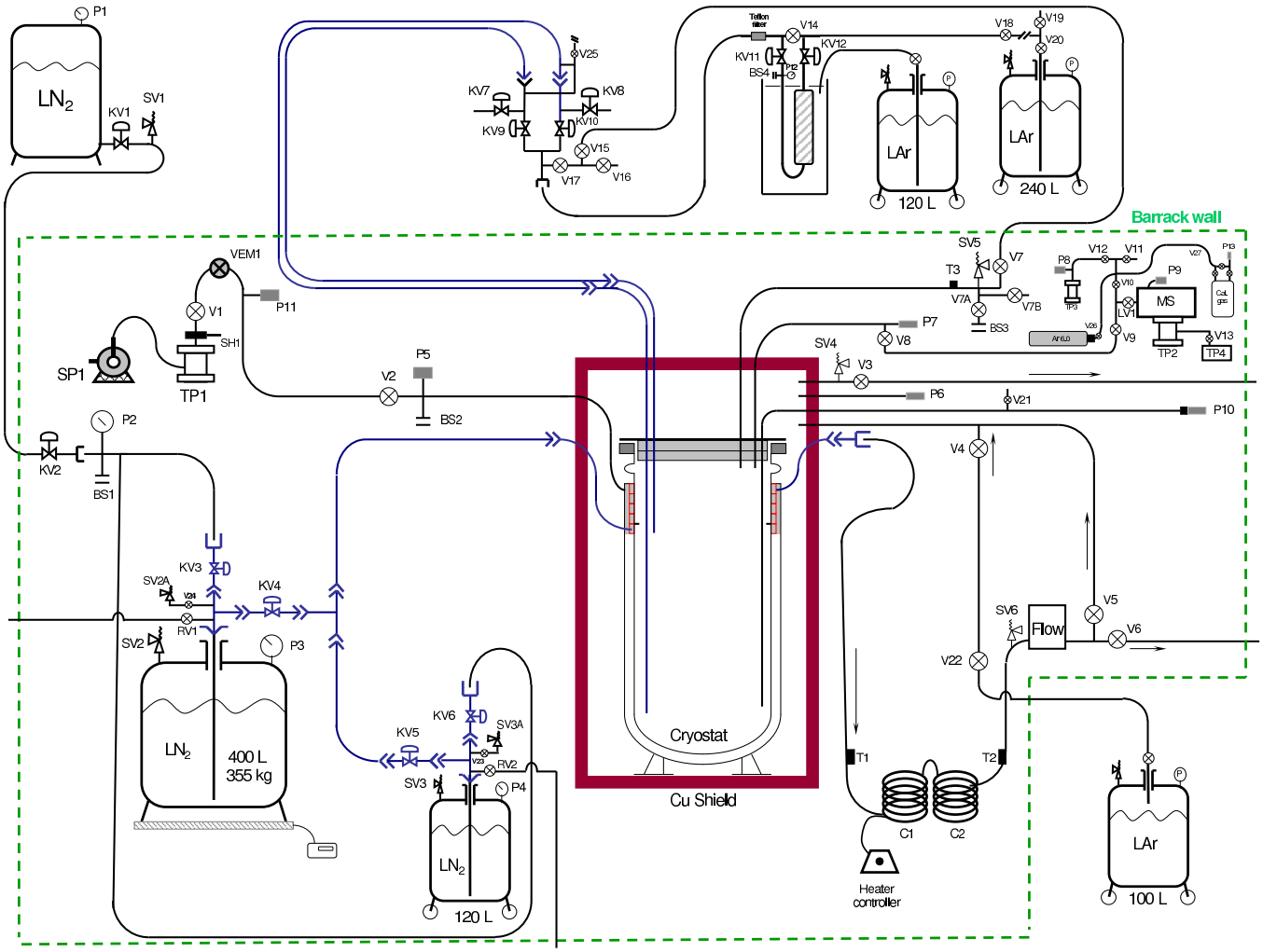

Figure 2.10: Piping and instrumentation diagram (PID) of the cryogenic infrastructure; by courtesy of Grzegorz Zuzel. The basic operations are explained in the text. A legend of the symbols and labels is given on the opposite page.

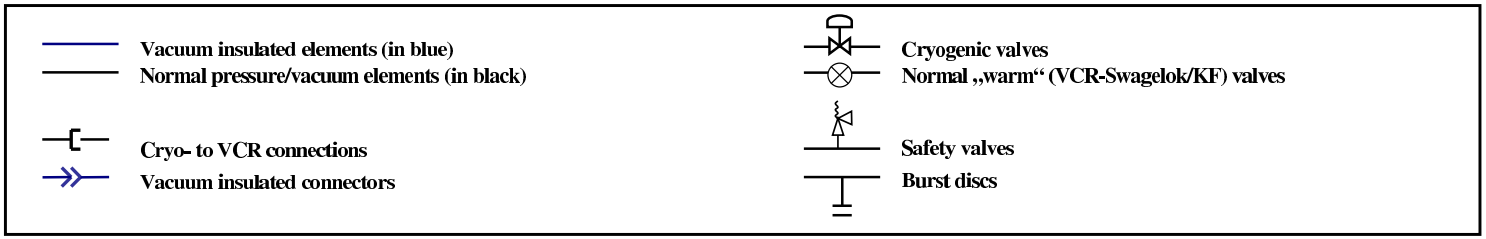

SV1 – safety valve on the nitrogen supply line, outside the barrack, 5 bar
SV2 – safety valve on the 400-L LN_2 dewar, sets the pressure for the active cooling system (1 barg)
SV3 – safety valve on the 120-L LN_2 dewar, sets the pressure for the active cooling system (1 barg)
SV2A – safety valve on the 400-L LN_2 dewar, sets the pressure for the active cooling system (0.5 barg)
SV3A – safety valve on the 120-L LN_2 dewar, sets the pressure for the active cooling system (0.5 barg)
SV4 – safety valve for the shield, 1000 mbar abs
SV5 – safety valve for the cryostat, 1000 mbar abs
SV6 – safety valve for the active cooling system, 1.3 barg
BS1 – Burst disc, LN_2 filling line, 16 barg
BS2 – Burst disc, Cryostat insulation vacuum, 900 mbar abs
BS3 – Burst disc, Cryostat, 1100 mbar abs
BS4 – Burst disc, Rn trap, 10 barg
RV1 – Gas relive valve from the 400 L dewar
RV2 – Gas relive valve from the 120 L dewar

P1 – Pressure gauge on the LN2 storage tank (analog)
P2 – Pressure gauge, LN2 filling line (analog)
P3 – Pressure gauge, 400-L LN2 dewar (analog)
P4 – Pressure gauge, 120-L LN2 dewar (analog)
P5 – Pressure gauge, Cryostat insulation vacuum (Pfeiffer, digital)
P6 – Pressure gauge, shield (Leybold, digital)
P7 – Pressure gauge, cryostat (Pfeiffer, digital
P8 – Pressure gauge of the pump for SPV of the MS
P9 – Pressure in the MS
P10 – Pressure gauge of the source tube
P11 – Pressure gauge, Cryostat insulation vacuum (Leybold, digital)
P12 – Pressure gauge of the Rn trap
P13 – Pressure gauge of the bottle containing calibration gas mixture

T1 – Temperature sensor, cold nitrogen gas (cooling system)
T2 – Temperature sensor, warm nitrogen gas (heating control)
T3 – Temperature sensor, Cryostat vent

SP1 – Scroll pump
TP1 – Turbo pump, insulation vacuum
TP2 – Turbo pump of the Mass Spectrometer
TP3 – Turbo pump of the Sample Prep. Volume of the MS
TP4 – Orange combo pump used as a pre-vacuum for TP2

C1 – Nitrogen warming-up coil, heated with a heating tape
C2 – Backup N_2 warming-up coil, room temperature

Flow – Nitrogen flow controller, active cooling control

KV1 – Cryo-valve at the LN_2 storage tank outside the barrack
KV2 – Cryo-valve on the LN_2 supply line, located inside the barrack just at the wall
KV3 – Cryo-valve, filling line of the 400-L dewar
KV4 – Vacuum insulated cryo-valve, LN_2 supply of the active cooling
KV5 – Cryo-valve, filling line of the 120-L dewar
KV6 – Vacuum insulated cryo-valve, LN2 supply of the active cooling
KV7 – Vent valve of the LAr filling line (top)
KV8 – Vent valve of the LAr filling line (bottom)
KV9 – Vacuum insulated cryo-valve, LAr filling line (top)
KV10 – Vacuum insulated cryo-valve, LAr filling line (bottom)
KV11, KV12 – Cryo-valves of the LAr purification column

VEM1 – electromagnetic safety valve
LV1 – leak control valve (gas inlet for the MS)
SH1 – Shutter valve of the turbo pump

V1 – LArGe insulation pumping line, valve on the turbo pump
V2 – LArGe insulation pumping line, valve on the top (silver with CF-40 flanges)
V3 – Vent valve for the shield, used to regulate the overpressure there
V4 – Ar gas inlet valve for the shield
V5 – N_2 inlet gas valve, regulates the flow of nitrogen into the shield volume
V6 – Vent valve for the nitrogen produced by the active cooling system
V7 – Ar gas inlet valve for the cryostat (connected with the valve panel)
V7A – Valve of the cryostat burst disc
V7B – Argon gas release valve
V8 – Top valve of Ar gas supply to the MS
V9 – Bottom valve of Ar gas supply to the MS
V10 – Valve closing the SPV of the MS
V11 – Valve separating the SPV from the bubbler
V12 – Valve separating the SPV from the turbo pump TP3
V13 – Valve separating TP2 from the TP4 (orange pump)
V14 – By-pass valve of the big Rn trap
V15, V16, V17 – Flushing valves at the valve panel
V18, V19, V20 – Flushing valves at the filling LAr dewar
V21 – T-piece valve of the source tube (flushing of the source tube)
V22 – GAr flushing tube
V23 – Valve to the 0.5 barg safety valve, small LN_2 dewar
V24 – Valve to the 0.5 barg safety valve, big LN_2 dewar
V25 – Valve of the vacuum insulation of the filling lines/adapters
V26 – Valve to the Ar 6.0 bottle (on the pressure reducer)
V27 – Valve to the bottle with the calibration mixture

Figure 2.11: Legend of the symbols and labels used in the PID in figure 2.10; by courtesy of Grzegorz Zuzel.

2.3 Cryogenic infrastructure & operations

The cryogenic system can be divided into several independent subsystems: The active-cooling system, the pumps for the insulation vacuum, and the GAr-flushing system for the shielding serve the preservation of LAr in the cryostat. For filling and flushing a separate branch of infrastructure is used, mainly placed outside the GDL barrack. And finally there is safety and surveillance gadgetry, such as pressure gauges, overpressure valves, burst discs, temperature sensors, and a mass spectrometer for online monitoring of the argon's gas phase. All relevant cryogenic parameters are compiled in a slow control system, to which there is external access via ethernet connection. The piping and instrumentation diagram (PID) of the infrastructure branches is shown in figure 2.10. References to components are given in brackets in the following text, a legend of whose is found in figure 2.11. The cryogenic infrastructure was designed and assembled predominantly by Grzegorz Zuzel, the slow control was implemented by Herbert Strecker. Since the cryogenic operations are particularly important for the commissioning phase, in which the issue of LAr purity arises (chapter 3), its basic operations are briefly outlined here. Details are covered in the 'LArGe safety and operational manual' [44].

2.3.1 Active cooling system

The working principle and implementation of the active cooling in the cryostat has already been described in section 2.1.3: LN_2 is pressed through a cooling spiral in the cryostat's steel collar, and carries away heat by evaporation. On average the LN_2 consumption is 2.5 kg/h, respectively ∼420 kg/week. The LN_2 is supplied by a 400 l dewar, which operates at 0.5 mbar overpressure (P3) to push the LN_2 into the cooling spiral. After the LN_2 is evaporated, the cold nitrogen gas is heated up in warm-up coils (C1 & C2), and the gas flow is measured and regulated by a nitrogen flow controller (Flow). The nitrogen flow determines the cooling power of the active cooling system, and is controlled via the slow control.

The pressure in the cryostat (P7) is regulated by the cooling power: in normal operation, the working pressure is kept stable around 950 mbar, typically in the range 930-970 mbar. When the pressure is dropping, the cooling power is reduced and LAr evaporates, counteracting the pressure drop; when the pressure is increasing, the cooling power is increased and argon from the gas-phase liquifies, thus decreasing the pressure. By this method, the pressure has been controlled reliably during months of operation. As long as the system remains closed, no LAr is lost.

Since the temperature of LN_2 (-195.8 °C) is below the freezing point of LAr (-189.3 °C), it is possible to form argon ice with too much cooling power. For instance, this may happen when the insulation vacuum of the cryostat is decreasing, and the additional heat must be compensated with a higher LN_2 flow. The temperature sensors on the PMT support structure show when this happens.

Maintenance during normal operation

On average, the 400 l LN_2 dewar for the active cooling system has to be refilled every four days. A balance below the dewar shows the weight of remaining LN_2, at maximum

360 kg. During the refilling procedure the active cooling system is run by a smaller 120 l dewar, which is adjacent to the big dewar. On one side, both dewars are connected to each other and the cooling spiral via vacuum-insulated tubes (via KV4 and KV5). On the other side, the dewars can be refilled via a direct connection to a LN_2 storage-tank outside the GDL barack (via KV3 and KV6). In parallel, the insulation vacuum is pumped, to keep it constantly below $\leq 1\times10^{-4}$ mbar (P5). With the currently used turbo pump (TP1) a pressure of $\leq 2\times10^{-6}$ mbar can be reached. During the refilling and pumping operation all measurements are interrupted.

The GAr for flushing the shielding volume around the cryostat is provided by the evaporation of LAr from a 100 l dewar outside the barrack. In emergency cases, the shielding can also be flushed from the evaporated LN_2 of the active cooling system (through V5).

2.3.2 Flushing & Filling

For filling of the cryostat transportable argon dewars (in the PID: 240 l) under high pressure (up to 6 bar) are connected to a vacuum-insulated valve-panel outside GDL. Interconnected between panel and dewar (between V18 and KV9/KV10) is an active-charcoal trap (602 g of CarboAct) to remove radon from the LAr, followed by a Teflon® filter against (charcoal) particles. At least for one day prior to filling, the trap and tubing up to the valve panel are baked at 140 °C at 10^{-4} mbar, to release previously accumulated contaminations. For filling the trap is cooled with LAr from the outside. At the valve panel one can choose between two vacuum-insulated tubes, which transport the argon into the cryostat; one tube going to the bottom (via KV10) of the cryostat, and one to the top of the final filling level (via KV9). The cryostat is precooled by the active cooling system. Yet, flash-gas which arises is released through exhaust valves (V7B, SV5) or other temporary openings.

For flushing of the cryostat the same filling infrastructure is used, with two differences: 1) the radon trap is bypassed (via V14); 2) the LAr from the 240 l dewars is evaporated before entering the evacuated tubes. This was done by simply interconnecting a long, not-thermally isolated tube. Prior to the second LAr filling (in February 2010), we actively heated up the gas with a designated 3 kW gas heater.

2.4 Photomultiplier tubes

2.4.1 Photomultiplier basics

To begin with, some basic properties and terminology of the photomultipliers are resumed here. When light hits the photocathode, it can knock out electrons via the photoelectric effect, called photo electrons. The probability for this to happen for the incidence of a single photon is called the *quantum efficiency*. An electric field inside the PMT accelerates the primary photo-electrons towards the first dynode, from which it can knock out further (secondary) electrons. These are accelerated to the next dynode, which lies on an increased electric potential compared to the previous one, and so forth until the avalanche of electrons reaches the anode. The collected charge gives rise to a signal pulse, which is proportional to the intensity of the detected scintillation light, and therefore to the deposited energy. The number of secondary electrons collected on the anode per primary photo-electron is called

the *gain factor* of the PMT. It depends on the PMT type and the operational voltage. The smallest possible signal is produced by a PMT, when only one photo electron is knocked out of the photocathode, called the *single photo electron* (spe) signal. The amplitude of this characteristic signal is determined by the gain factor, whereas its width depends on the spread of the PMT. In LArGe, the PMTs are operated at a gain factor of 10^6 to 10^7, which corresponds to a spe-signal amplitude of approximately 3-10 mV. A spe-signal is not necessarily created by light hitting the photocathode. Also thermoemission, cosmic rays, and other background radiation may randomly trigger such an event; the frequency at which this happens is called the *dark rate* of the PMT.

2.4.2 Photomultipliers in LArGe

Out of the nine PMTs from the manufacturer ETL[2], eight of them are type 9357 FLB with flying leeds, and one is type 9357 KFLB with a socket connector – the former Mini-LArGe PMT. The PMTs are equipped with custom made voltage dividers, which are operated in GAr. The 8" (200 mm) diameter end window with a low resistance bialkali photocathode is sensitive to wavelengths from 275-630 nm[3] The peak quantum efficiency of the PMTs is 18% at 370 nm. Since the glass of the end window is not transparent for the 128 nm scintillation light, and to shift the wavelength into the sensitive range, it must be covered with WLS. As mentioned above, the glass itself is ETL ultra-low background glass – specific activities are given in table 2.1.

2.4.3 Design of voltage divider & cables

The LArGe PMT voltage-divider is a joint development by Jinr (Joint Institute for Nuclear Research, Dubna) and Mpik. It was designed in the light of the experience gained from the Mini-LArGe investigations, and is devised to meet four criteria: 1) a high-quality pulse-shape is important for pulse shape discrimination of the slow and fast components of the scintillation light. By operating the PMT with negative HV on the cathode, the anode signal can be read out directly. As a result, the signal quality is improved and overshoots due to AC coupling at positive HV are avoided. 2) the voltage divider has a high dynamic range from 2 mV to 4 V, by enabling the simultaneous readout of anode and last dynode (D12). This is necessary to simultaneously handle low energy signals, such as single photo electrons from the slow component (a few mV amplitude), as well as high signal amplitudes from alpha particles (several volts possible). As it turned out, however, the achieved photo-electron yield with LArGe so far is much lower, than it was with Mini-LArGe. Therefore, the readout of the last dynode is unnecessary in this work. 3) high radiopurity: the voltage divider is based on a 0.5 mm thin CuFlon®[4] printed circuit board (PCB). CuFlon and SMD[5] components were screened for radiopurity and selected for low mass. A photograph of the loaded PCB is shown in figure 2.12, the circuit diagram is depicted in figure 2.13. 4) the PCB is required to operate at cryogenic temperatures in argon gas atmosphere. This issue is discussed in the following section.

[2] now: ET enterprise Ltd
[3] wavelength range over which quantum efficiency exceeds 1%, according to the data sheet.
[4] Teflon® (PTFE) covered with copper
[5] 'surface mounted devise'

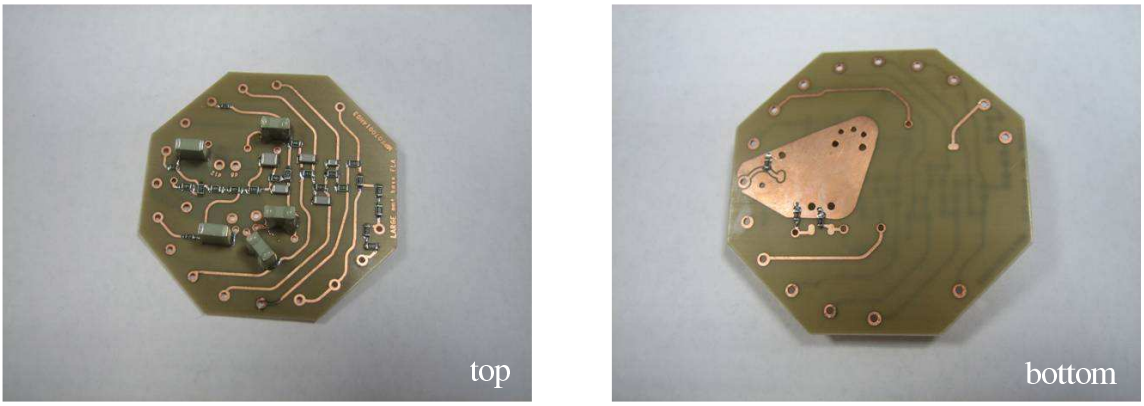

Figure 2.12: Pictures of the printed circuit board (PCB) of the LArGe PMT voltage dividers. Left: top side. Right: bottom side.

For HV and signal cables 3 m long 50-Ohm PTFE-coaxial Habia cables[6] (type SM 50) are used. They have a low mass (only 1 mm diameter) and high radiopurity. The feedthroughs in the shielding are gastight SMA RF-connectors[7] for the signals, and LEMO HV-connectors[8] (S-series) for the HV. The cable feed through in the cryostat's top flange is solved connector-free by glueing the three cables of each PMT into 1/4" Swagelok® tube fittings, which are fixed to designated copper tubes welded to the cable flanges – see the photograph A.21 in appendix A. Outside of the shielding, standard 10 m BNC cables are used for the connection with the front-end electronics.

2.4.4 Spark discharges on voltage dividers

Throughout this work spark discharges on the voltage dividers in gaseous argon (GAr) have been a major issue. The low dielectric strength of GAr and bias voltages of -1000 V to -1600 V lead to discharges, which on the one hand require an automatic shutdown of the HV, and on the other hand have an influence on other PMTs.

The new voltage dividers were first tested for discharges on a PMT, which was put in a plasic bag filled with GAr at room temperature. At HV above -1700 V spark discharges were observed. The location of the discharge was identified by an overlay of two photographs. One was taken with a long exposure time (>1 min) in darkness while the discharge ocurred, and another one was taken from the same camera angle at light – see figure 2.14. The discharge arc follows the surface of an insulated cable loop, which carries HV. The problem was fixed with small PTFE rings around the cable, to increase the path length across the insulator surface from one end to the other. Subsequently, all PCBs were equipped with PTFE rings and tested in GAr (without PMT) at -2100 V (dark current: 178 μA) for more than 20 hours each. During the integration test at MPIK, and later in the final setup at LNGS, the PMTs showed no spark discharges while the cryostat was filled with GAr at room temperature, or with cool GAr at -50 °C to -80 °C.

[6] product of the company Habia Cable AB, Sweden
[7] by Huber+Suhner, Switzerland
[8] by LEMO S.A., Switzerland

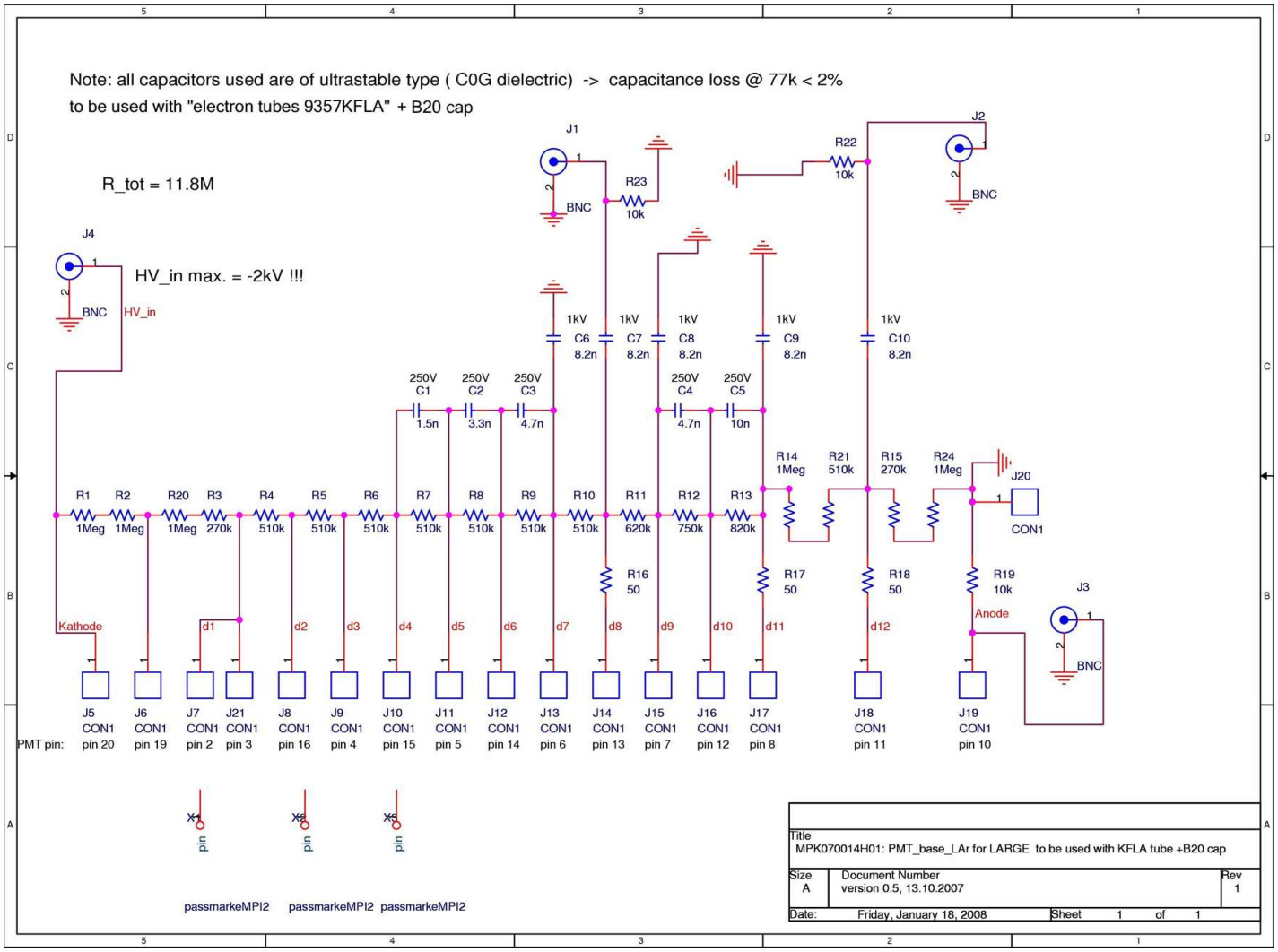

Figure 2.13: Circuit diagram of the custom-made LArGe voltage-divider.

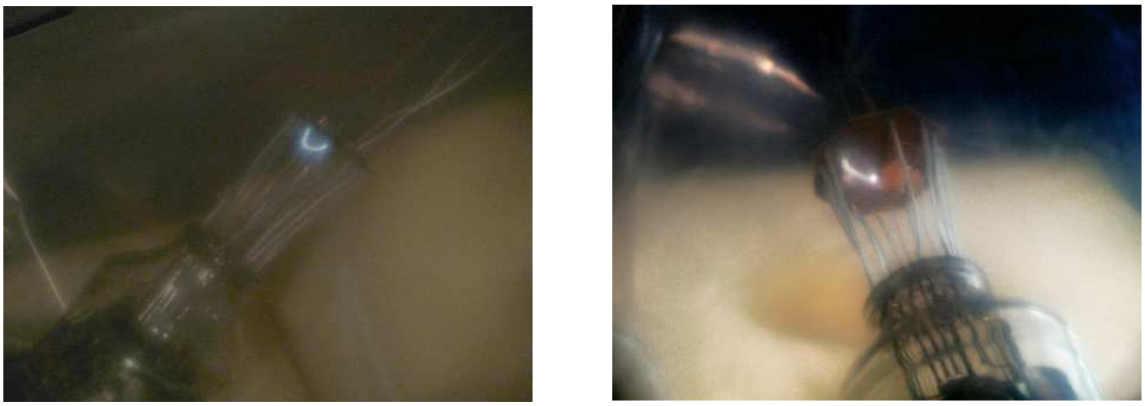

Figure 2.14: Pictures of spark discharges on the PCB in argon gas atmosphere. Each picture is an overlay of two images from the same camera angle: one taken in darkness while sparking occurs; the other one at light, to locate the spark position on the PCB.

Once the cryostat was filled with LAr, the situation became increasingly worse: At first, during the integration test, two PMTs proved problematic and got exchanged by tested spare PMTs. Later at LNGS, only six PMTs were fully operational after the first LAr filling. And by the time of the suppression measurements, after several weeks of operation and the second LAr filling, only 4-5 PMTs remained. A variety of phenomena has been observed, which cannot be fully explained yet, but which ultimately result in discharges. While some PMTs are effected strongly and fail, others seem to be much more robust:

- while ramping up the HV, the dark rate (DR) is increased and the PMT's baseline is unstable. It takes several hours to stabilize once the ramping-up is stopped. If the HV is driven up too quickly, a discharge can occur, even hours after nominal HV is reached. Our ramping-up procedure was therefore adapted to increase the HV gradually over one week time.
- one PMT induces additional DR into other PMTs. While the typical DR of our PMTs is ∼3.5 kHz in LAr, it raises by another 2-3 kHz when the HV of the faulty PMT is driven up. In some cases the DR continues to increase further for several minutes after the faulty PMT reached nominal voltage, until a discharged occurs. Naturally, the faulty PMT was put out of operation.
- discharges lead to 'thunderstorm-like' events, when the power supply modules are not set to automatically shut down HV: the discharged PMT seemingly continues to discharge uninterruptedly, which effects other PMTs. The DR of all PMTs increases up to 2 MHz, while an overload of saturated signals is created. Once the responsible PMT is switched off, the DR in the other PMTs decreases slowly below 10 kHz within one hour; but does not return to its original value, unless the HV is ramped up from scratch.

The last phenomena is partially explicable by an electric glow discharge, the emitted light of which is detected by other PMTs. However, an explanation of the various dark rate changes on the time scale of hours to days, is not found yet. Since these phenomena compromise the reliability of the scintillation light detection, we recommend systematic investigations

to understand and solve this issue. As a consequence of the encountered problems, we recalibrated the PMTs several times at a lower gain.

2.4.5 Calibration

The goal of the calibration is to fix the PMTs to the same gain factor, respectively the same spe-signal amplitude. For measurements with a MCA this means, that the position of the spe-peak in the charge/energy-histogram is fixed to the same channel. On the one hand, this is necessary for the measurement of the photo-electron yield (chapter 3), on the other hand it is easier to fix a veto-threshold in the analysis, when the spe-signals of all PMTs have a similar amplitude (charge). The procedure for the calibration is the following: the spe-signal amplitude of a reference PMT is fixed to 3-10 mV, by applying a corresponding operational voltage. Now, MCA spectra of the spe-peak are taken for all PMTs. The operational voltage of each PMT is adjusted, so that the spe-peak positions match with the reference PMT. For finetuning, a function is fitted to the spe-peaks to determine their position above the pedestal.

Figure 2.15 shows the front-end-electronics layout for the calibration measurements: the PMT is supplied with high voltage (by Iseg NHQ 204M or 225M NIM-module, both types are used), and its voltage-signal from the voltage divider (VD) is amplified by a factor ten (Phillips Scientific Mod. 776 NIM). The output signal of this amplifier is integrated and amplified by a spectroscopy amplifier (Ortec Mod. 572 NIM) with a shaping-time constant of 0.5 μs, the output of which is fed into a multichannel analyzer (MCA, Ortec Mod. 927 NIM). The measurements are controlled and recorded from a PC using the Maestro-32

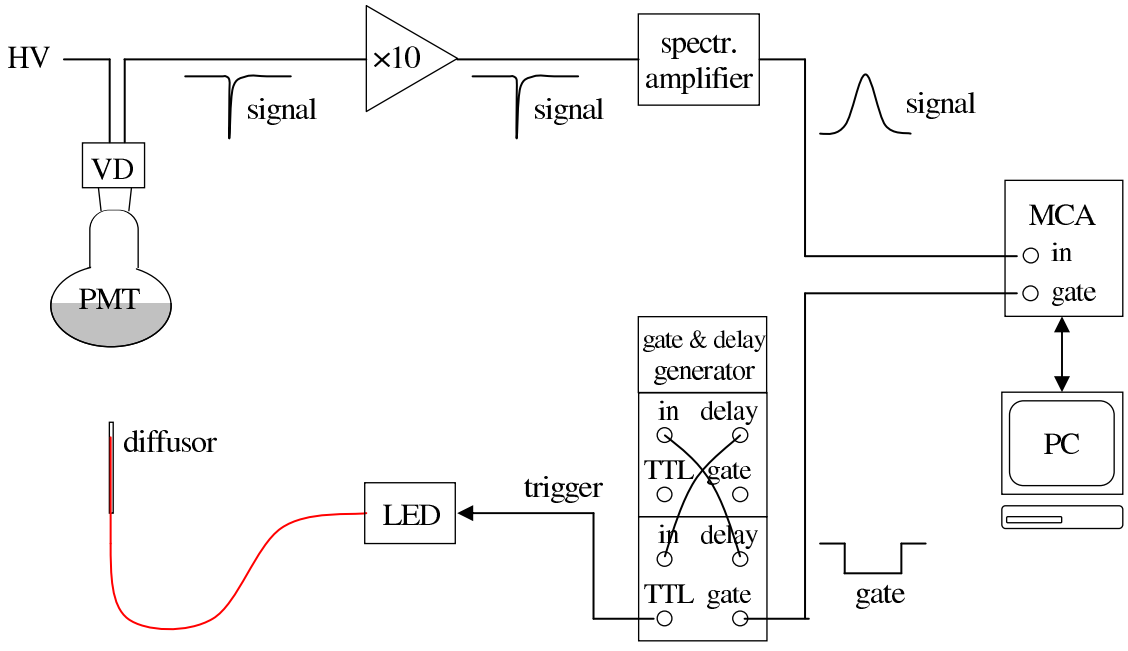

Figure 2.15: Front-end-electronics layout for PMT calibration measurements with a multichannel analyzer (MCA). VD = voltage divider; '×10' = amplifier.

software (by Ortec). In a second branch, a common trigger with 1 kHz is generated by a flip-flop setup on a gate-and-delay generator (Philips Scientific Mod. 794 NIM): on one side a TTL signal triggers an UV-LED, while on the other side a gate for the MCA is generated, to record the PMT signal corresponding to an LED pulse. The custom-made LED emits short pulses ($\tau = 3$ ns) of UV-light ($\lambda = 380$ nm) with adjustable intensity. The light is guided to the PMTs by optical-fibres, including two optical feedthroughs and a self-made glass-diffusor, which distributes the light isotropically in the cryostat. Three such optical-lines are available to reach each group of PMTs.

Single-photo-electron signals are created by adjusting the intensity of the LED such, that the PMTs detect light in only one out of 30 trigger signals. The number of photons N registered by the PMTs is Poisson distributed, with the mean value λ determined by the light intensity:

$$p_\lambda(N) = \frac{\lambda^N}{N!} e^{-\lambda}$$

From the given probability to detect zero photons $p_\lambda(0) = 29/30$ one can calculate $\lambda = 0.034$, and hence the probability for the detection of a single photo-electron $p_{0.034}(1) = 0.033$. For comparison, the probability for multiple photons is $p_{0.034}(> 1) = 0.009 < 1\%$. Thus, the energy spectrum is dominated by spe-signals.

Figure 2.16 shows the calibration spectrum of PMT #9 taken in GAr prior to the 1st LAr filling; the spe-signal amplitude is on average 10 mV. The pedestal is cut-off at low energies, due to a threshold set in the MCA (below channel 10). The shape of the histogram – i.e. the superposition of the pedestal, the spe-peak, and higher order photo-electron peaks – can be described by a series of Gaussian distributions of different weight [45]. For our purpose, however, a simplified fit function $f(x)$ is sufficient:

$$f(x) = a \cdot e^{-bx} + \sum_{n=1}^{3} c_n \cdot G(n\mu, \sqrt{n}\sigma)$$

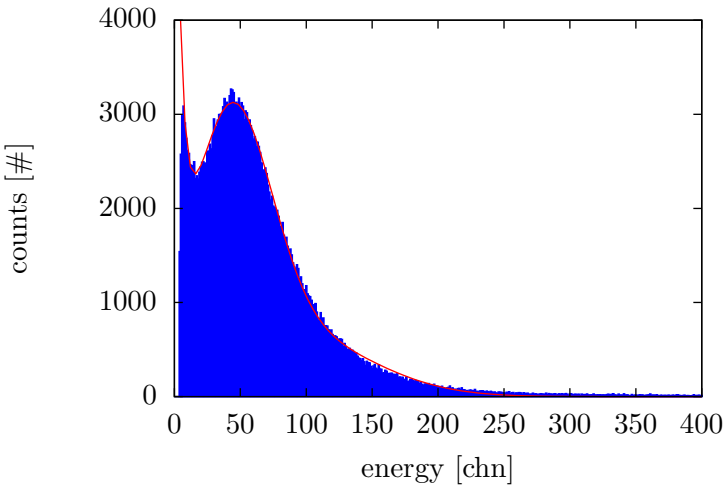

Figure 2.16: Calibration spectrum of PMT #9 in GAr at room temperature, taken prior to the first LAr filling. The spe-signal amplitude is adjusted to 10 mV. The pedestal and the spe-peak is fitted (see text) to determine the peak position.

Table 2.3: Shown are the nominal PMT voltages from the calibration runs. Prior to each LAr filling of the cryostat the PMTs were calibrated for measurements in GAr at room temperature, and after each filling they were calibrated in LAr. The voltages in brackets refer to the amplitude of the single-photo-electron signal, which is determined by the gain-factor.

PMT	1st filling		2nd filling	
	GAr (10 mV)	LAr (7 mV)	GAr (3 mV)	LAr (3 mV)
#	[-V]	[-V]	[-V]	[-V]
1	1141	1160	1040	1145
2	1265	1240	1140	1230
3	1335	1320	–	–
4	1620	–	–	–
5	1460	1455	1350	1485
6	–	–	–	–
7	1510	1450	1300	1470
8	1410	1400	1290	1410
9	1120	1140	–	1120

The exponential function with fit parameters a and b represent the pedestal, which is dominated by electronic noise. The gaussian functions $G(n\mu, \sqrt{n}\sigma)$, with mean value $n\mu$, standard deviation $\sqrt{n}\sigma$, and a normalization constant c_n, describe the respective distribution of PMT signals with n primary photo-electrons ($n = 1$ for spe-signals). Higher order signals are negligible. The correlation between photo-electrons (pe) and MCA signal is expressed by the pe-to-MCA gain-factor given by the mean value μ of the spe-peak, to which the PMTs are calibrated. In case of the example in figure 2.16 the pe-to-MCA gain-factor is $\mu = (42.3 \pm 0.2)$ chn, the fit function $f(x)$ is shown by the red curve.

As mentioned earlier, due to the repeated problems with PMT discharges, the PMTs had to be recalibrated at different gain-factors several times. Also, the gain is temperature dependend: thereby, for each LAr filling of the cryostat one calibration run was carried out for PMTs in GAr at room temperature (for measurements prior to filling), and one with the PMTs immersed in LAr. Table 2.3 shows the determined nominal voltages obtained from the different calibration runs, which apply for the measurements presented in this work. Instead of the pe-to-MCA gain factor, which is incomparable among the calibration runs due to changed gain-settings of the spectroscopy amplifier, the spe-signal amplitude in mV is provided as a measure of the PMT gain. PMTs without nominal voltage could not reach the required gain before discharge problems occurred.

2.5 Germanium detectors

2.5.1 BEGe detector

The broad-energy-germanium (BEGe) detector is the first Ge-diode submerged into the LArGe cryostat, and has been used to carry out the suppression-efficiency measurements

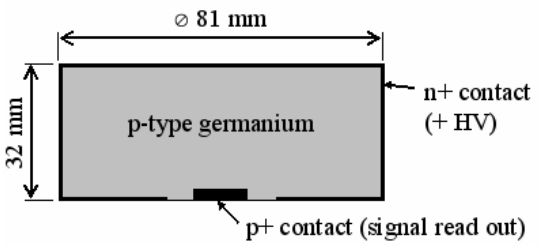

Figure 2.17: Schematic drawing of the p-type broad-energy Ge-detector (BEGe), manufactured by Canberra Semiconductors, N.V. Olen. The weight of the crystal is 878 g.

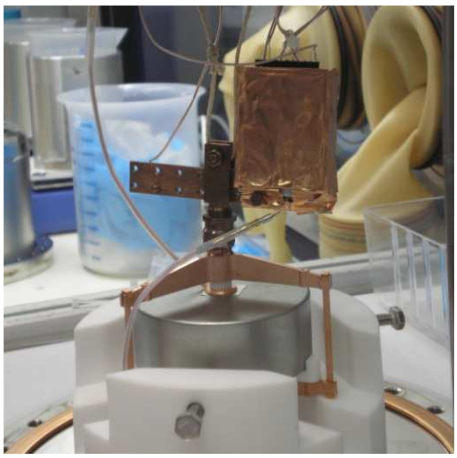

Figure 2.18: Photograph of the BEGe detector in its low-mass copper-holder, with the prototype CC2 preamplifier attached inside a copper box.

presented in chapter 4 of this work. With a mass of 878 g, it is the largest conventionally available BEGe detector by its manufacturer Canberra Semiconductors, N.V. Olen/Belgium. The BEGe diode is p-type: a positive bias HV is applied on a Li-drifted $n+$ contact covering the outer surface. A passivated groove separates the small electrical $p+$ contact, from which the signal is read out – see figure 2.17. The small read-out electrode leads to a large variation of the electrical field in the diode, which is exploited to reject background events using pulse shape discrimination. According to the manufacturer, the depletion voltage is +4 kV, and the front dead-layer has a thickness of 500 μm. A description of the detector is given in [46].

The diode is mounted to a low-mass copper-holder, like it is used in GERDA, and is submerged 'naked' into LAr, i.e. without further encasing. Its operation and performance in LAr has been thouroughly investigated [47]. A multi-channel charge sensitive preamplifier ('CC2') has been developed and tested in the framework of the GERDA experiment [48], a prototype of which is used in LArGe. It is designed for cryogenic temperatures, and is mounted on the copper-holder close to the detector – see figure 2.18.

2.5.2 GTF44 detector

The GTF44 detector is a coaxial p-type HPGe-diode (HP = high purity) of high mass (2465 g), which is used for the first background measurements in LArGe, presented in chapter 5. It is made from germanium with a natural isotope composition, and has been kept underground since its operation in the Genius Test Facility (GTF). The detector has been modified by the manufacturer Canberra for the bare operation in LAr [49]. It is equipped with a low-background version of the CC2 charge sensitive preamplifier [50].

Within the scope of an investigation program about ^{42}Ar background in GERDA and LArGe, the diode has been encapsuled in a grounded Faraday cage, to shield the argon from the detector's electric field and avoid the drift of ions in the surrounding LAr. The encapsulation is made from an inner PTFE cup for insulation (wall thickness $d = 0.5$ mm, mass $m = 38.8$

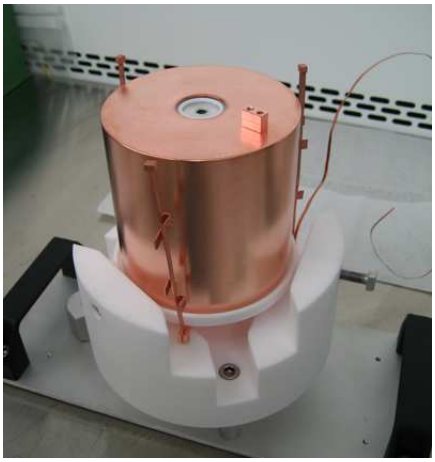
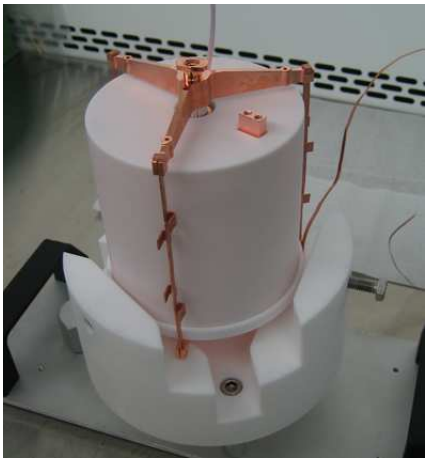

Figure 2.19: The GTF44 detector being mounted to its encapsulation. **Left:** the copper cup. **Right:** the outer PTFE cup and the low-mass copper holder.

g), a copper cup with electrical contact ($d = 1.5$ mm, $m = 441$ g), and an outer PTFE cup ($d = 1$ mm, $m = 99$ g). Photographs are shown in figure 2.19. Recent results from the ^{42}Ar measurements with this detector are also shown in chapter5.

2.6 Front-end electronics and DAQ

2.6.1 Simultaneous readout of Ge-detector and PMTs

For the application of the LAr-scintillation anti-coincidence veto the signals from Ge-detector and PMTs must be read-out simultaneously. A scheme of the front-end electronics layout is depicted in figure 2.20. Again, the PMTs' voltage dividers (VD) are supplied with operational HV (by Iseg NHQ 204M or 225M NIM-modules, both types are used), and their individual voltage-signals are amplified by a factor ten (Phillips Scientific Mod. 776 NIM). Next, the signals are merged in a linear fan-in (LeCroy Mod. 428F NIM), to build the analog-sum of the utilzed PMT signals. The output is connected with a custom-made analog shaper (by MPIK, NIM), which amplifies the signals with a shaping constant of a few 10 ns, and inverts them to match the input dynamic-range (-1 V to +4 V) of the subsequent flash ADC (FADC). The FADC (Struck SIS3301 VME; 8 channels, 14-bit, 105 MS/s) is mounted into a VME-crate (Wiener).

The preamplifier of the Ge-detector is supplied with bias HV (Iseg NHQ 225M NIM). A pulser signal (Ortec Mod. 448 NIM) can be fed into a test input of the preamplifier, when needed. The output signal is amplified without shaping by another home-made (linear) amplifier. Again, the purpose is to fully use the available input dynamic-range of the FADC, to reduce its noise contribution and take full advantage of the 14-bit FADC amplitude resolution. The FADC is internally triggered by the Ge-signal, and simultaneously records Ge- and PMT waveforms of 40 μs trace-length with 100 MHz sampling rate. The FADC aquisition is controlled by a custom-made software by MIZZI Computer Software GmbH [51].

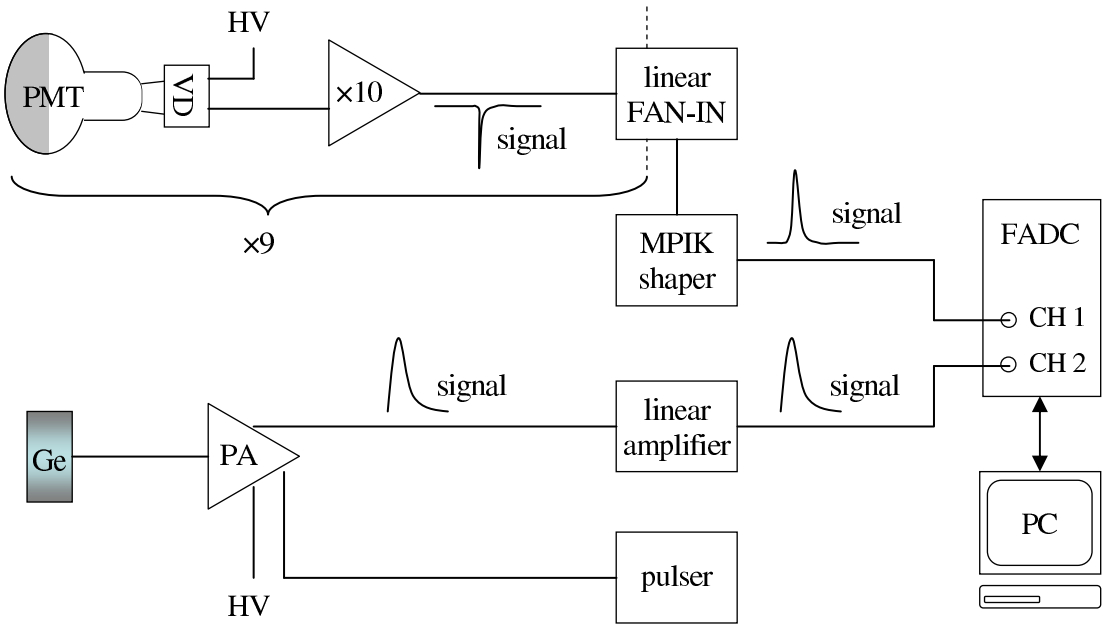

Figure 2.20: Front-end electronics scheme of the Ge-detector and PMT readout. The system is triggered internally on the Ge-detector signal, hence simultaneously recording 40 μs of Ge- and PMT-waveforms. VD = voltage divider; PA = preamplifier.

2.6.2 Separated PMT readout

The electronic layout presented here is used for the investigation of scintillation light with a MCA or a digital oscilloscope, avoiding the somewhat more cumbersome work with a FADC; see figure 2.21 for the front-end electronics scheme. In the top branch, the PMT signals are summed-up in a linear fan-in, and passed through a spectroscopy amplifier into the MCA – as described above in sections 2.4.5 and 2.6.1. A digital oscilloscope (Tektronix DPO7104) is used to record waveforms of single PMTs.

A common 'multiplicity-trigger' for both MCA and oscilloscope is generated by two consecutive leading-edge discriminators (Phillips Scientific Mod. 710). The idea is to trigger only on signals, when a minimum number of n PMTs fires simultaneously, called an n-fold coincidence. Our default, a 2-fold coincidence, already allows to effectively filter real scintillation-signals, which appear in multiple PMTs, from randomly occurring dark pulses. First, the individual PMT signals (amplified by a factor ten) are discriminated with a threshold of 1/3 to 1/2 of the spe-signal amplitude. For instance, with an average spe-amplitude of 10 mV (100 mV after amplification) the threshold is set to ∼40 mV. The sum-output of the discriminator creates a step-shaped signal, which is composed from the logical NIM-signals (width 100 ns) of the individually discriminated PMTs. Now, the second discriminator imposes a threshold on this step-signal: by choosing the threshold accordingly, one can demand a minimal number of steps for the discriminator to pass on the signal (as a NIM-signal); the number of required steps determining the n-fold multiplicity-trigger condition. The multiplicity-trigger signal is distributed to the digital oscilloscope and the MCA via a logical fan-out. A scaler (Caen Mod. 145 NIM) is used to measure the dark rate of individual PMTs, and the rate of the multiplicity trigger.

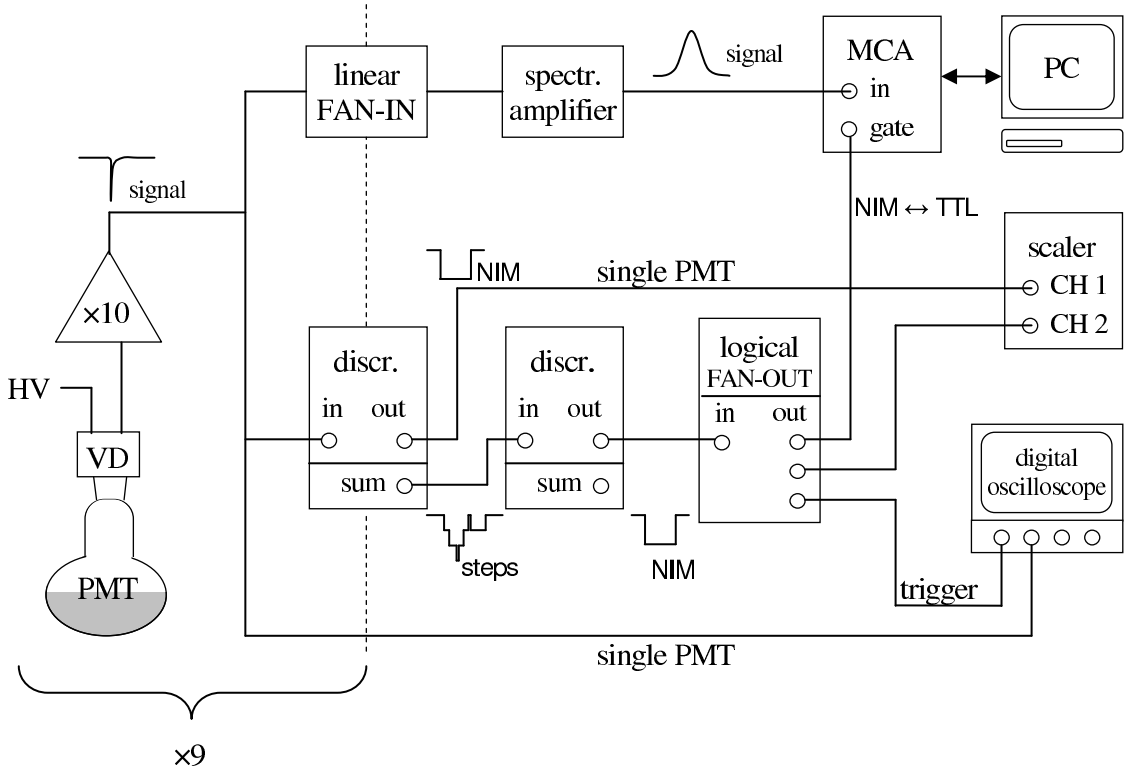

Figure 2.21: Front-end electronics layout for the PMT readout with the MCA. The diagram also shows the aquisition scheme for PMT traces with the digital oscilloscope, as well as for dark rate measurements with the scaler. A multiplicity trigger is generated from the logical sum of the individual PMT triggers (see text for explanation), and is distributed to the three aquisition branches. 'ref. PMT' refers to the signal of a single PMT, which is picked for the particular measurement.

Chapter 3

Liquid argon purity & scintillation light detection

This chapter covers the commissioning phase of LArGe, and the persistent problem of scintillation light quenching due to trace impurities in the LAr. The causes for the argon contamination were found to be air diffusion into the cryostat and presumably residues of humidity. After a second filling of LArGe with LAr in February 2010, the scintilliation light remained stable during several months of operation, and with sufficient light yield to run the active background suppression together with Ge-detectors. However, the photo-electron yield was still too low to permit light spectroscopy and pulse-shape discrimination with the photomultipliers, as it was demonstrated with the Mini-LArGe setup [36, 37].

3.1 Argon scintillation

3.1.1 Excimer formation and light emission

Ionizing radiation which passes through argon, can either excite or ionize the argon atoms [52, 53]. Both mechanisms lead to the creation of neutral excimers Ar_2^*, which ultimately decay into two argon atoms by the emission of 128 nm scintillation light [54] (figure 3.1). Excitation leads to the formation of the excimers through collisions with neighboring atoms. In case of ionization, the electron thermalizes and recombines with the ionized atom on a timescale of $\mathcal{O}(100)$ ps. The emitted photons, are highly likely of being reabsorbed and form secondary excitons – i.e. the argon is not transparent to this recombination luminescence. However, it is possible that an ionized dimer Ar_2^+ is formed from the initial ionized argon atom and a neutral partner, before the thermalization of the electron takes place. The recombination of an electron with the dimer leads to a highly excited state, which de-excites non-radiatively and forms the excimer Ar_2^* [57]. Both excimer formation mechanisms are strongly pressure and density dependent: excitation dominates in gaseous argon at normal pressure and room temperature, whereas ionization is important in liquid argon [58, 59].

The argon excimers are created either in singlet or triplet states, with the population ratio being dependent on the type of causative radiation, e.g. electron, neutron, or α-particle [60]. The decay of the singlet and triplet states occurs with characteristic time constants

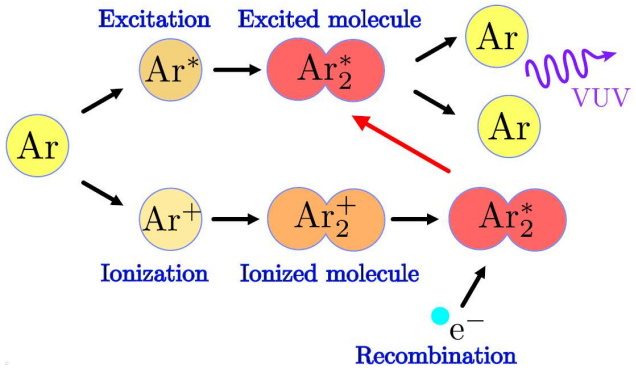

Figure 3.1: The two excimer formation mechanisms, which lead to the emission of 128 nm scintillation light; adopted from [55, 56]

τ, by which the states can be distinguished. While the decay of the singlet state is allowed (also called 'fast component', $\tau_s = 6$ ns), it is forbidden for the triplet state by angular momentum conservation. In liquid argon the triplet lifetime is about $\tau_t = 1.5$ μs – also referred to as the 'slow component'. Together, both components have a scintillation *light yield* of 40 photons per keV energy deposition in ultra-high purity LAr [61].

3.1.2 Triplet state lifetime as an indicator for impurities

Trace contaminations in liquid or gaseous argon lead to a reduction of the triplet lifetime [62]. The reason is presumably a depopulation of the triplet state due to collisional destruction with impurities, such as water, nitrogen, or oxygen. This non-radiative process is in competition with the XUV light emission, and leads to quenching of the light yield. For the singlet state almost no quenching is observed, as the de-excitation time is too short to be affected by collisions. The dependence of the triplet lifetime on the impurity level has been studied for air contamination in GAr [55, 63], and for N_2 and O_2 impurities in LAr [64, 65]. The triplet lifetime is a good measure of impurities, because it is independent of the detection efficieny of the instrumentation, and also independent of the type and energy of the initial particle triggering the scintillation. Therefore it can be measured with arbitrary sources.

Figure 3.2 shows the average PMT pulse shape in GAr, measured in LArGe with a ^{148}Gd pure α-source. Ten thousand PMT waveforms were recorded with a digital oscilloscope using a 3-fold multiplicity trigger – the DAQ layout is presented in section 2.21. The waveforms are averaged offline, and an exponential fit to the slow component yields the triplet lifetime. In this example, the pulse shape in the left plot yields $\tau_t = 3.41$ μs, which is in agreement with the expected decay time (3.2±0.3) μs for high-purity GAr [55]. Shown in the right plot is the pulse shape of a contaminated GAr sample, where the triplet state is strongly quenched and only the fast component remains. Pulse shapes in LAr look comparable, with the difference of shorter maximal lifetimes of the slow component.

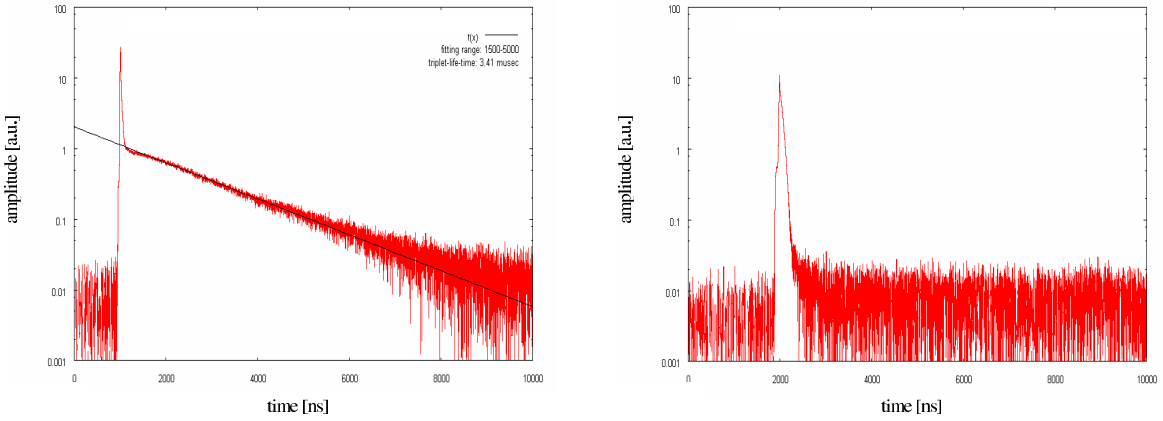

(a) clean GAr **(b)** contaminated GAr

Figure 3.2: Average PMT waveforms in GAr, measured with a ^{148}Gd pure α-source. The slow component of the scintillation light is strongly quenched in the contaminated gas, while the fast component remains. The fit to the triplet component (black line) in the clean sample yields a lifetime of $\tau_t = 3.41$ μs.

3.2 Overview on argon contamination issue

3.2.1 Commissioning phase & search for impurities

Prior to first filling (October 2009). After completion of the assembly, the cryostat was flushed with Ar 5.5 (99.9995% purity) for several days to remove air residues. First scintillation light was observed in GAr using a ^{148}Gd α-source[1] ($Q_\alpha = 3.3$ MeV). A degradation of the light yield[2] was measured as a function of time for several hours after flushing was stopped, and it recovered once the flushing continued – see figure 3.3. Repeated test runs with different GAr temperatures down to -90°C showed a slowing down of the light degradation, which was presumably due to outgassing of air pockets inside the cryostat. It was decided to try a first filling with LAr.

First LAr filling (November 2009). It took more than one week to ramp-up the bias voltage of the PMTs, due to the problems discussed in section 2.4.4. Once the PMTs were operational, the scintillation light was found to be quenched: a measurement of the triplet lifetime yielded 66 ns (compare to ∼1.5 μs in pure LAr). A 39 kBq ^{228}Th-source was observable in the MCA spectrum, but still no measurement of the photo-electron yield was possible. In order to identify the contamination, we connected a Prisma QMS 200 M2 mass spectrometer[3] with a sensitivity to measure concentrations at the ppm level to the cryogenic

[1] The ^{148}Gd was implanted into the aluminum foil at an accelerator at the Joint Institut for Nuclear Research, Dubna. The source is mounted to a steel wire with a brass weight, which is lowered into the cryostat by the 'alpha source manipulator'.

[2] Energy spectra of the light were taken with a MCA. The spectra were almost featureless, but their endoint was clearly related to the detected light intensity. In fact, the observed PMT signal shape was not understood at first, as it was influenced by the electric field between the PMTs' photocathodes and the grounded steel wire.

[3] A detailed description of the mass spectrometer and its operation is found in [66]

system of LArGe (see figure 2.10). However, the impurity concentrations in LAr (7 ppm N_2, <4 ppm O_2, no other contaminations found) are not sufficient to explain the strong quenching (compare [64, 65]). Therefore, to narrow down the problem, the Mini-LArGe setup was transported to LNGS, and a test series of the triplet lifetime in various different LAr batches was conducted. The following conclusions were made: 1) the argon from the storage tank was 'clean' ($\tau_t = 870$ ns) compared to the LAr in LArGe. 2) a sample of LAr from LArGe was measured in Mini-LArGe, confirming the short triplet lifetime. 3) some possible causers for a contamination are excluded (CarboAct and PTFE filters for LAr filling, Araldit epoxy-resin). After all, air humidity remained the most likely hypothesis for the contamination.

Prior to second filling (January 2010). For a new start, the cryostat was drained. Modifications were made to increase the operation pressure range of the cryostat, in particular to be able to evacuate it by supporting the bellow. This was initially not forseen, since it foils the purpose of the bellow to increase the thermal resistance between top flange and the cold bottom part of the cryostat. With the possibility to pump the cryostat, several small leaks were discovered and fixed[4]. The diffusion of air through the various seals of the top flange into the cryostat against overpressure (30 - 80 mbar) was verified by the mass spectrometer running in a dynamic mode: by flushing the top flange with different gases (Ar, N_2, air), their ingrowth into the pure GAr atmosphere inside the cryostat was observable over time. As a consequence, the whole inner shielding volume around the cryostat is now constantly flushed with GAr, instead of using the initially forseen exhaust gas GN_2 from the active cooling system. Eventually, to remove traces of air humidity, we performed over 50 pumping-flushing cycles during two weeks, and heated up the cryostat wall to $\gtrsim 40°C$. One cycle consists of pumping down the cryostat to $\leq 2 \cdot 10^{-1}$ mbar, and then flushing it with actively heated GAr using a designated 3 kW gas heater. A measurement of the

[4]A helium leak detector can only be used sporadically, since helium can diffuse into PMTs and damage them. When utilized, we flushed the cryostat with GAr immediately after.

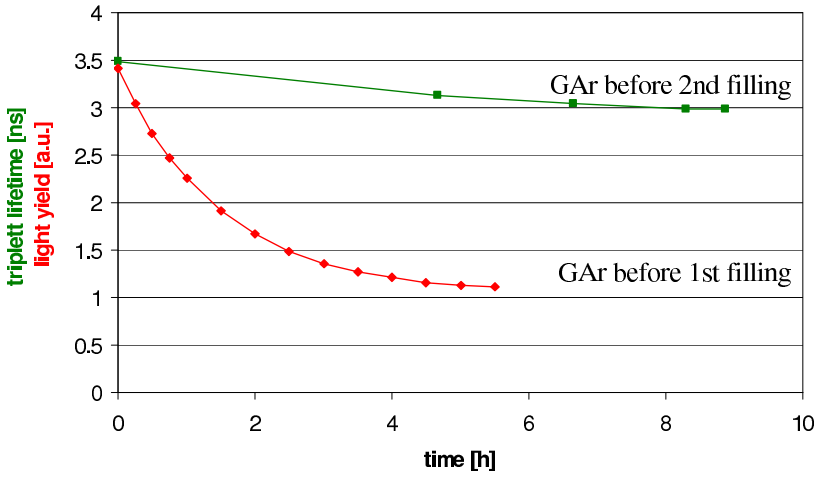

Figure 3.3: Measurements of the light degradation in GAr prior to the first and second LAr filling. Since the triplet lifetime is approximately proportional to the light yield, the degradation time constants are comparable.

triplet lifetime degradation in the closed cryostat with the α-source in GAr concluded the preparations for a second filling – see figure 3.3. The starting value for the triplet lifetime $\tau_t = 3.49$ μs is consistant with high-purity GAr, and it decreases to 3 μs after 8.9 h. In parallel to the observed degradation in this measurement, no contamination on the ppm level or above was found with the mass spectrometer.

Second LAr filling (February 2010). After the second filling with Ar 5.5, scintillation light was observed with moderate quenching of the triplet state. Figure 3.4 shows a triplet lifetime measurement immediately after the second filling, which yields $\tau_t = 826$ ns – a starting point for subsequent measurements.

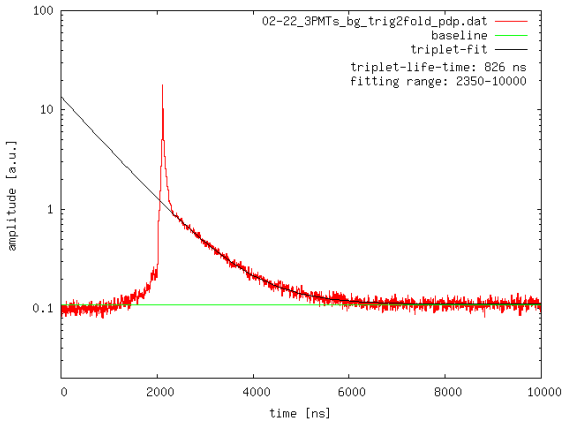

Figure 3.4: Average of 10000 PMT waveforms in LAr after the second LAr filling. Also shown is the fit to the slow component (black line) and the baseline (green).

3.2.2 Triplet lifetime longterm stability

The longterm stability of the scintillation light yield is a crucial prerequisite for its utilization as an anti-coincidence veto. Therefore, it has been monitored almost daily over the course of more than four months – measurements are shown in figure 3.5. During the first month, an average triplet lifetime degradation of 2.5 ns/d is observed. So far, the shielding at the top is opened, and only sealed with PTFE foil, so that the volume around the cryostat can be flushed with GAr under slight overpressure. After closing the shielding and mounting the lock, the degradation has almost stopped. The mounting operation itself caused a loss of ∼70 ns lifetime, since the flushing had to be interrupted and the top flange was exposed to air for several hours. Another loss of 70 - 80 ns is observed for the BEGe deployment procedure, which is described in 2.1.5, and further smaller steps occurred during mounting of the source-flange and the inner sources, despite these operations being executed under GAr atmosphere in the lock. Since the source-flange is not sealed when an inner source is inserted, impurities in the GAr from the lock (also flushed with Ar 5.5) may penetrate into the cryostat during measurements with inner sources; the observed degradation is ∼1.7 ns/d. Without inner sources the source-flange is tight, and no decline of the triplet lifetime was observed. By the time when the BEGe detector was removed, the triplet lifetime was ≈450 ns.

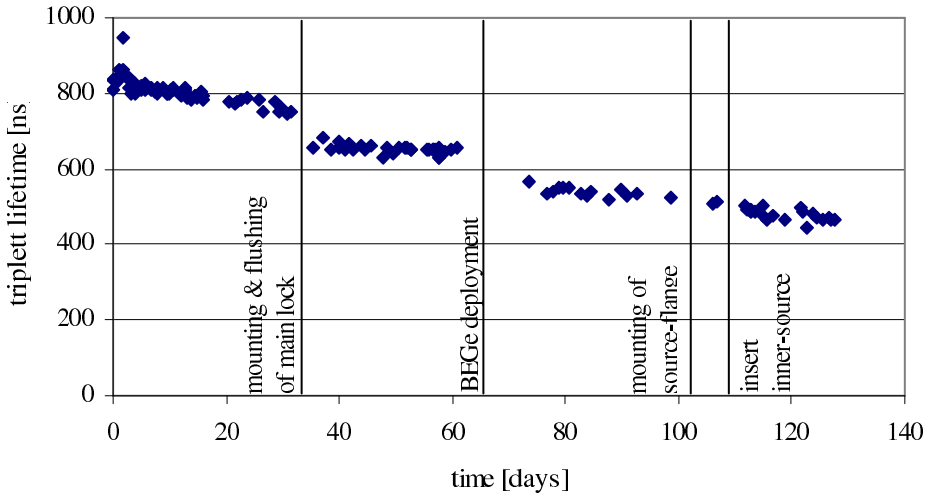

Figure 3.5: Longterm stability monitoring of the triplet state lifetime. The time is given in days after the second LAr filling of the cryostat.

3.3 Photo-electron yield

Since the average number of photo electrons registered by the PMTs is proportional to the detected light intensity, it is also proportional to the deposited energy in the scintillator. The photo-electron yield is the proportionality constant, given in units of *photo electrons* (pe) per deposited energy (e.g. pe/keV). While on the one hand the photo-electron yield depends on the scintillation light yield – a property of the argon depending on its purity (40 photons/keV in ultra-pure LAr), it is also dependent on the detection efficiency of the setup. The detection efficiency depends on the quantum efficiency of the wavelength shifter, the efficiency of light collection on the photocathodes, and the quantum efficiency of the PMTs. The light collection efficiency by itself is given by the transparency of the LAr, the reflectivity of the mirror foil, and the geometry of the system.

For a measurement of the photo-electron yield one needs a gain calibration of the PMTs, to aquire the position of the single photo-electron peak in the energy spectrum – in our case we use a MCA, see 2.4.5. The energy scale can now be expressed in units of 'average number of photo-electrons per channel'. Together with an energy calibration from a source measurement one obtains the photo-electron yield.

Figure 3.7 shows the energy spectrum of a 39 kBq external ^{228}Th-source, located on the outer wall of the cryostat. The measurement is taken two weeks after the second filling (aquisition time 10 min), with a corresponding triplet lifetime of 800 ns. The DAQ is described in section 2.6.2. The blue histogram is the net-spectrum, which is the total aquired ^{228}Th-spectrum (red) minus the background spectrum without a source (yellow). The energy resolution is too low to identify individual ^{228}Th lines, like it has been possible in the Mini-LArGe setup [37]. In order to identify spectral features, a Monte Carlo (MC) simulation of the expected source response in LAr for the given geometry was done (without smearing for energy resolution) – it is shown in figure 3.6 [67]. The 'hump' in the MCA spectrum around 135 pe is associated with the similar structure at ∼3 Mev in the MC spectrum, from which follows a photo-electron yield of $Y \approx 0.05$ pe/keV. A measurement

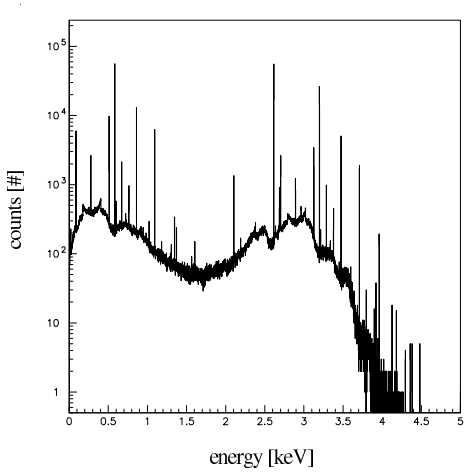

Figure 3.6: Monte Carlo simulation of the energy deposition in LAr from a ^{228}Th-source on the outer wall of the cryostat. No energy smearing was applied [67].

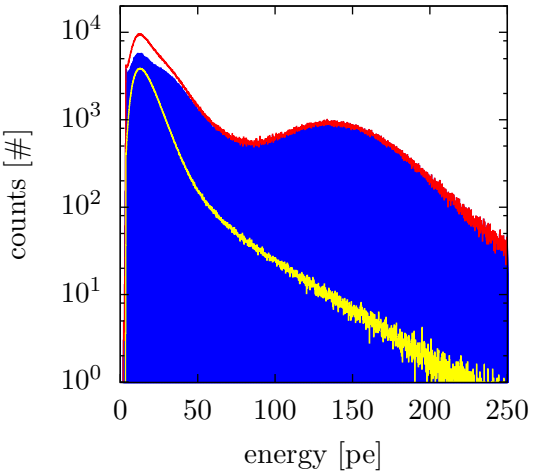

Figure 3.7: MCA spectrum of an external 39 kBq ^{228}Th-source, located on the outer wall of the cryostat. The net spectrum (blue), is the total spectrum (red) minus the background spectrum (yellow).

with other sources (^{241}Am, ^{60}Co) was not successful, since no characteristic structures could be identified in the spectra and associated with energies.

The achieved photo-electron yield is very low compared to the Mini-LArGe value (1.24 pe/keV [37]), which explains the poor energy resolution. Clearly, no scintillation spectroscopy or pulse shape discrimination can be done under these conditions. Nevertheless, the average energy deposition required for the creation of a single photo electron is 20 keV, which gives an estimate of the energy threshold of the LAr veto, and is sufficient for its operation.

Chapter 4

Background suppression measurements

This chapter presents the key measurements performed with the LArGe setup, recording gamma-spectra with the BEGe detector, while simultaneously applying the LAr scintillation anti-coincidence cut technique. Short: LAr veto.

The first half of the chapter describes the data treatment of the recorded BEGe and PMT pulses, which results in the respective cut conditions and the energy reconstrucion of the BEGe detector. In the second half, the suppression efficiency of the LAr veto is studied in combination with the *pulse shape discrimination* (PSD) cut of BEGe, for several gamma sources at different locations. This demonstrates the feasibility and efficiency of LArGe's background suppression concept on a realistic scale for ultra-low background experiments.

4.1 The LAr scintillation veto cut

The principle of the LAr veto is discussed in section 1.3.1. Briefly, when energy from ionizing radiation is deposited in the liquid argon, scintillation light is emitted, shifted to a suitable wavelength, and guided to the PMTs. Each PMT creates a charged pulse, which is composed from a number of photo electrons proportional to the initial energy deposition in the LAr. The PMT pulses are amplified, summed up, shaped, and eventually digitized by a FADC. The FADC simultaneously records the BEGe signal, by which the FADC is triggered. The electronic layout of the DAQ is explained in section 2.6.1. For both pulses, the FADC records a trace of 20 μs before and after the trigger with 100 MHz sampling rate (corresponding to 10 ns per channel). Example pulses are shown in figure 4.1. In an offline analysis of the PMT pulses, the veto condition is set such, that each BEGe signal is rejected in coincidence with one or more photo electrons, which appear in a pre-defined time window around the BEGe trigger.

4.1.1 PMT pulse processing

The output event files generated by the DAQ system are in binary format. The event traces of BEGe and PMT pulses are stored consecutively, furnished with additional information

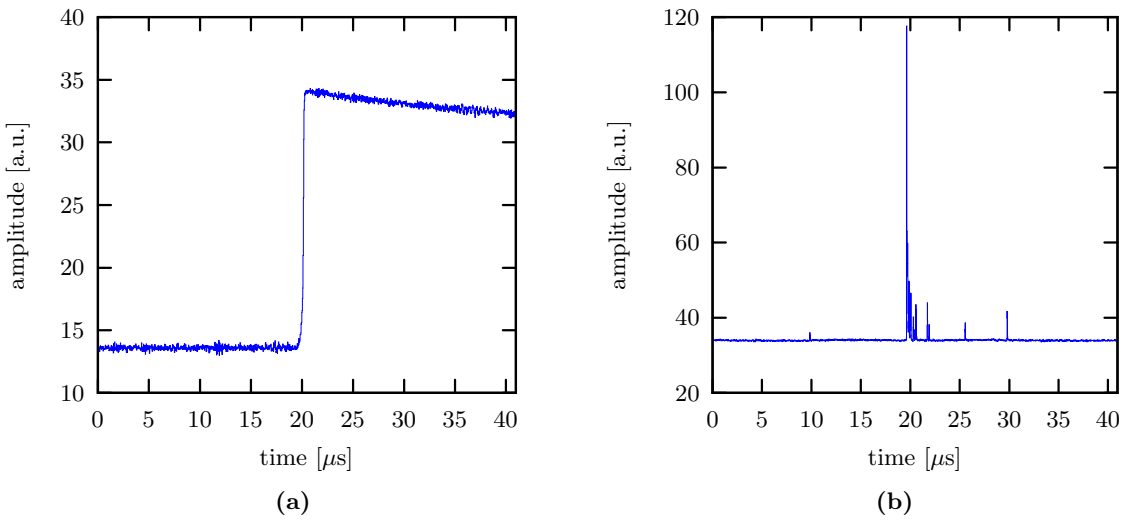

Figure 4.1: Pulses recorded with the FADC. **(a)** A BEGe pulse corresponding to an energy deposition of 609 keV. **(b)** The corresponding summed PMT pulse, composite of the single PMTs' pulses.

from an online analysis, such as energy or amplitude of the BEGe pulse. For the offline analysis of the PMT pulses, the event files are read and processed by a routine using MATLAB 7.9.0. The flowchart of this program is shown in figure 4.2.

In the first part, the program scans through the event file for tags, which indicate the type of the following information. After finding a tag it proceeds accordingly: The BEGe events are merely used to count the event number, since at this stage only the PMT events are analysed. Other tags are either read and output on screen for monitoring, or they are skipped entirely. When no tag is found, the end of the file is reached and the routine stops.

When a PMT event is found, the baseline and the baseline spread are determined in the *veto window*. The veto window is the time window to accept a veto, the position and width of which is defined prior to running the analysis routine for detail. This is done with the help of the *probability density profile* (pdp) from a run with an internal ^{226}Ra source (figure 4.3a), as described below in section 4.1.3.

To determine the baseline, first, the mean average b_0 and the baseline spread σ_0 of the event is calculated in the veto window. The baseline spread is the standard deviation of the distribution of the channels' amplitudes $A(chn)$. Then, in a first iteration, all channels are discarded, which span out of a $3\sigma_0$ corridor around b_0. The baseline parameters b_i and σ_i are recomputed, excluding the discarded channels from the calculation. This is repeated in further iterations, until the baseline's mean average b_i changes by less than its uncertainty $\bar{\sigma}_i$, which is just $\bar{\sigma}_i = \sigma_i/\sqrt{n-1}$, with n being the number of used channels. Typically, the baseline is approximated well with about six iterations. Events with a large number of photo electrons require more. See figure 4.3c for an example of the baseline and its spread after three iterations.

Eventually, the program calculates the energy of the PMT pulse and checks the veto condition using the *veto threshold*. The energy is obtained by subtracting the baseline from

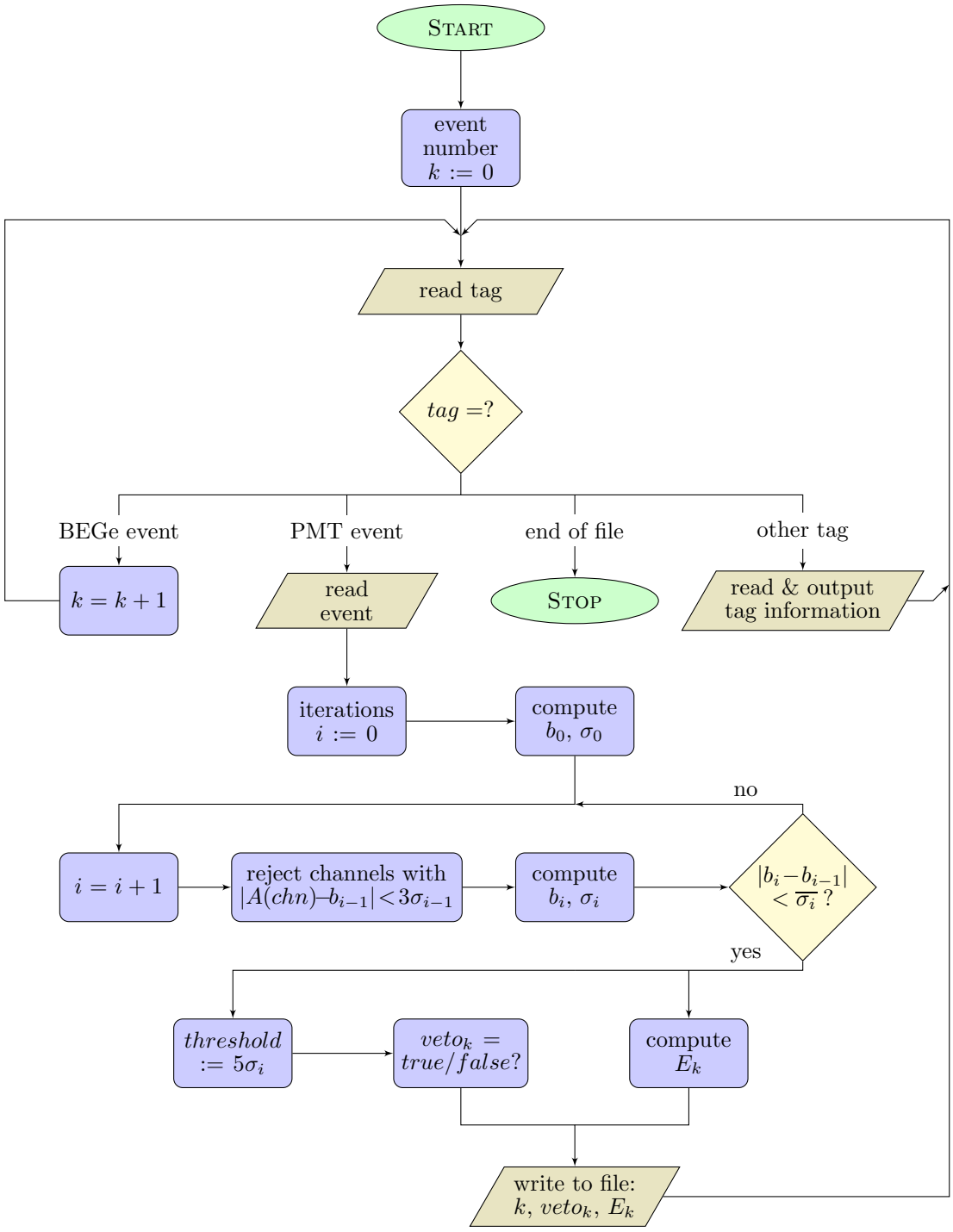

Figure 4.2: Flowchart of the MATLAB program for reading and processing the PMT pulses from the event files of the FADC. Generally, each BEGe event is followed by the corresponding PMT waveform. These PMT events are read and the baseline for each of them is determined. Therewith, the program checks the veto condition and computes the PMT pulse's energy. This information is stored together with the event number, as an array in an output file.

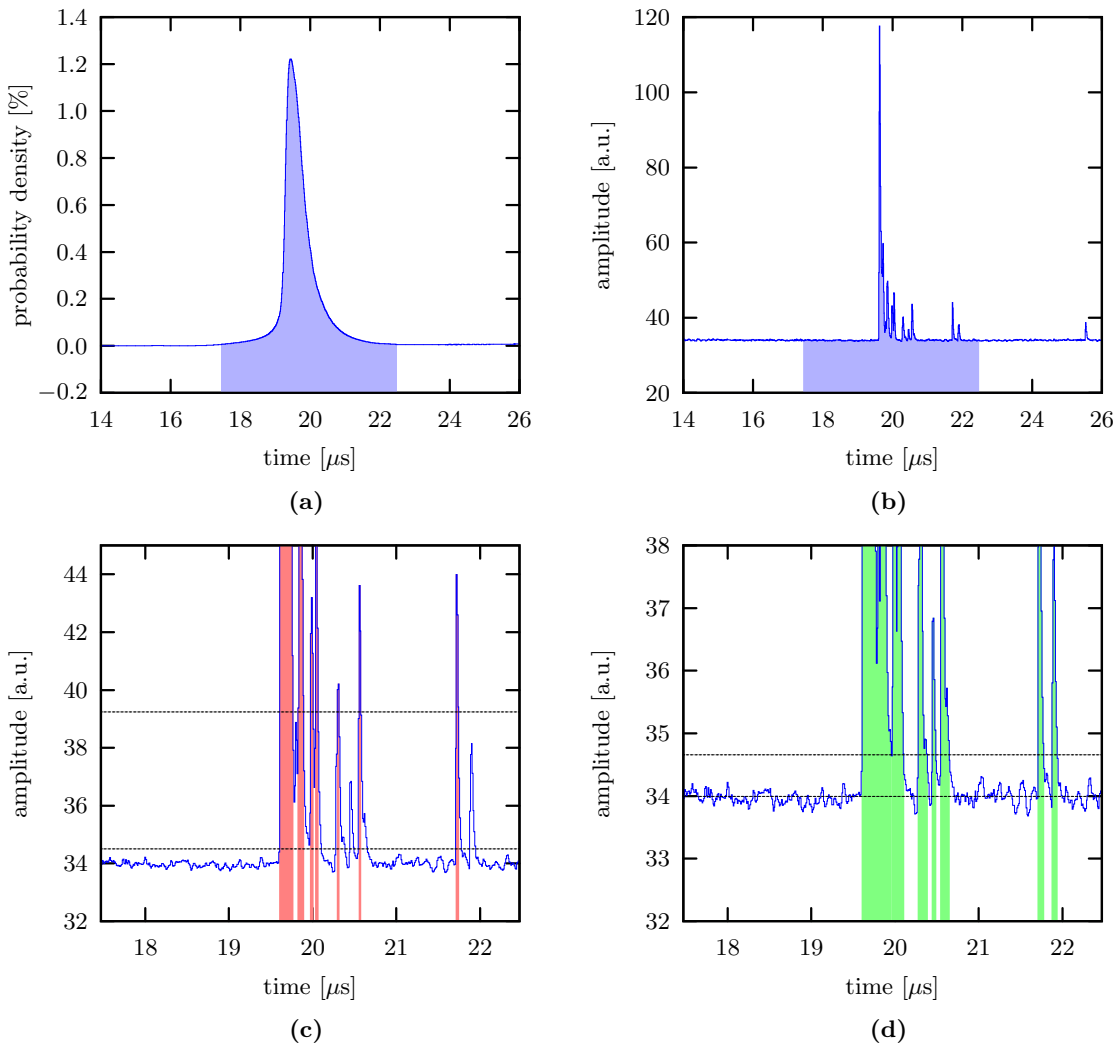

Figure 4.3: **(a)** The probability density profile of the PMT pulse from the internal ^{226}Ra run. The region in light blue shows the veto window with a width of 5 μs. **(b)** The PMT pulse of figure 4.1, with the veto window. **(c)** A close up of the veto window. The lower horizontal line indicates the baseline estimation after the third baseline iteration. The upper line is the corresponding 3σ limit, above which channels are excluded for the next iteration step. These channels are coloured red. **(d)** The horizontal lines show the final baseline after seven iterations, and the 5σ threshold. All channels which exceed the threshold cause a LAr veto. Here these channels are coloured green.

the pulse and then integrating it within the veto window. The veto threshold discriminates photo-electron signals from baseline noise. It is set to $5\sigma_i$ above b_i of the last iteration, typically corresponding to $\sim$20% of the signal amplitude of a single photo-electron. If any channel in the veto window exceeds the threshold, the LAr veto is triggered – figure 4.3d. Accordingly, a boolean is written to an output file, together with the event number and the energy of the PMT pulse. The 5σ veto threshold is derived in section 4.1.3.

4.1.2 Characteristic quantities of the veto efficiency

In this work, the quality of the LAr veto is evaluated by mainly two quantities: The *acceptance* and the *survival probability*. These depend on the type, location and activity of the investigated source, and must be determined for each source individually – the results of which are the topic of section 4.4. Alternatively to the survival probability, its reciprocal – the *suppression factor* (SF) – is commonly used as well. The veto cut parameters are optimized with respect to these characteristic quantities.

Acceptance

The acceptance (ε_{acc}) quantifies the probability for a BEGe event, to pass the veto cut without being vetoed 'by mistake'. Hence, one aspires an acceptance close to 100%, in order not to loose events due to false rejection.

False rejection is caused by *random coincidences* (RC). These are PMT events, which are independent from a BEGe event, but nonetheless coincide with the veto window and accidently trigger the veto. These RC events, which have an impact on the acceptance, can have several origins:

- Single photo electrons from the PMTs' dark noise.
- Background radiation, which does not hit the germanium detector. For example, the beta decay of ^{39}Ar.
- Radiation from an investigated source. To create a random coincidence, the BEGe and the PMT signal must come from independent decays, respectively decay chains.
- Electronic noise/artifacts. Often, these 'events' occur in both, the BEGe and the PMT pulse, and are filtered out during the pulse shape processing of BEGe, before the veto cut is applied. Therefore, electronic noise/artifacts is no issue for the veto.

All these events contribute to the total PMT trigger rate of the veto. The trigger rate ν_{trig}^{PMT} can be used to estimate the probability for a random coincidence p_{RC} in a given time window Δt. With Δt being the length of the veto window (here: $5\,\mu s$), p_{RC} is also related to the acceptance:

$$p_{RC} = 1 - \varepsilon_{acc} \approx \nu_{trig}^{PMT} \cdot \Delta t \tag{4.1}$$

The acceptance can be measured directly with a pulser signal, which is fed into the germanium detector's preamplifier. This makes sure, that the observed signal is independent from any PMT events, and no valid vetoing can occur. Now, the acceptance is given by the number of counts in the pulser peak before ($N_{0,pulser}$) and after ($N_{V,pulser}$) the veto cut:

$$\varepsilon_{acc} = \frac{N_{V,pulser}}{N_{0,pulser}} \tag{4.2}$$

The pulser peak is set to high energies beyond the 2615 keV line of ^{208}Tl, in order not to overlap with the gamma spectrum. Alternatively to the pulser, other spectral lines, which by their nature cannot be vetoed, can be utilized as well.

Survival probability

The *survival probability* (ε_{sur}) is the fraction of BEGe events in a given energy range, which is not vetoed. That said, the fraction of events vetoed due to random coincidences is excluded from this number. For the number of counts in a certain energy range N_0, the number of counts in the corresponding suppressed spectrum N_S is given by

$$N_S = \varepsilon_{sur} \cdot \varepsilon_{acc} \cdot N_0 \tag{4.3}$$

With the acceptance ε_{acc} determined from a pulser peak (equation 4.2), the survival probability ε_{sur} is uniquely defined by this equation. A survival probability of 100% corresponds to no suppression at all. The better the suppression, the smaller is ε_{sur}. The reciprocal of ε_{sur} is called *suppression factor* ($SF = 1/\varepsilon_{sur}$).

4.1.3 Determination of veto cut parameters

The two veto cut parameters are the *veto threshold* and the *veto window*, both of which have been introduced in section 4.1.1. In fact, the veto window is a matter of two parameters, the lower and upper bound of the window. However, later in this section we will downsize it to a single parameter.

For the optimization of the cut parameters we define an optimization criterium. On the one hand, the survival probability (ε_{sur}) for background should be as small as possible. Since the most important energy range for GERDA is the ROI of $Q_{\beta\beta}$, we choose this region for optimization; using an energy range of 2039±35 keV. On the other hand, the acceptance (ε_{acc}) should be close to 100%. Since these quantities characterize the quality of the LAr veto, and both depend on the cut parameters, it is reasonable to optimize the parameters by minimizing the ratio $\varepsilon_{sur}/\varepsilon_{acc}$; i.e. minimizing ε_{sur}, while simultaneously maximizing ε_{acc}.

The sources chosen for the optimization are internal ^{226}Ra and ^{228}Th (see section 4.4.1). The background runs do not yield enough statistics in the ROI. And the runs with external sources have a too high coincidence trigger rate, which results in a low acceptance. This is, because these sources were chosen to be more active than the inner sources. However,

Table 4.1: Shown are the trigger rates for BEGe and PMT events, subject to the source activity and position. For the acceptance two values are given for comparison: 'approx.' is the approximation using equation 4.1; 'pulser' is determined from the pulser.

source	position	activity [kBq]	ν_{trig}^{BEGe} [Hz]	ν_{trig}^{PMT} [kHz]	acceptance [%] approx.	pulser
no source			0.02	6.7	96.7	97.3
^{228}Th	external	38.9	5.5	43.3	78.4	78.3
	internal	0.63	45.9	8.6	95.7	95.7
^{226}Ra	external	94.9	7.1	39.2	80.4	78.7
	internal	0.934	66.9	8.1	96.0	94.2

the parameters are intended to be optimized primarily for the background case, where the event rate is small. The internal sources embody the best compromise. Table 4.1 gives an overview on the trigger rates with different sources, and an estimate of the acceptances with a veto window of 5 μs. Other sources are not considered, since their contribution to the RoI of $Q_{\beta\beta}$ is smaller.

Optimization of the veto threshold

In some events the baseline of the PMT pulses exhibits a slight curvature. Also, high frequency noise bunches may appear in the veto window. These have a frequency of the order of the single photo electron pulse length ($\sim$100 Mhz), and have an amplitude only a few times smaller. The occurence of the pickups (high frequency electromagnatic interferences) in these events is reflected in a higher baseline spread, compared to events where only normal noise appears. In order to have an individually optimized threshold for each event, the threshold is chosen to be a multiple of the baseline spread, rather than a fixed value.

A scan of ε_{sur} and ε_{acc} as a function of the threshold cut is shown in figure 4.4. The survival probability (green) quickly rises, until the threshold is well above the noise level at around 5σ baseline spread. At higher thresholds the survival probability rises gradually, as more and more photo electrons are lost. The acceptance (blue) behaves similarly, only that it almost saturates, once a threshold above the noise level is reached. The ratio $\varepsilon_{sur}/\varepsilon_{acc}$ (red), which is the optimization parameter to be minimized, has its minimum also around 5σ. Thus, we set the veto threshold to this value. For events which don't suffer strong pickups, this threshold corresponds to $\sim$20% of the signal amplitude of a single photo electron.

The scan was performed on data from the internal ^{226}Ra measurement. At a crosscheck with internal ^{228}Th no significant differences were found for the position of the minimum.

Optimization of the veto window

For the choice of the veto window we consider the probability density profile (pdp) of the PMT pulses – see figure 4.3a. It is obtained by subtracting the baseline from the average pulse, and normalizing the integral to unity. Starting from the highest probability density at the peak, we integrate the pulse towards equally lower values on both sides, until a certain coverage (a fraction of the normalized pdp area) is reached. These intervals are uniquely defined by the coverage, and can be taken as possible veto windows. Thus, we have reduced the two free parameters of the veto window – namely the lower and upper bound – to the single parameter *pdp coverage*. What remains, is only to optimize $\varepsilon_{sur}/\varepsilon_{acc}$ with respect to this parameter.

Figure 4.5 shows $\varepsilon_{sur}/\varepsilon_{acc}$ as a function of the pdp coverage for each of the two sources. The total aquired statistics after the veto cut is much smaller in the internal ^{228}Th run, than in ^{226}Ra. This is because the veto efficiency for ^{228}Th is much better in the RoI, and only few counts survive the cut. In fact, the steps in the graph stem from each new event in the RoI, which is captured with increasing veto window size. One graph in each figure is created with ε_{sur} and ε_{acc} from the respective source runs (magenta), whereas in the second graph the acceptance is replaced by one from a measurement without source (blue). The

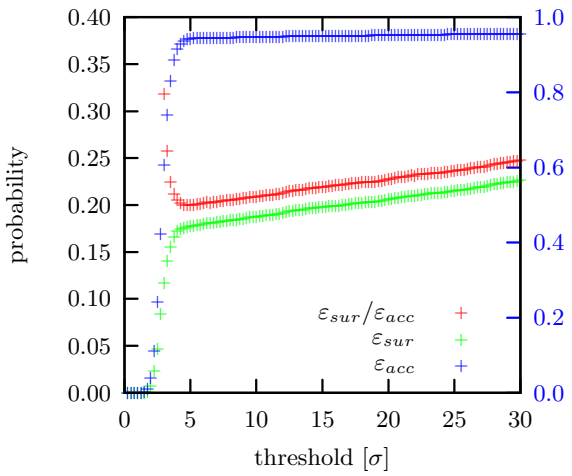

Figure 4.4: A scan of the survival probability ε_{sur} in the RoI of $Q_{\beta\beta}$, the acceptance ε_{acc}, and $\varepsilon_{sur}/\varepsilon_{acc}$ as a function of the veto threshold from an internal ^{226}Ra measurement. The optimization parameter $\varepsilon_{sur}/\varepsilon_{acc}$ (red) exhibits a minimum at 5σ. The blue y-scale on the right side holds for ε_{acc}.

latter is for comparison. The idea behind this is to do the optimization as close as possible to the background case. It turns out that the graphs for both sources and acceptances have rather extended regions of minimal $\varepsilon_{sur}/\varepsilon_{acc}$, all of which happen to overlap between 93% and 94%. The choice was made for a veto window of 5 μs, which corresponds to 93.6% pdp coverage.

The choice of the veto cut parameters, *veto window* and *veto threshold*, is setup dependent. On the one hand, the light yield determines the energy threshold of the veto. Therewith, a higher light yield would allow to decrease the size of the veto window, since the probability to still find light in the remaining window is increased. Also, with a better light yield one could afford a multiplicity veto trigger, and therewith significantly decrease the random coincidence rate. The random coincidence rate by itself is also strongly setup dependent: The main influences are the dark noise of the PMTs, and the background countrate in the liquid argon volume.

4.2 Pulse shape processing of BEGe

Two of the most beneficial features of BEGe-type detectors for GERDA, as compared to the standard coaxial HPGe-detector type, are a superior energy resolution and pulse shape discrimination. For an optimized energy resolution it is worthwhile to conduct an elaborated offline pulse shape processing on the digital waveforms recorded with the FADC. Its implementation in LArGe was developed and carried out by Matteo Agostini [68, 69]. It is briefly summarized in the first part of this section. The second part describes the technical principle behind the PSD, and its realization in LArGe. The presented PSD method was largely developed by Dušan Budjáš [46, 70], and applied by him to the measurements of this work.

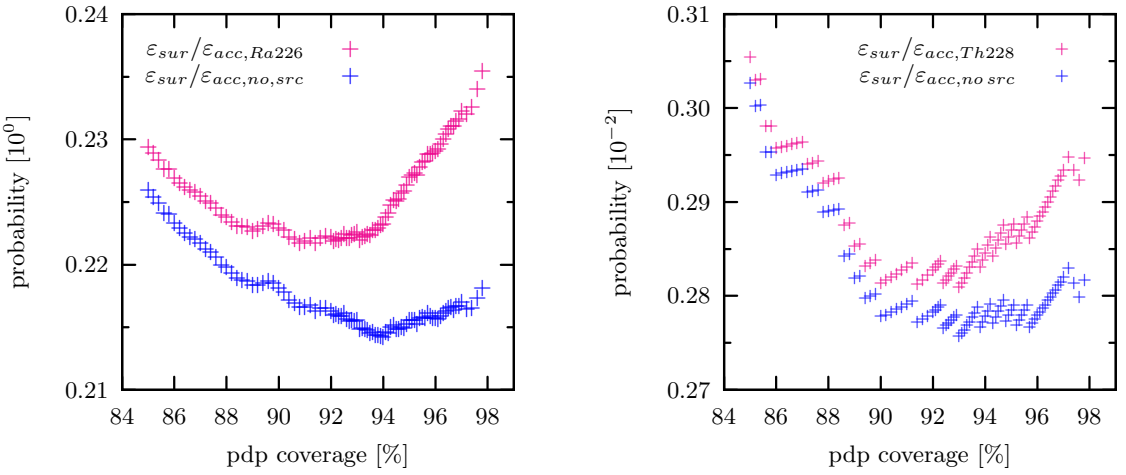

(a) internal ^{226}Ra **(b)** internal ^{228}Th

Figure 4.5: A scan of the optimization parameter $\varepsilon_{sur}/\varepsilon_{acc}$ as a function of the *pdp coverage*. The acceptance is taken once from the respective source measurement (magenta), and second from the measurement without a source (blue).

4.2.1 Energy reconstruction

The energy reconstruction from the digital BEGe pulses involves several aspects: The primary objective is to reconstruct the energy (E) of the events with high accuracy. In order to increase the signal-to-noise ratio, the waveform undergoes several steps of processing and shaping. However, this is hampered by perturbances like baseline oscillation, high frequency electromagnetic interferences (pickups), and overlapping waveforms from consecutive events (pileups) – just to name a few. Deficient events must be either corrected or removed, because their energy reconstruction is inaccurate and would impair the resolution. Eventually, the signal amplitude (A) of the pulses must be determined, in order to provide the A/E parameter for the pulse shape discrimination.

The waveforms of the charge-sensitive preamplifier are characterized by an initial rising edge, generated by the charge collection from the germanium crystal. It is followed by an exponentially decaying tail, whose time constant $\tau = RC$ is given by the preamplifier's RC feedback capacitor – see figure 4.1a as an example for an undisturbed pulse.

The initial step of pulse processing is the *baseline restoration* (or *pileup correction*). An exponential fit of the baseline is conducted on the first part of the waveform before the leading edge. The fitting function is then subtracted from the entire pulse, in order to correct for a residual decay tail of a previous event. If the waveform can be corrected properly, it is used for further processing. Otherwise, the event must be removed. Figure 4.6a shows such a pileup event.

For the extraction of the energy the *Moving Window Deconvolution* (MWD) approach [71], developed by Stein et al., is utilized. This approach allows perfect trapezoidal/triangular shaping by applying only a MWD, and an integration filter. The MWD consists of a deconvolution of the exponentially decaying tail of the signal, a subsequent differentiation to avoid computation overflows, and an integration. The basic motivation is to be able to

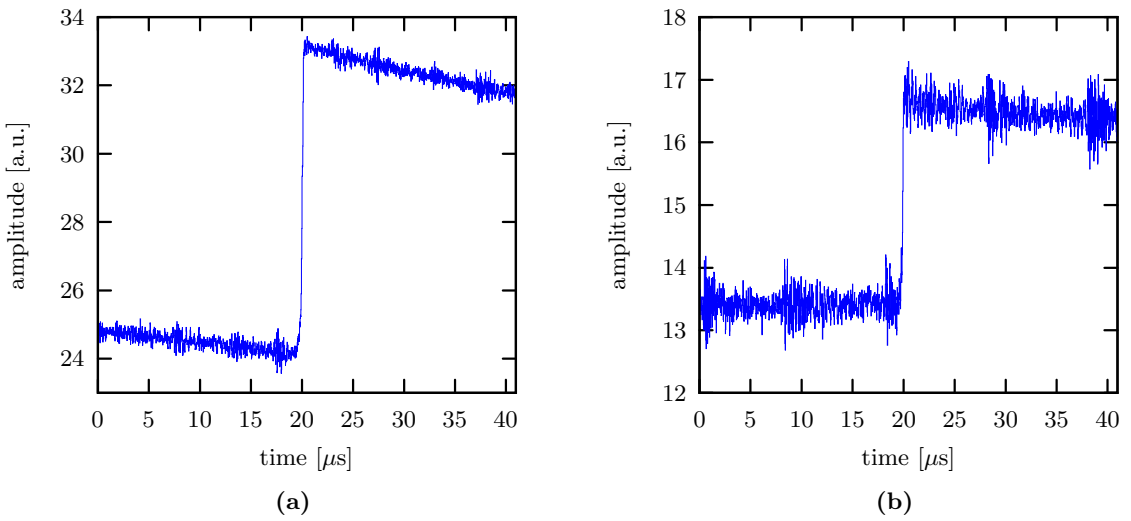

Figure 4.6: Digital BEGe pulses recorded with the FADC. **(a)** A *pileup* event, sitting on top of the exponential tail of the forerunner. **(b)** An event corresponding to an energy deposition of 96 keV. It contains noise bunches due to *pickups* in intervals of 10 μs.

average the decaying part by making it flat. In combination with an additional integration filter (*moving average*), this allows to significantly reduce the noise. This is particularly important for events with pickups, which are commonly observed in the LArGe setup – e.g. see Figure 4.6b. The outcome of the filtering is a trapezoidal shaped pulse, whose amplitude corresponds to the charge, respectively the energy, of the event. A more detailed discussion of this shaping method applied to BEGe pulses can be found in [68, 69].

The amplitude A is defined as the amplitude of the current pulse. It is computed deconvolving the initial charge pulse with an exponential function, and applying a differentiation filter. Hence, A/E is determined.

Eventually, a number of cuts are applied, in order to remove signals generated by non-physical events (DAQ problems), or signals with strange shapes, which cannot be analysed properly. All in all, only a few percent ($\sim$1%) of the recorded signals are removed (for most of the data sets).

4.2.2 Pulse shape discrimination method

The pulse shape discrimination (PSD) method with BEGe detectors has been developed in the light of the anticipated $0\nu\beta\beta$ events of ^{76}Ge in GERDA. The signature in the Ge-detector is an energy deposition of $Q_{\beta\beta}$ by the two beta particles. The path length of the electrons is of the order of one millimetre. These localized events are called *single site events* (SSE). In contrast, most of the background events in that energy region are multiple-Compton-scattered gamma-rays, likely to interact at various locations in the Ge-crystal: *multi site events* (MSE). Even though the transition from SSE to MSE is smooth, it is the objective of the PSD to discriminate these cases, and provide a cut for the rejection of MSE. The reliability and validation of the PSD method has been studied thoroughly, and is described in detail in [46, 70].

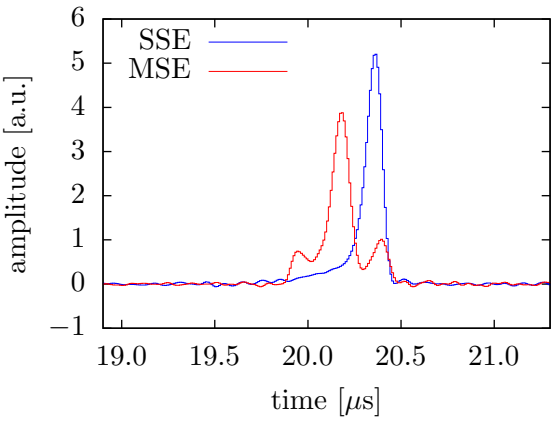

Figure 4.7: The current pulses of a SSE (blue) and MSE (red) with the same energy E. The amplitude A is proportional to the energy of the largest interaction point. Since for a SSE the energy is concetrated in one interaction point, A is proportional to E. For a MSE A/E is smaller.

PSD principle

The basic concept of PSD is the investigation of time structure (shape) in the recorded BEGe signals. At each interaction point, a cluster of charge carriers builds up and moves along the electrical field lines towards the electrodes. While SSE consist of only one charge cluster, MSE generate multiple clusters, which arrive at different times.

In order to improve the spatial resolution, it is worthwhile to have a slow charge collection. In BEGe detectors, this is achieved by a small read out electrode, causing a large variation of the electrical field in the diode. The charge collection time in BEGe is of the order of $\sim$1 μs, compared to a few $\sim$ 100 ns in a standard coaxial detector. Close to the small $p+$ contact, the weighting field sharply increases, so that the current pulse is peaking sharply with its amplitude A proportional to the charge in the cluster. As the final part of the trajectories close to the signal contact is (practically) independent of the initial location of the energy position, the ratio A/E is constant for a given energy E in the cluster. Hence, for a SSE the amplitude is proportional to the total energy E of that event. In contrast, the amplitude of a MSE corresponds to the highest energy deposition in only one of the interaction points, leading to a smaller A/E ration – see example pulses in figure 4.7. This different behaviour of A/E for SSE and MSE is utilized to perform the SSE/MSE cut. The current amplitude resolution was tested to be typically about 0.5%.

As a welcome side effect of the small electrode, the capacitance of the detector becomes very small, and hence reduces the serial component of the electronic noise. This is not only beneficial for the PSD, but it also improves the energy resolution and lowers the energy threshold of the detector.

PSD calibration spectrum

The PSD cut is calibrated with the internal ^{228}Th measurement, because this common source provides both SSE and MSE. Figure 4.8 shows the energy spectrum of the internal

^{228}Th source in a wide region around $Q_{\beta\beta}$, and a corresponding density plot of the A/E parameter.

The line at 2615 keV is the full energy absorption peak (FEP) of ^{208}Tl, a progeny of ^{228}Th. That line's double escape peak (DEP) at 1593 keV is used as a substitue for the $\beta\beta$-decay, as it mostly consists of SSE: The 2615 keV gamma-ray has a significant probability for e^+e^- pair production, which can result in a localized energy deposition in the detector. The annihilation of the positron is accompanied by back-to-back emission of two 511 keV photons. A DEP event occurs, when both annihilation photons escape the detector without further interaction. Out of these events, only a small fraction of 4-9% are MSE, caused by hard bremsstrahlung of the electron or positron – the rest are SSE. Events, where only one of the annihilation photons escapes, form the single escape peak (SEP) at 2104 keV, dominated by MSE. The SEP and the FEP can be used as representative samples of MSE.

All three peaks (FEP, SEP, DEP) are visible in the spectrum (figure 4.8). In the A/E distribution, the FEP and the SEP appear as vertical lines with a wide distribution of A/E values. In contrast, the DEP is highly concentrated in one point at $A/E \approx 7.66$.

Another source of SSE is found in Compton continuum below the 2615 keV peak: The narrow band around $A/E \approx 7.66$ is almost constant in energy. Hence, since the amplitude A is directly proportional to the energy E, it can be interpreted as SSE – called the *SSE line*. The band consists of events from single Compton scattering (SCS). The broader region below the SSE line ($A/E < 7.66$) is the *MSE region*, which contains multiple Compton scattering (MCS) events.

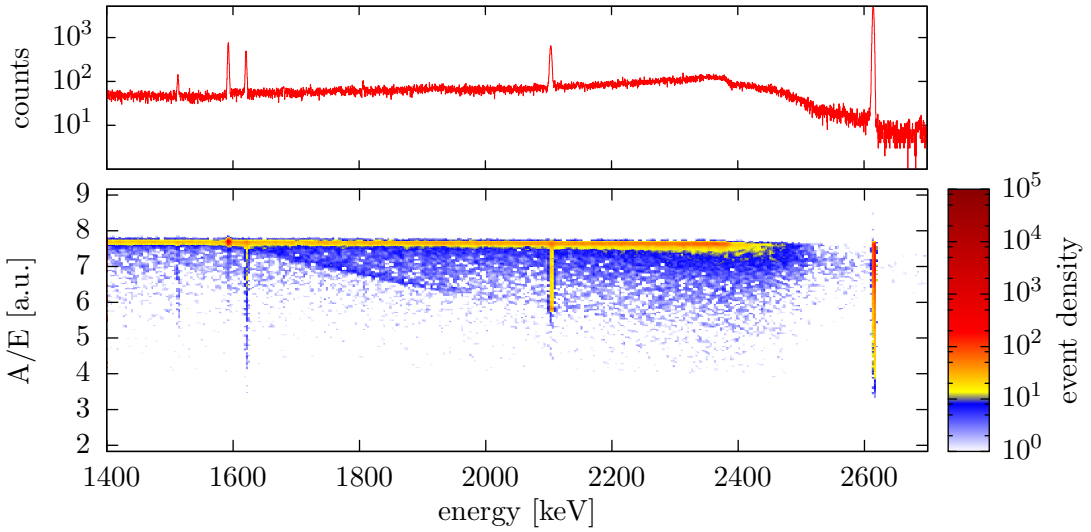

Figure 4.8: Top: The internal ^{228}Th spectrum in a broad energy region around $Q_{\beta\beta}$. **Bottom:** The density plot of the A/E parameter of the same measurement, as a function of the energy E. The colour bar on the right indicates the number of events in a square of 3.25 keV×0.0367 a.u. in logarithmic scale. The *SSE line* is the dense horizontal line around $A/E \approx 7.66$; below lies the *MSE region*. Both are explained in the text. The DEP at 1593 keV appears as a high density point on the SSE line.

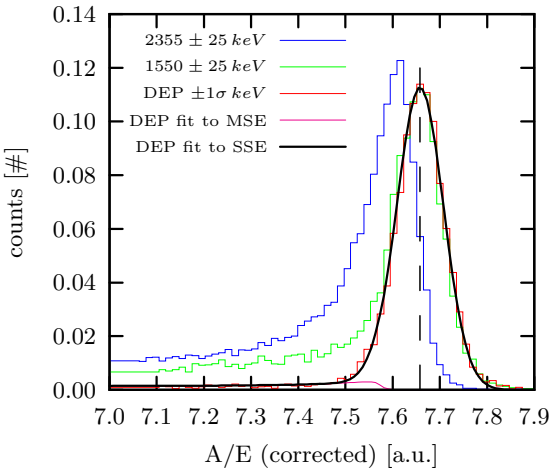

Figure 4.9: The histograms are cross-sections from the A/E distribution of the SSE band of the internal ^{228}Th calibration measurement. The fit with a Gaussian and an exponential tail is shown for the cross-section of the DEP. The vertical dashed line indicates the mean value m of the gaussian, which represents the A/E value of the SSE line at the particular energy. The mean value is shifted when looking at other energy regions.

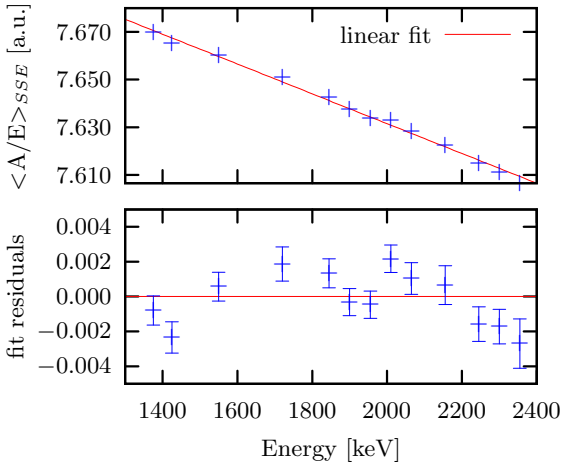

Figure 4.10: Top: The mean values m of the Gaussian fits to the cross-sections in the Compton region of the SSE band. The linear fit extrapolates the energy dependence of the SSE line and provides the slope parameter a to the cut function. **Bottom:** The fit residuals. The error bars include the statistical uncertainty of the A/E histogram fits.

PSD cut function

It is evident, that the SSE line in the A/E density distribution is not constant in energy, but rather can be approximated by a linear dependence. Therefore, the PSD cut function (CF) must contain a function of energy, reproducing the SSE line. Moreover, the offset must be chosen at A/E values slightly below the center of the SSE line, to discriminate single site events from the lower MSE region. Events with $A/E < CF$ are rejected as MSE:

$$CF(E) = a \cdot E + b_{DEP} \tag{4.4}$$

The slope a is determined from several cross-section cut-outs of the SSE band between 1.35 and 2.4 keV: Here, the A/E histogram follows a gaussian distribution for the SSE, since the resolution of A is dominated by noise in the current signal. The MSE contribution is approximated by an exponential tail (figure 4.9). A least-square-fit of each cross-section determines the mean value m of that gaussian, respectively of the SSE band. A linear fit to the various m's of each cross-section eventually determines the slope a (figure 4.10).

The efficiency of the PSD cut is tuned by the offset b_{DEP} of the cut function. For this work, b_{DEP} is chosen to fix the acceptance for events in the DEP to 90%, which corresponds to an A/E value of 7.53 in the DEP cross-section. In this aspect the PSD calibration differs from the method given in the references [46, 70] and follows the argument of [69].

PSD survival probability

The *survival probability* (respectively the *suppression factor*) of the PSD follows the definition given for the LAr veto in section 4.1.2: It is the fraction of events surviving the PSD cut in a given energy range. However, in contrast to the LAr veto, the survival probability is not corrected for the acceptance ($\varepsilon_{acc} = 1$ in equation 4.3). Since the acceptance of the PSD is independent of source strength and position, the survival probabilities remain comparable among the various measurements.

The dominant uncertainties of the PSD calibration with ^{228}Th are the fitting uncertainties of the A/E histograms. The absence of a reference SSE sample in most other sources (like a DEP) does not allow to calibrate these measurements individually. Therefore, the PSD calibration from ^{228}Th must be used for other data sets as well – with the downside, that electronic instabilities of the DAQ must be taken into account. The systematic error of the survival probability due to these instabilities is estimated by varying the offset of the cut function, according to the magnitude of the SSE-line fluctuation during a measurement.

4.3 Spectroscopic performance of BEGe

After the insertion of BEGe into the LArGe cryostat, the spectroscopic performance was tested with a multichannel analyzer (MCA) using an external ^{60}Co source. Later this measurement was repeated, when the electronic scheme with the FADC was installed. It turned out, that the 'FADC-setup' is much more sensitive to electronic noise and electromagnetic interferences (pick-ups) than the far simpler MCA setup. The implemented countermeasures include (a) the installation of a RC-filter for HV (Caen), (b) thorough grounding of the main LArGe hardware components (lock, cryostat, shielding, cryogenic system), and the entire electronic chain, and (c) the electronic decoupling of the whole setup from the metal laboratory walls and selected components of the slow control during measurements. All in all, the BEGe baseline spread was reduced to a level of 1-2 mV, with minor pick-ups of 100 kHz remaining. These are dealt with offline in the pulse shape processing phase (section 4.2.1).

In LArGe the BEGe detector is operated at bias voltage +4000 V, as derived in [49]. During the three months lasting measurement campaign the leakage current remained at a stable level below 10 pA.

In the 'MCA-setup' the CC2 preamplifier [48] is followed by a spectroscopy amplifier (Ortec Mod.672; set to 10 μs shaping time), which feeds the signal to the MCA (Ortec Mod.927). The spectra were recorded using the Maestro-32 software (by Ortec). A pulser signal (Ortec Mod.448) is fed into the preamplifier test input. The spectrum recorded in this configuration is shown in figure 4.11a (the decay scheme of ^{60}Co is discussed below in section 4.4.4). For the 1332 keV peak of ^{60}Co the resolution is 1.99 keV full width at half maximum (FWHM). The pulser yields 1.60 keV FWHM at 1.6 MeV.

The resolution in the spectrum taken with the FADC is worse (figure 4.11b): The 1332 keV peak has a FWHM of 2.27 keV, and the pulser at 1.6 MeV has 2.02 keV FWHM. The resolution specified by the manufacturer is 1.8 keV FWHM for the 1332 keV peak, measured in a vacuum cryostat. Given, that the diode is operated 'naked' in LAr, and that noise

is still present on the unprocessed detector pulses, the result is quite satisfactory [47]. A spectral resolution at this level does not compromise the study of suppression efficiencies. Therefore, further improvement of the noise was set aside.

Long term spectral stability

The suppression efficiency measurements of this chapter were recorded in FADC-data sets of approximately one day aquisition time each. The calibration of the energy spectra is done for each data set individually, using the dominant spectral lines of the respective sources. During a two-months period in the course of the measurement campaign the peak positions are found to be shifted by 0.3%–0.4%. Since the daily gain fluctuation is much smaller,

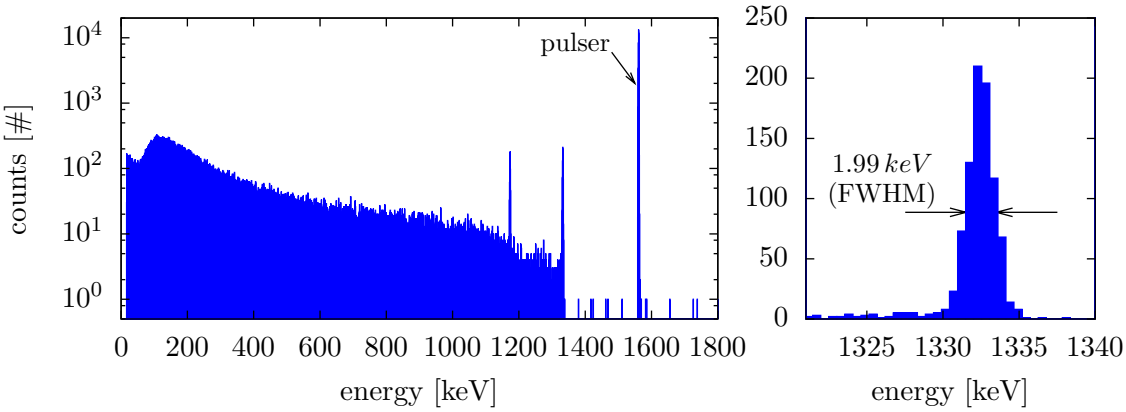

(a) The BEGe spectrum of ^{60}Co taken with a MCA.

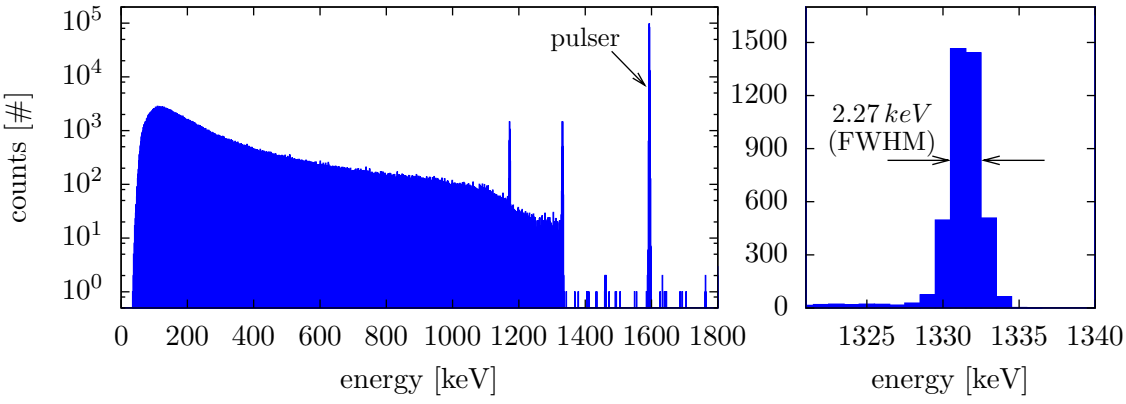

(b) The BEGe spectrum of ^{60}Co taken with a FADC.

Figure 4.11: **(a)** directly after inserting the detector into the LArGe cryostat. The spectral resolution of the 1332 keV peak is 1.99 keV FWHM. The pulser has 1.60 keV FWHM at 1.6 MeV. **(b)** in the final electronic scheme. The spectral resolution is 2.27 keV FWHM for the 1332 keV peak, and 2.02 keV FWHM for the pulser (at 1.6 MeV).

and the spectra are calibrated for each run individually, no deterioration of the spectral resolution is observed.

4.4 Suppression efficiency for different gamma sources

With the BEGe detector, several energy spectra were taken for various sources in different positions. The suppression efficiency and the acceptance of the LAr veto and the PSD were determined for characteristic energy regions, to verify and characterize the mechanism of both cut techniques individually, and in combination. It can be demonstrated, that LAr veto and PSD complement each other: As such, their combined suppression factor in the RoI of the $0\nu\beta\beta$-decay is better than the product of the individual suppression (*orthogonality*). The results show the potential for the achievable background rejection with a possible implementation of the cut techniques in GERDA.

4.4.1 Properties of the sources

The properties of the utilized sources are listed in table 4.2. All sources, except for ^{137}Cs, were measured in two locations, as illustrated in figure 4.12: The 'external' sources were placed between the outer wall of the cryostat and the copper shielding, approximately at the height of the center of the BEGe detector ($\pm$5 cm). The 'internal' (or 'inner') sources were placed as close to the BEGe diode as possible. These are wire sources, which are led down to the side of the detector through a designated source-flange mounting system (section 2.1.5) with a vertical and horizontal position error of about $\pm$3 cm each.

The sources are meant to simulate background contributions from different parts of the setup. The external sources simulate background from the shielding or the cryostat walls. The internal sources represent background from the inner detector assembly, such as from the preamplifier, the detector or its holder. The activity of the sources was chosen as a compromise between a high countrate in the BEGe detector on the one hand, and a low event rate in the LAr on the other hand, to reduce random coincidences.

Single and coincident gammas

For the discussion of the response of the LAr veto to different gamma sources it is helpful to classify the gammas in the following way: Multiple gammas, which are emitted in a cascade from a nuclear decay within a short time span, are referred to as *coincident* or *cascading* gammas. The lifetime of the intermediate nuclear states must be short enough for one gamma to be detected in the Ge-diode, and for the other to evoke a LAr signal within the corresponding veto window. In our case, this time span is about half the width of the veto window, i.e. $\sim$2.5 μs. An example for coincident gammas is the decay of ^{208}Tl to ^{208}Pb, from the ^{228}Th decay chain: The decay scheme in figure 4.24 shows, that the prominent 583 keV gamma (relative intensity 84.5%) is directly followed by the 3- state at 2615 keV, which itself decays to the ground state with a halflife of 16.7 ps. Therefore, these two gammas are emitted consecutively and with a time constant of pico-seconds, short enough to fulfil the coincidence condition. In fact, this holds true also for all other gammas of that decay, since none of the intermediate states is a long-lived isomeric state. The impact of cascading

Table 4.2: A list of the sources utilized in the suppression measurements of this chapter. The uncertainty of the activities is typically about 3%, except for ^{228}Th external (15%).

source	position	nominal activity [kBq]	reference date	half life [y]	measurement start date (year 2010)	current activity [kBq]
^{137}Cs	external	42.2	01/02/2002	30.07	01/06	34.9
^{60}Co	external	413	13/02/1990	5.27	04/05	28.8
	internal	0.641	28/01/2005	5.27	02/07	0.314
^{226}Ra	external	95.2	01/06/2002	1600	21/05	94.9
	internal	0.936	01/12/2004	1600	17/06	0.934
^{228}Th	external	100	01/09/2007	1.91	07/05	38.9
	internal	3.06	01/02/2006	1.91	15/06	0.63

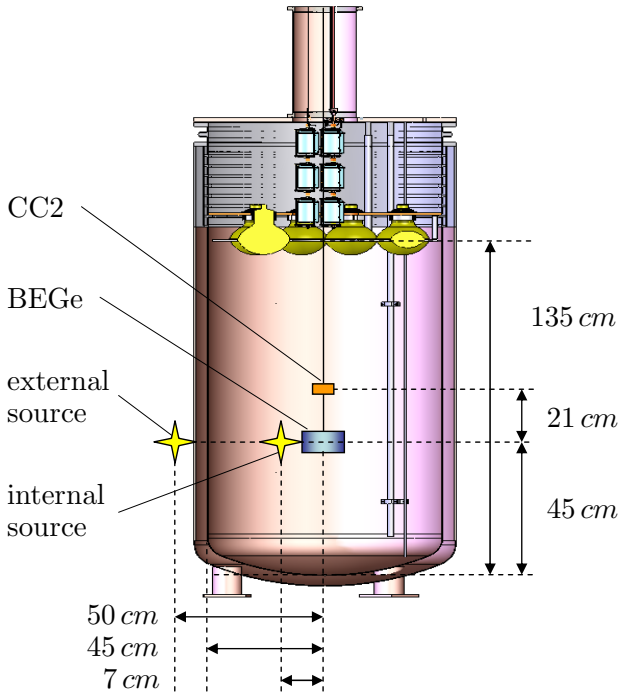

Figure 4.12: A schematic view of the source positions 'external' and 'internal', and the BEGe detector in the LArGe setup. The position error is estimated to be ±3 cm for inner sources, and ±5 cm for external sources.

Table 4.3: The trigger rates of the BEGe detector ν_{trig}^{BEGe} and the PMTs ν_{trig}^{PMT}, and the acceptance ε_{acc} of the LAr veto, are shown for the different source measurements. The acceptance is determined from a pulser or a characteristic peak in the spectrum, following the definition given in section 4.1.2.

source	position	activity [kBq]	aquisition time [d]	ν_{trig}^{BEGe} [Hz]	ν_{trig}^{PMT} [kHz]	acceptance ε_{acc} [%]
^{137}Cs	ext	34.89	1.59	2.1	25.4	87.3
^{60}Co	ext	28.81	1.31	5.4	58.9	69.2
	int	0.314	13.06	26.9	5.8	96.6
^{226}Ra	ext	94.9	2.49	6.9	39.2	78.7
	int	0.934	1.54	65.4	8.1	94.2
^{228}Th	ext	38.9	8.30	4.5	43.3	78.3
	int	0.63	1.96	47.5	8.6	95.7

gammas on the suppression efficiency is strongly dependent on their solid angle towards the active LAr-volume: While gamma-rays from internal sources inevitably traverse the LAr, the solid angle for external gammas to miss the cryostat is larger than 2π.

A gamma quantum without a coinciding partner is referred to as being *single*. For instance, this is the case for the 662 keV line of ^{137}Cs (decay scheme in figure 4.13). So, in contrast to coincident gammas, a single gamma which is fully absorbed in the Ge-detector has no chance to trigger the LAr veto – except for random coincidences. Therefore, single-type gamma lines are intrinsically unsuppressed, and can be used to determine the veto's acceptance – just as with a pulser.

The distinction of single and coincident gammas is less significant for the Compton continuum: Regardless of its origin, a gamma which Compton-scatters into or out of the Ge-detector has a high chance of depositing part of its energy in the LAr. If the deposited energy exceeds the energy threshold of the veto, the gamma is rejected. The maximum available energy for the veto is given by the difference of the energy in the Compton spectrum, and the initial energy of the gamma-ray ('excess energy'). The suppression efficiency in Compton regions therefore depends on the energy difference to the causative gamma line.

4.4.2 Overview on measurements

Table 4.3 provides an overview on basic parameters of the suppression measurements: It shows the interrelation of the sources' activities (and positions) with the trigger rates of the BEGe detector and the PMTs, and the acceptance ε_{acc} of the LAr veto. The acceptance is determined from a pulser signal or a characteristic peak.

General notes on data taking

The FADC data is recorded in chunks of approximately one day aquisition time. The electronic scheme of the DAQ is presented in section 2.6.1. During data taking lab activities are

reduced to a minimum, to prevent the generation of electromagnetic noise or microphonics. For example, for refilling the LN-dewars of the active cooling, or pumping the insulation vacuum of the cryostat, the measurements are interrupted.

Due to the malfunction of some PMTs, only five PMTs are included in the DAQ. While four of these PMTs are running on nominal voltage, the fifth PMT repeatedly discharged and tripped, and its HV had to be risen up again (section 2.4.4). Therefore, a part of the measurements was conducted with the fifth PMT only partially working. The discharges and the power-up seem not to impede the measurements else than by a change of the detected scintillation yield.

Evaluation procedure

The steps taken for the data evaluation are as follows:

1. The LAr veto cut routine is applied on the raw data files. The output file contains a boolean tag with the veto information for each event (4.1).

2. Pulse shape processing is executed on the raw data files. It provides E and A/E for the events und filters out 'bad events' (4.2.1). The output file is merged with the file from step 1.

3. Energy spectra are created from the output files. The energy calibration is performed, and spectra that belong to the same source measurement are summed up.

4. The PSD cut is applied. First, it is calibrated on the inner ^{228}Th measurement. Then, it is applied to the other source measurements (4.2.2). The energy spectra of each source now contain four different histograms; one for each 'cut combination': 1) unsuppressed, 2) with the LAr veto cut applied, 3) with PSD, and 4) with LAr veto & PSD.

5. The survival probabilities for different energy regions and cut combinations is determined from the energy spectra. The LAr veto acceptance is determined from the pulser peak (see below).

All of these steps were coordinated and performed in close cooperation with Matteo Agostini and Dušan Budjáš.

Calculation of survival probabilities

The calculation of the survival probability ε_{sur} for a given cut combination in the region of interest (RoI) of the $0\nu\beta\beta$-decay is straightforward, following the definitions given in section 4.1.2 and 4.2.2: The number of counts in the RoI of the suppressed spectrum N_S is divided by the number of counts in the unsuppressed spectrum N_0. When the LAr veto is part of the cut ('cut combinations' 2 and 4), the result is divided by ε_{acc}. The statistical uncertainty is derived from N_S, N_0 and the corresponding quantities of ε_{acc}, using poisson counting statistics. In addition, the PSD cut involves a systematic uncertainty. The uncertainty

quoted in the final results (tables below) is the total uncertainty, including statistical and systematic errors.

To determine the suppression factor for single spectral lines, N_0 and N_S refer to the net peak area above background. The RoI of the particular line is choosen to have a width of 3.8 FWHM of the full energy peak. Two equally sized areas, adjacent to the left and right side of the RoI, are used to fit a model of the Compton background under the peak: a Heaviside step-function convoluted with a gaussian, to emulate the detector resolution. Eventually, the net peak area is the number of counts in the RoI, minus the estimated Compton background.

The subtraction of natural background from the source spectra is not relevant for the determination of the suppression efficiencies in LArGe, and is omitted in this analysis. The measured BEGe rates are much higher than the rates of corresponding regions in the natural background spectrum. For illustration, the background rate in the RoI at $Q_{\beta\beta}$ (2039±35 keV) is 3.4 cts·d^{-1}, whereas the rates for the external sources ^{226}Ra and ^{228}Th are 460 cts·d^{-1} and 1730 cts·d^{-1}, respectively. The rates for internal sources are even higher.

4.4.3 ^{137}Cs external source

The purpose of the ^{137}Cs measurement is to test the functional principle of the LAr veto with a simple isotope: As the decay scheme in figure 4.13 shows, ^{137}Cs makes a β^-–decay to ^{137}Ba, which possesses only a single gamma line at 662 keV, with a branching ratio of 94.4%. The full energy peak of the *single* gamma is expected to be vetoed only by random coincidences, just like the pulser signal. Thus, the two 'lines' should yield the same reduction factor, both providing the *acceptance* of the LAr veto. In contrast, the Compton continuum must be suppressed genuinely.

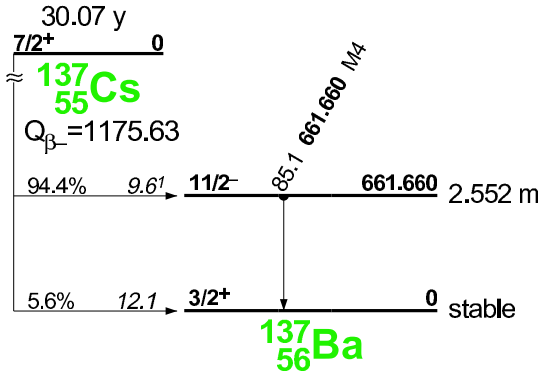

Figure 4.13: The decay scheme of ^{137}Cs [72].

The achieved suppression of ^{137}Cs with the PSD cut is not optimal, because the PSD is not calibrated for energies below 1400 keV. For this reason, the PSD is not discussed for this measurement. Nonetheless, it is shown in the spectra for completeness.

Figure 4.14 shows the energy spectrum of ^{137}Cs in logarithmic scale, and a close–up of the 662 keV peak and the pulser. The pulser position was set at 3 MeV, well above the caesium spectrum. A comparison of figure 4.14b and 4.14c shows, that both peaks are only little

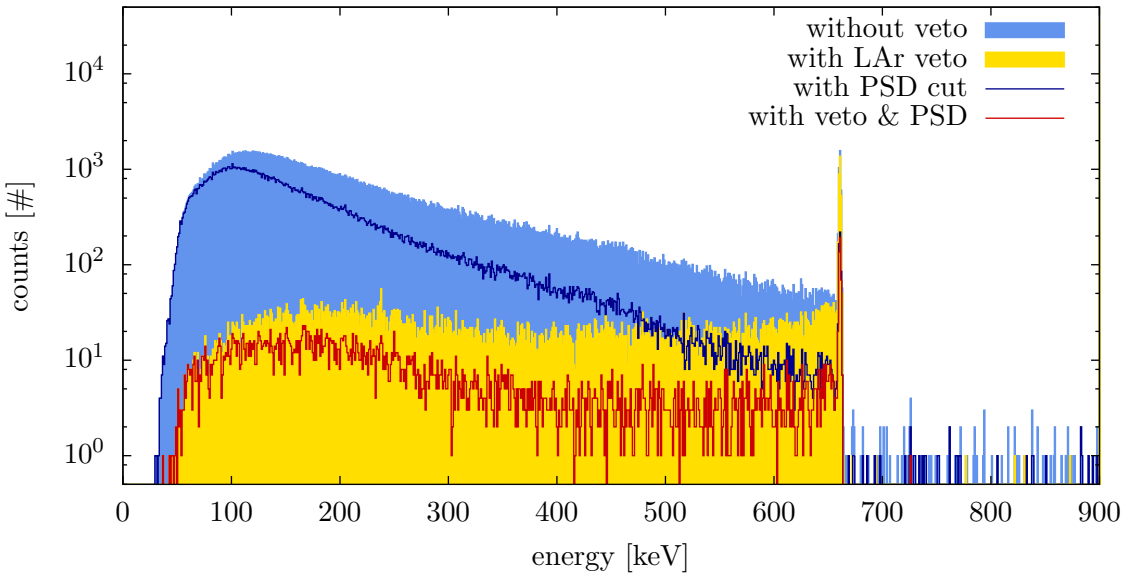

(a) Full spectrum with 662 keV peak and the Compton region.

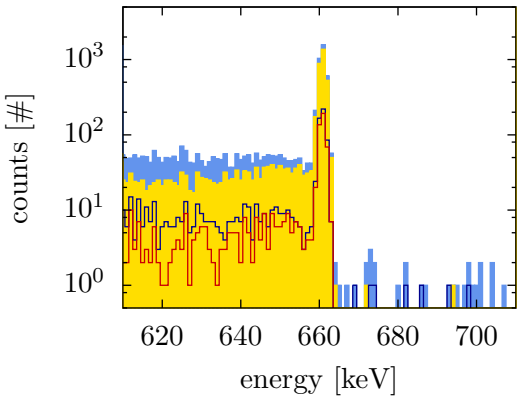

(b) Close-up of the 662 keV peak.

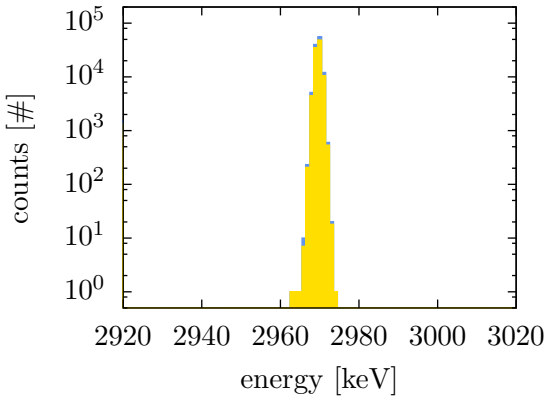

(c) Close-up of the pulser peak.

Figure 4.14: Energy spectrum of ^{137}Cs. The single gamma line at 662 keV is unaffected by the LAr veto, whereas the Compton region is suppressed. The suppression of the pulser and the gamma line is both exclusively due to random coincidences, and thus provide the veto's *acceptance*. The PSD cut is not optimized for this energy region.

suppressed by the LAr veto; in fact, the suppression is hardly noticeable at this scale. The acceptance calculated from the pulser is (87.3±0.4)%, calculated from the single gamma line it is (86.9±2.3)%. These two values agree within their uncertainty, and hence confirm our expectation that the gamma line is suppressed by random coincidences only. Accordingly, the *survival probability* (which is by definition corrected for the pulser acceptance!) of the gamma line is (99.5±2.7)%. A survival probability of 100% means 'no suppression at all'.

In contrast to the single gamma line, the Compton continuum is clearly suppressed by the LAr veto. The suppression is energy dependent and reaches one order of magnitude around 400 keV, close to the Compton edge at ∼470 keV. The suppression is decreasing towards the full energy peak, as a smaller energy fraction of the 662 keV-gamma ('excess energy') is available to trigger the veto. The veto is bypassed, if this excess energy is either deposited outside the LAr, e.g. by Compton scattering in the shielding or the detector holder, or too few scintillation light is created to reach the energy threshold of the veto. The cutoff at the low energy side of the spectrum is due to the energy threshold of the Ge-detector.

4.4.4 ^{60}Co external & internal source

The isotope ^{60}Co is expected to be one of the major background contributions to GERDA [33]). It is cosmogenically produced in germanium and copper, leading to an intrinsic trace impurity of the detectors and their holders. At each decay ^{60}Co emits two gammas of 1173 keV and 1332 keV – see the decay scheme in 4.15. Since the energy of each gamma is below the ROI of the $0\nu\beta\beta$-decay (2039 keV), only their summation may create a critical background event. The summation is possible because the time constant of the cascade (0.7 ps) is much shorter than the time resolution of the BEGe detector (∼1 μs). The spectrum expands up to the summation peak at 2505 keV. The strong solid-angle dependence of summation events confines the origin of this background to material close to the diodes, respectively the diodes themselves. The internal ^{60}Co measurement emulates this situation in LArGe.

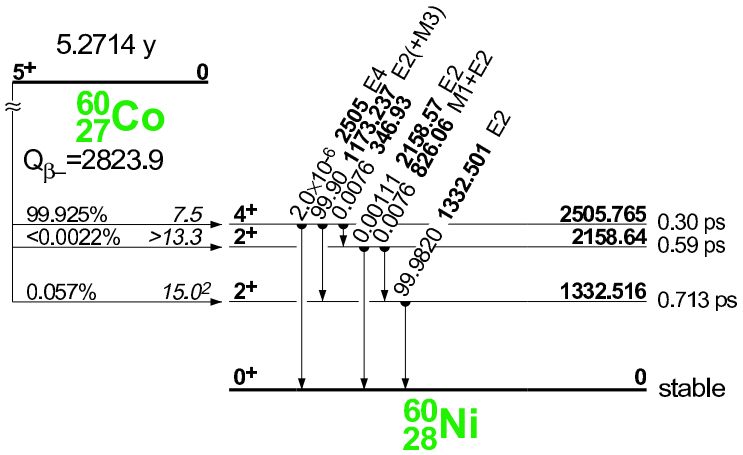

Figure 4.15: The decay scheme of ^{60}Co [72].

The full spectrum is shown in figure 4.17, with close-ups of the relevant peaks (4.18) and the ROI of $Q_{\beta\beta}$ (4.19). For comparison, a measurement with an external ^{60}Co source was

carried out (spectrum in figure 4.16). A compilation of the survival probabilities is given in table 4.4.

Evidently, the two full energy peaks of the internal spectrum are strongly suppressed by the LAr veto, with survival probabilities of 3.43% (1173 keV) and 2.95% (1332 keV). While one gamma is detected in the BEGe diode, the other one is likely to be simultaneously scattered in the LAr, by which it is surrounded. In combination with the suppression from the PSD cut (12.2% for each peak), the lines are reduced to less than 0.5% of the unsuppressed spectrum.

The situation is different for the external source: Here the survival probabilities of the LAr veto are 75.3% (1173 keV) and 76.9% (1332 keV). Since the source is positioned outside of the cryostat, and the gammas are *cascading*, the suppression efficiency is strongly diminished. This is, even if one gamma has succeeded to make a full energy deposition in the Ge-diode, its companion from the decay is still likely not to hit the LAr at all – hence, not to trigger the veto. Conversely, the PSD is independent of the source position: The peaks are suppressed to ∼11%, and agree with the corresponding suppression for the internal source within 1σ uncertainty. Again it must be stated, that the PSD is not optimized for energies below 1400 keV, and that the achieved suppression with these lines might be improvable.

While the inner-source measurement exhibits a distinctive summation spectrum, it is too weak to be investigated in the external spectrum. The following discussion is therefore restricted to the internal source:

In contrast to the full energy peaks, the summation peak of the inner source is practically unsuppressed by the LAr veto; it is merely affected by random coincidences. This is expected, since no gamma energy is deposited outside the Ge-diode to trigger the veto. Therewith, the acceptance of the LAr veto can be determined from the summation peak, yielding 96.5%, without using a pulser. As a consequence, the survival probability (being corrected for random coincidences) of the summation peak is equal to *one*, equivalent to the 662 keV peak of ^{137}Cs. The PSD acts more effectively on the summation peak (survival probability 0.194%), than on the single gamma peaks. The reason is, that the summa-

Table 4.4: The *survival probabilities* in different regions of the internal and external ^{60}Co spectrum. The numbers are given for the LAr veto and PSD separately, as well as for their combination (column 'total'). The peaks marked with * are used to determine the *acceptance* of the LAr veto. The survival probabilities in the columns 'LAr veto' and 'total' are corrected for the acceptance (see section 4.4.2).

position	region	energy [keV]	survival probability [%]		
			LAr veto	PSD	total
internal	peak	1173	3.43 ± 0.07	12.17 ± 0.58	0.423 ± 0.023
	peak	1333	2.95 ± 0.06	12.21 ± 0.54	0.357 ± 0.018
	RoI	$2004 - 2074$	3.67 ± 0.23	1.31 ± 0.15	0.026 ± 0.020
	sum peak*	2505	96.6 ± 1.9	0.194 ± 0.064	n.a.
external	peak	1173	75.3 ± 2.4	11.27 ± 0.79	7.80 ± 0.72
	peak	1333	76.9 ± 2.1	10.42 ± 0.78	8.15 ± 0.69
	pulser*	1590	69.18 ± 0.23		

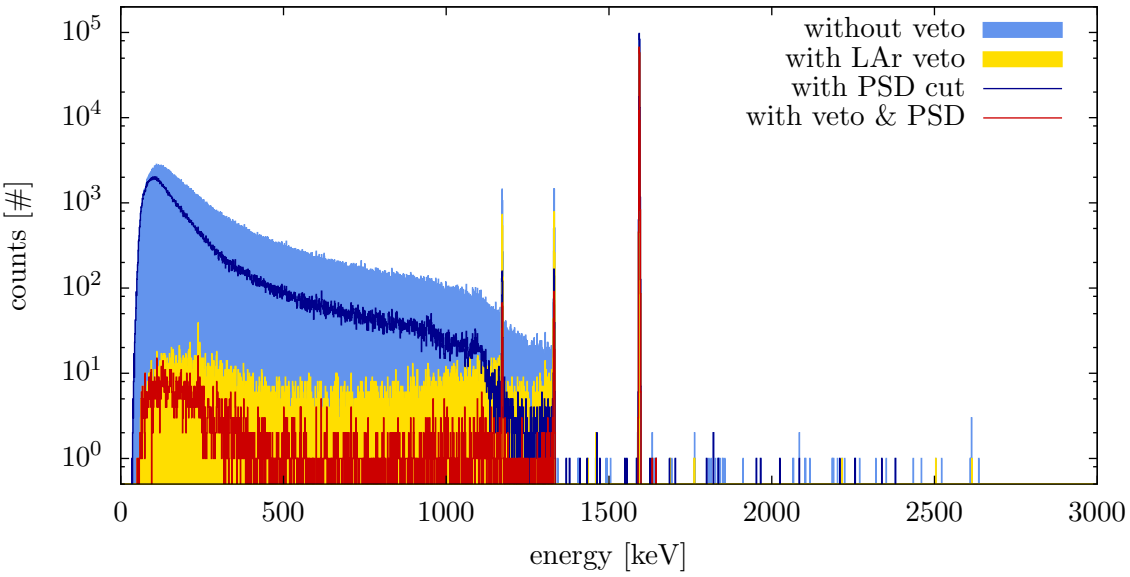

Figure 4.16: The external ^{60}Co spectrum. The distance from the source to the detector (0.5 m) is too large to produce a summation spectrum in the RoI of $Q_{\beta\beta}$. Therefore, external ^{60}Co is no concern for the background in GERDA. The pulser is positioned at 1.6 MeV.

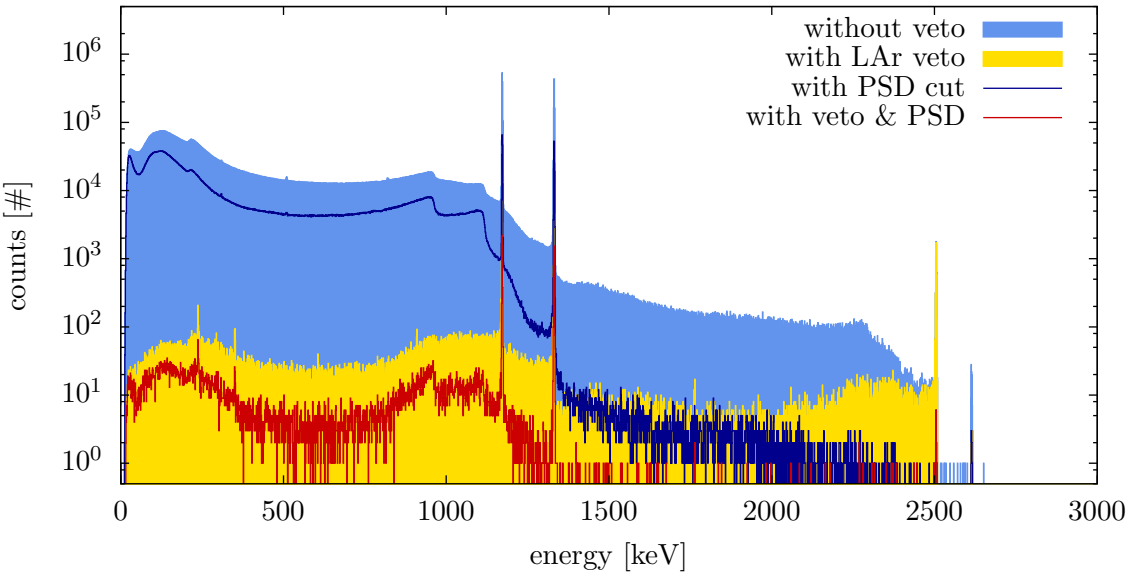

Figure 4.17: The internal ^{60}Co spectrum. Due to the proximity of the source to the detector, a summation spectrum is present above the 1332 keV line, covering the RoI of the $0\nu\beta\beta$-decay. The summation peak is visible at 2505 keV. Cosmogenic ^{60}Co is considered a limiting background for the GERDA experiment.

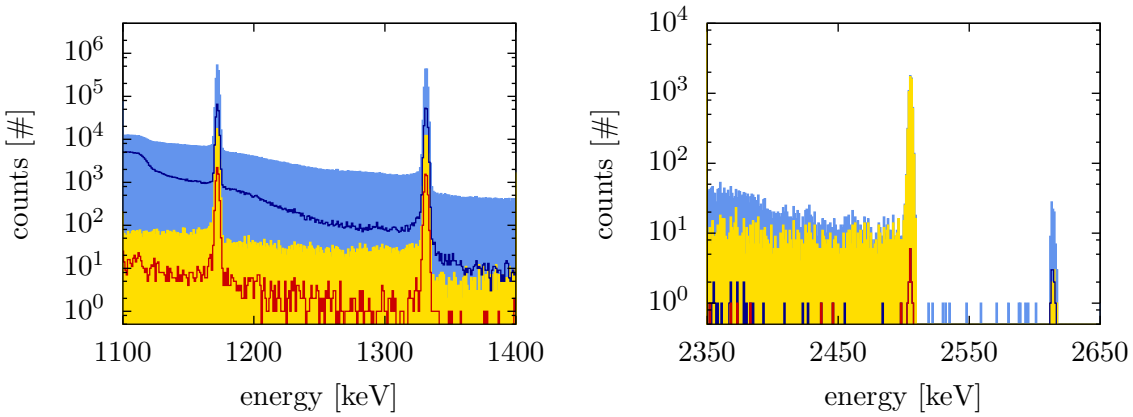

(a) The peaks at 1173 keV and 1332 keV.

(b) The summation peak at 2505 keV.

Figure 4.18: **(a)** The full energy peaks are suppressed by both cut techniques. **(b)** On the other hand, the LAr veto has no effect on the summation peak at all, whereas the PSD works even more effective. The small peak at 2615 keV is a background peak from ^{208}Tl.

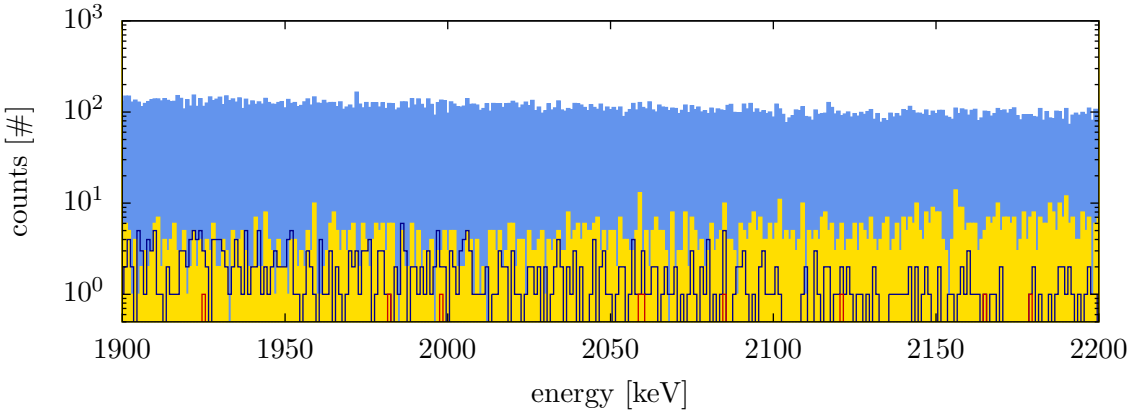

Figure 4.19: The RoI of the $0\nu\beta\beta$-decay around 2039 keV. Both cuts individually reduce the ^{60}Co induced 'background' to a few percent. The combination of the techniques is survived by merely 4 counts in a 70 keV wide region around $Q_{\beta\beta}$ (red contour line), which corresponds to a survival probability of 0.026% (suppression factor ∼3900). The relative uncertainty of the total suppression is 71%.

tion peak inherently consists of multi-site events (MSE) by detecting multiple gammas. It makes no sense to provide a number for the combination of the LAr veto and PSD, since the survival probability of the LAr veto is equal to *one*.

Eventually, most relevant for GERDA, is the suppression of ^{60}Co induced background in the ROI at $Q_{\beta\beta}$: The events in this part of the spectrum dispense part of their energy to their proximity, preferentially to the LAr. And by the nature of summation events, they are almost exclusively MSE (see the close-up in figure 4.19). Therewith, both suppression methods have an ideal grip to veto these events. In a 70 keV wide region around $Q_{\beta\beta}$, the LAr veto achieves a survival probability of 3.67%, and the PSD 1.31%. The total reduction is to 0.026% of the initial 'background' level, which corresponds to a suppression factor of ∼3900. The relative uncertainty is 71%, because only 4 counts survive both cuts. A much wider region than 70 keV to increase the number of surviving events was not chosen, because the spectra exhibit unlinear behaviour of the background before and after the cuts. Altogether, in this setup the combination of the cut techniques allows to suppress the critical background by more than three orders of magnitude.

4.4.5 ^{226}Ra external & internal source

^{226}Ra is a long lived progeny of ^{238}U in the natural decay chain; a simplified version of which can be found in the appendix B, together with the decay schemes of the relevant isotopes ^{214}Pb and ^{214}Bi; the latter of which dominates the gamma background at $Q_{\beta\beta}$. ^{226}Ra decays to ^{222}Rn, which is a radioactive noble gas that diffuses into the LAr of the GERDA (and LArGe) cryostat. ^{222}Rn and impurities of ^{238}U are potentially a major background source to GERDA. Since the impurities are distributed in the LAr volume, both, the external and the internal ^{226}Ra measurements are relevant for an assessment of the suppression capability of the LAr veto for an implementation in GERDA.

The full external and internal source spectra are shown in figure 4.20 and 4.21. The unsuppressed spectra comprehend lines from the ^{214}Bi decay. In the internal spectrum also lines from the ^{214}Pb decay are present (e.g. 352 keV, 295 keV). The pulser is set at 3 MeV. The gamma spectrum of the ^{214}Bi decay contains several *single* gamma lines above 1.7 MeV (e.g. 1764 keV, 2204 keV, 2448 keV), which decay directly to the ground state of ^{214}Po, and are not affected by the LAr veto. Other lines, such as 609 keV or 1120 keV, are emitted in a *cascade*. Hence, they are vetoed efficiently to a survival probability of a few percent for the internal source (see table 4.5 for details), but only down to 80 % for the external source. The PSD works coherently with a suppression of ∼10%, regardless of the source position. Detailed numbers for selected peaks are listed in table 4.5.

The suppression in the ROI at $Q_{\beta\beta}$ (2004–2074 keV) is in the range of 21–31% for the LAr veto and the PSD. The LAr veto's survival probability for external and internal radium differs by merely a factor 1.5. Because of the predominantly *single* nature of the gamma lines which cause the Compton background in the ROI, the detection of scintillation light relies on the excess energy of the scattered gammas. On the one hand, this makes the suppression less dependent on the distance from source to detector, as if *coincident* gammas were involved. On the other hand, the available energy to trigger the LAr veto is low: For example, the most intense gamma line above $Q_{\beta\beta}$ (2204 keV, branching ratio 4.86%) leaves 130–200 keV for the light detection; this corresponds to an average of 6–10 photo electrons

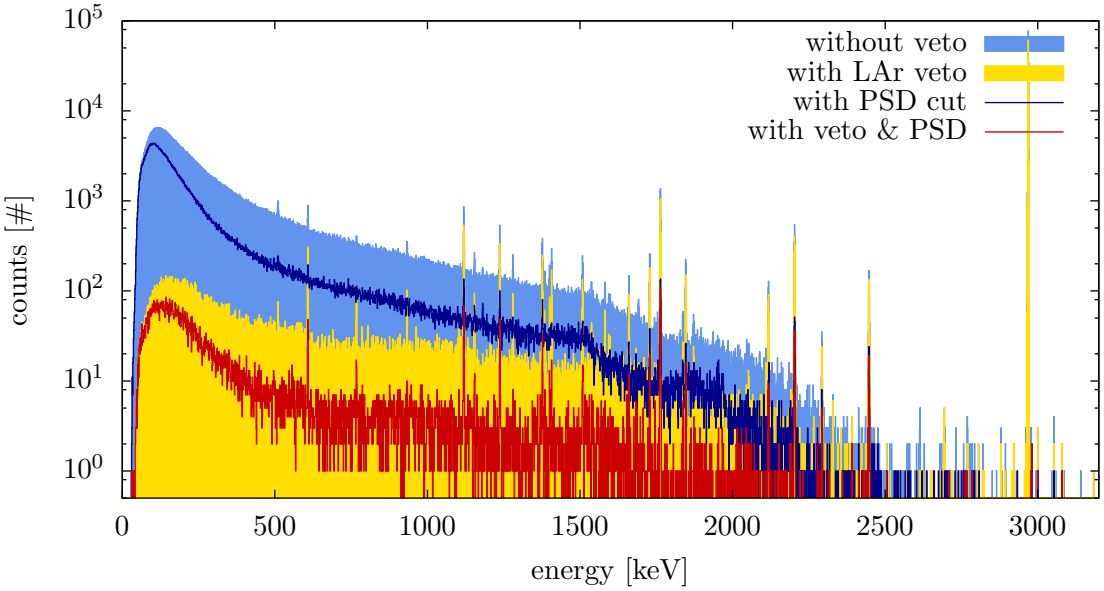

Figure 4.20: The external ^{226}Ra spectrum. The low energy lines of ^{214}Pb are shielded. Only energetically higher lines from the ^{214}Bi decay are visible. Since these are *single* gamma lines, they are not vetoed by the LAr veto. The pulser was set to 3 MeV and yields a LAr veto acceptance of 79%.

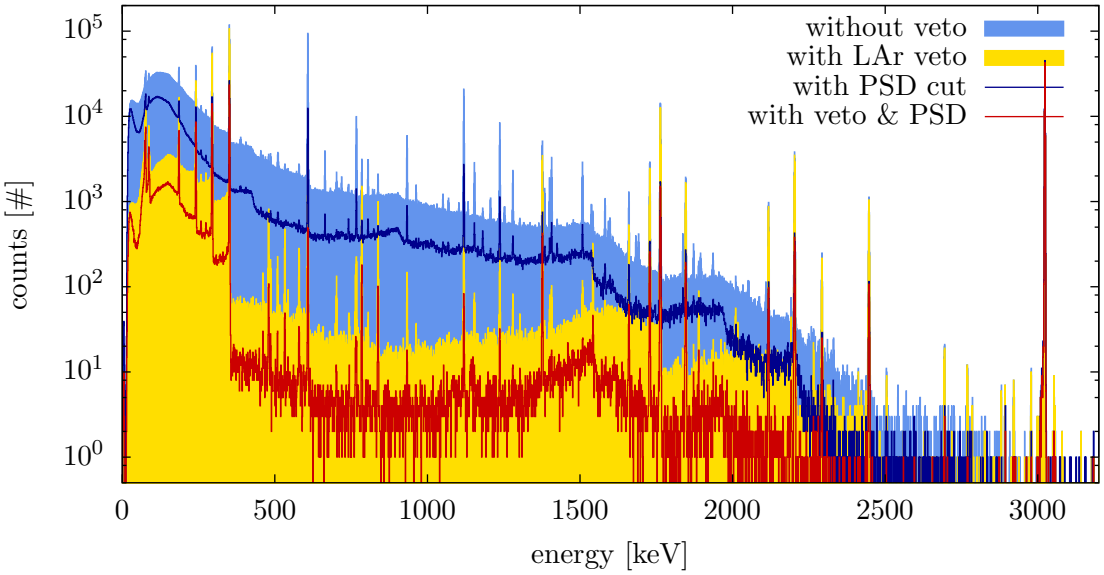

Figure 4.21: The internal ^{226}Ra spectrum. All major ^{214}Pb and ^{214}Bi lines are visible in the unsuppressed spectrum. Above the 2448 keV peak, also many faint lines appear. While the *cascading* gamma lines of the ^{214}Bi decay are effectively vetoed by LAr scintillation (e.g. 609 keV, 1120 keV), the *single* gamma lines, which decay directly to the ground state of ^{214}Po, are not (e.g. 1764 keV, 2204 keV, 2448 keV). The pulser was put at 3 MeV and yields an acceptance of 94% for the LAr veto.

Table 4.5: The *survival probabilities* for selected peaks and the RoI around $Q_{\beta\beta}$ (2039 keV) for the internal and external ^{226}Ra spectrum. The column 'total' contains the combined survival probabilitiy of the LAr veto and the PSD. The pulser peaks are used to determine the *acceptance* of the LAr veto, for which the survival probabilities of the columns 'LAr veto' and 'total' are corrected for (see section 4.4.2).

position	region	energy [keV]	survival probability [%] LAr veto	PSD	total
internal	peak	609	4.344 ± 0.053	12.73 ± 0.78	0.545 ± 0.038
	peak	1120	2.937 ± 0.089	11.84 ± 0.64	0.374 ± 0.040
	peak	1764	95.06 ± 0.81	11.76 ± 0.62	11.19 ± 0.59
	peak	2204	98.31 ± 1.44	10.61 ± 0.73	10.65 ± 0.69
	peak	2448	98.70 ± 2.56	10.49 ± 0.80	10.25 ± 0.79
	RoI	$2004 - 2074$	21.60 ± 0.72	24.67 ± 1.17	2.23 ± 0.26
	pulser	3020	94.20 ± 0.41 (LAr-veto acceptance)		
external	peak	609	81.8 ± 8.6	14.0 ± 4.9	12.1 ± 2.0
	peak	1120	93.4 ± 4.6	13.2 ± 1.9	11.5 ± 1.2
	peak	1764	100.5 ± 2.6	9.61 ± 0.74	10.50 ± 0.79
	peak	2204	98.7 ± 3.9	10.4 ± 1.0	9.8 ± 1.0
	peak	2448	96.1 ± 6.7	12.7 ± 2.1	12.0 ± 2.0
	RoI	$2004 - 2074$	31.4 ± 2.1	22.8 ± 1.9	5.56 ± 0.86
	pulser	2960	78.73 ± 0.28 (LAr-veto acceptance)		

at a light yield of 0.05 pe/keV. In this sense, the moderate suppression of ∼20% may point to an energy threshold effect of the LAr veto. If so, the suppression can be improved by a better photo-electron yield. Nonetheless, the total suppression of PSD and LAr veto combines to a survival probability of 2.2% (internal) and 5.6% (external).

The close-ups of the RoI show the 2118 keV peak of the ^{214}Bi decay in the unsuppressed spectra (figures 4.22 and 4.23). The peaks at 2011 keV and 2017 keV appear only in the internal spectrum after applying the LAr cut. None of these *single* gamma peaks is affected by the veto.

4.4.6 ^{228}Th external & internal source

^{228}Th and its progenies from the natural decay chain are universally abundant in the detector and construction materials of GERDA. Relevant background contributions to the experiment are expected mainly from internal parts (preamplifier electronics, detector holders etc.), and to a lower degree from external sources (e.g. the watertank) [33]. In particular critical is the isotope ^{208}Tl (decay scheme in figure 4.24): Its gamma line at 2615 keV (branching ratio 99%) expands well above the RoI at 2039 keV and dominates the gamma background in this region. But since the gamma is emitted in coincidence with other lines, the LAr veto is expected to suppress the line and its Compton spectrum effectively for inner

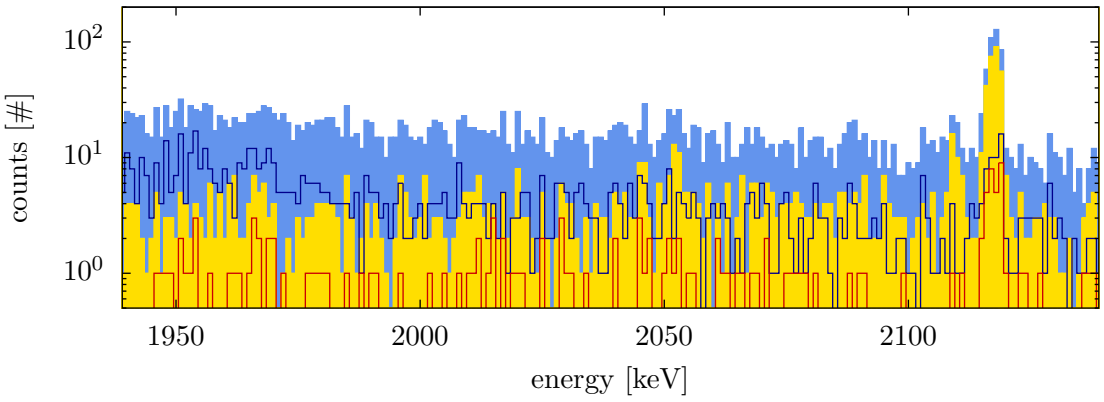

Figure 4.22: A close-up of the RoI at $Q_{\beta\beta}$ of the external ^{226}Ra spectrum. The *single* gamma peak at 2118 keV from the ^{214}Bi decay is visible. The survival probabilities for events in the energy window 2004–2074 keV around $Q_{\beta\beta}$ are 31% (LAr veto), 23% (PSD), and 5.6% (total).

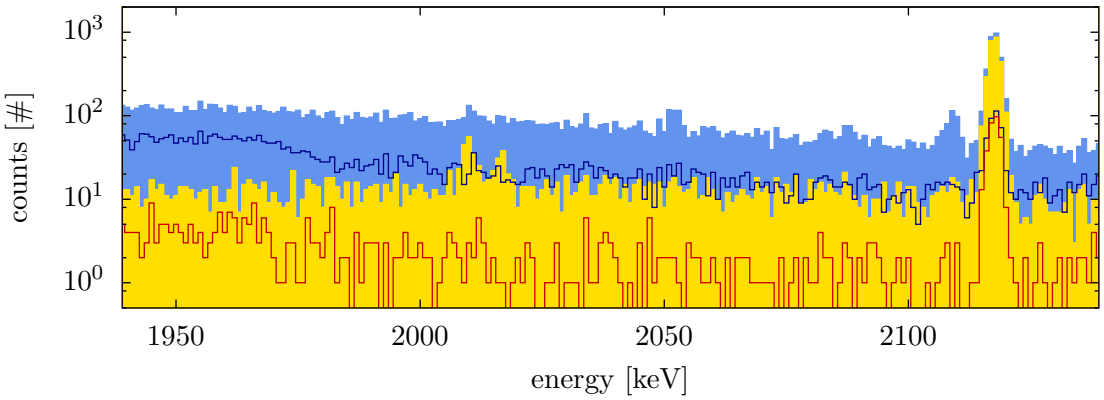

Figure 4.23: The RoI at $Q_{\beta\beta}$ of the internal ^{226}Ra spectrum. The 2118 keV peak of ^{214}Bi is visible in the unsuppressed spectrum, whereas peaks at 2011 keV and 2017 keV become distinct only after applying the LAr cut. Since all of these peaks stem from *single* gammas they are not affected by the LAr veto. In the energy window 2004–2074 keV around $Q_{\beta\beta}$ the survival probabilities are 22% (LAr veto), 25% (PSD), and 2.2% for the combination.

sources.

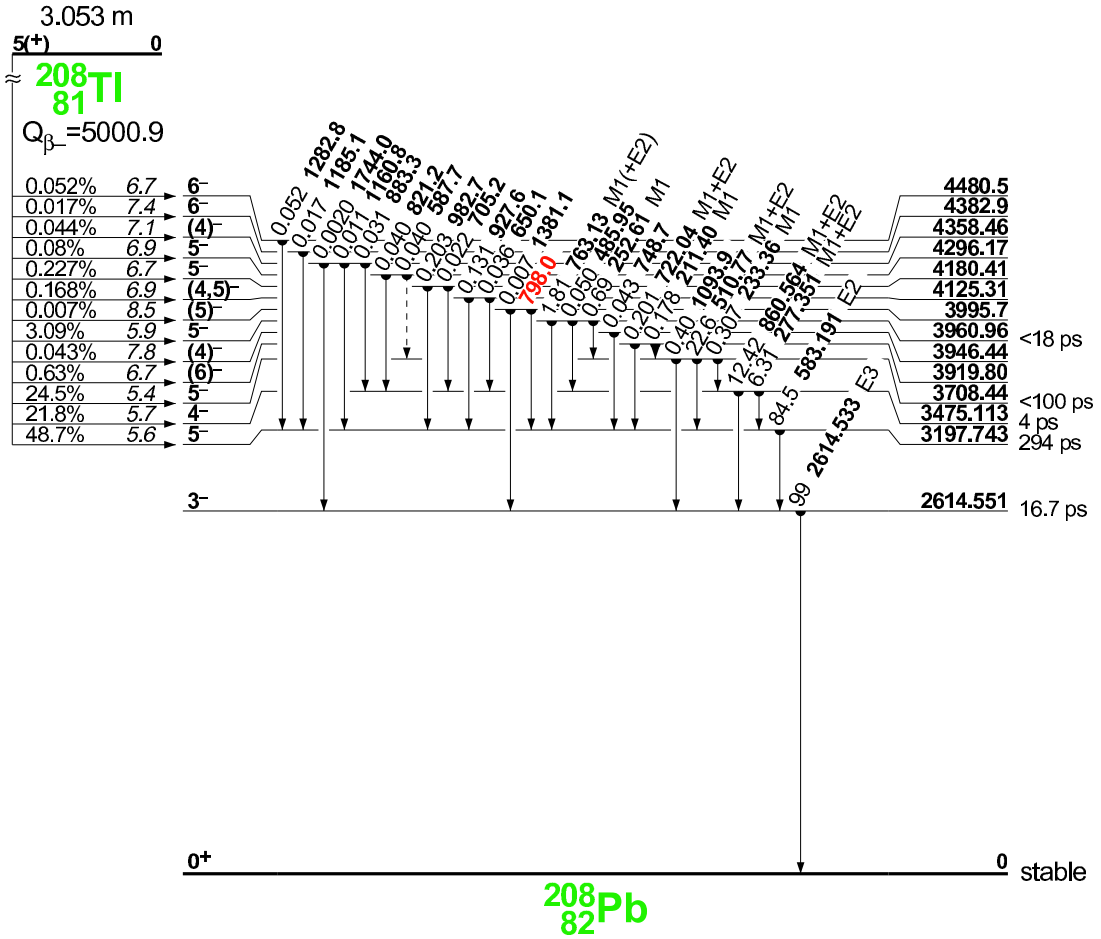

Figure 4.24: The decay scheme of ^{208}Tl [72].

The full spectra of the external (figure 4.25) and internal (figure 4.26) source measurement disclose the dominance of the 2615 keV line and its pendants, the single- and double escape peak (SEP at 2104 keV, DEP at 1593 keV). The pulser peak is at 3 MeV. Further lines from decays of ^{208}Tl (e.g. 583 keV, 860 keV), and ^{212}Bi (e.g. 727 keV, 1621 keV) are visible in both spectra, both isotopes of which are progenies in the natural decay chain (see appendix C). Many faint lines become observable only after the LAr veto cut is applied; for instance the 239 keV line of ^{212}Pb in the external spectrum. Naturally, low energy lines that are present in the inner source spectrum, do not overcome absorption on their way through the argon to occur in the external spectrum. Again, both spectra exhibit *coincident* gamma lines, which are suppressed differently well according to the source position; and *single* gammas, which remain unsuppressed by the LAr veto. The PSD works equally for the full energy peaks in both source positions.

The fundamental difference of the suppression mechanisms underlying the PSD and LAr veto is best illustrated at three peaks: The DEP at 1593 keV, the *single* 1621 keV peak of ^{212}Bi, and the *coincident* 2615 keV peak. Close-ups of these peaks from the 'inner' spectrum are shown in figure 4.27. The corresponding survival probabilities are found in table 4.6,

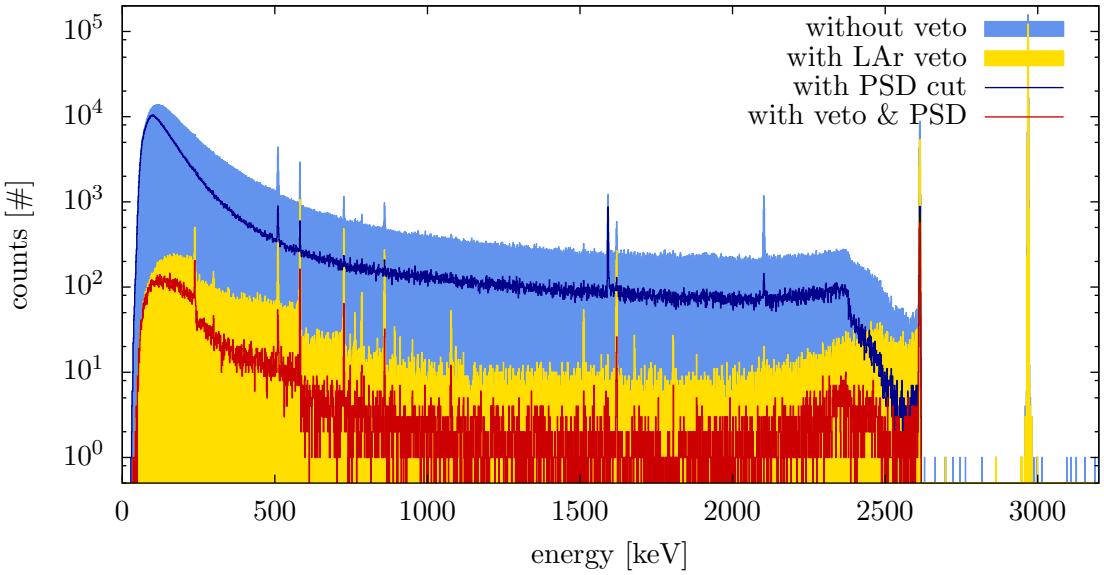

Figure 4.25: The external ^{228}Th spectrum. The visible gamma lines are from ^{208}Tl (511 keV, 583 keV, 860 keV, 1593 keV (DEP), 2104 (SEP), 2615 keV) and ^{212}Bi (727 keV, 785 keV, 1079 keV, 1621 keV). Further lines appear only after the LAr veto cut is applied (e.g. 239 keV from ^{212}Pb). The RoI of $Q_{\beta\beta}$ (2039 keV) is dominated by the Compton spectrum of the 2615 keV line from ^{208}Tl. The pulser is put at 3 MeV.

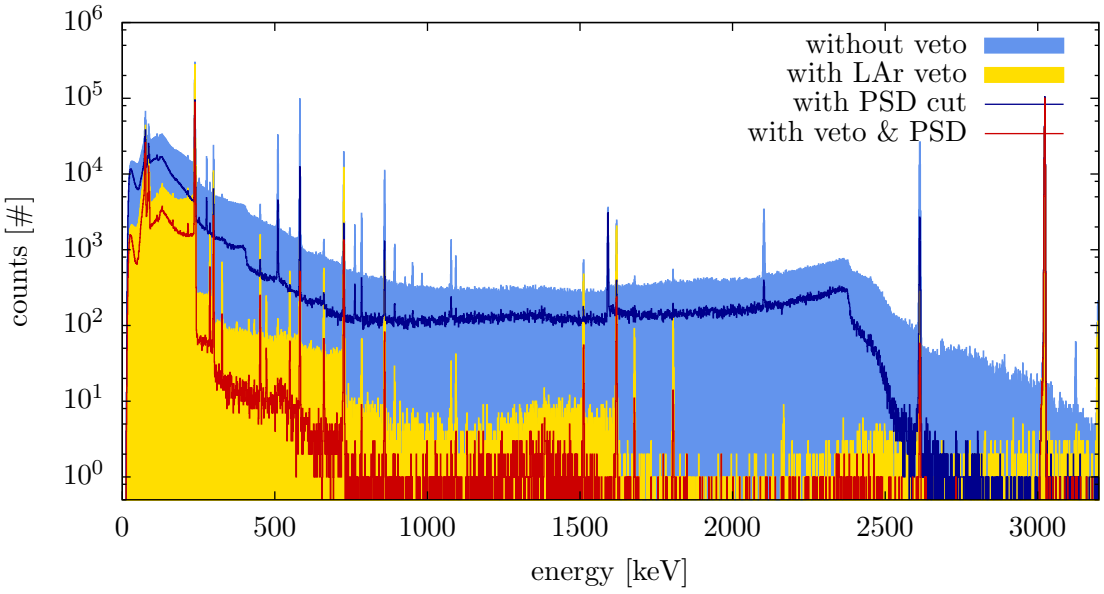

Figure 4.26: The internal ^{228}Th spectrum. In addition to the lines of the external spectrum, many fainter peaks appear – particularly at lower energies. *Single* and *coincident* gamma lines can be distinguished by the different suppression efficiency of the LAr veto. The pulser is set to 3 MeV.

Table 4.6: The *survival probabilities* for different peaks and the RoI of $Q_{\beta\beta}$ for the internal and external ^{228}Th spectrum: The numbers are given for the LAr veto and PSD separately, as well as for their combination (column 'total'). The pulser peaks are used to determine the *acceptance* of the LAr veto. The survival probabilities that include the LAr suppression are corrected for the acceptance (see section 4.4.2).

position	region	energy [keV]	survival probability [%] LAr veto	PSD	total
internal	peak	1621	98.8 ± 2.3	10.7 ± 1.3	11.77 ± 0.79
	DEP peak	1593	-0.28 ± 0.15	90.0 ± 2.2	-0.033 ± 0.047
	SEP peak	2104	0.009 ± 0.029	7.54 ± 0.80	-0.009 ± 0.015
	FEP peak	2615	2.116 ± 0.052	10.04 ± 0.63	0.189 ± 0.018
	RoI	$2004 - 2074$	0.085 ± 0.018	41.6 ± 1.3	0.0193 ± 0.0086
	pulser	3020	95.74 ± 0.26 (LAr-veto acceptance)		
external	peak	1621	94.3 ± 8.5	10.4 ± 4.7	8.73 ± 1.57
	DEP peak	1593	0.14 ± 0.73	76.9 ± 4.3	-0.36 ± 0.37
	SEP peak	2104	0.94 ± 0.54	7.9 ± 1.3	0.07 ± 0.22
	FEP peak	2615	78.0 ± 0.78	10.24 ± 0.58	8.12 ± 0.47
	RoI	$2004 - 2074$	4.0 ± 0.19	35.5 ± 1.3	0.778 ± 0.088
	pulser	3020	78.32 ± 0.20 (LAr-veto acceptance)		

and are given in brackets in this paragraph. The DEP serves as a reference SSE sample for the PSD calibration. As such, its survival probability is tuned to 90% PSD acceptance, which represents a largely unsuppressed line by the PSD. The contrary is true for the LAr veto. The two 511 keV annihilation photons, that escape the Ge-diode, trigger the LAr veto reliably: The DEP vanishes entirely (-0.28±0.15). The neighbouring *single*[1] 1621 keV full energy peak (FEP) of ^{212}Bi is suppressed decently by the PSD (11%), but is not affected by the LAr veto (98.8%). The PSD suppression for the 2615 keV peak is similar (10%), as both peaks are FEPs and contain a large fraction of MSE. But by being a *coincident* gamma line, the LAr veto suppression for the 2615 keV peak is efficient (2%).

The RoI of the $0\nu\beta\beta$-decay is a flat Compton region before and after the cuts in both spectra, the internal (figure 4.28) and the external (figure 4.29). The peak at 2104 keV is the SEP of the 2615 keV line. Again, a 70 keV wide window around $Q_{\beta\beta}$ was chosen for the determination of the survival probabilities. The PSD cut is survived by 42% (internal) and 36% (external) of the events. The LAr veto reduces the Compton 'background' to 0.09% (internal), which corresponds to a suppression by more than three orders of magnitude (suppression factor 1180). For the external source, the LAr veto suppression is still 4% (factor 25) – despite the strong angular dependence of the coincident gammas. For comparison, the 2615 keV FEP is vetoed to only 78%. The suppression in the RoI is so much better, because the excess energy of the 2615 keV gamma is 610–680 keV; too much to slip

[1] Interestingly, the 1621 keV line is *single*, although the subsequent decay of ^{212}Po to ^{208}Pb has a lifetime of only 0.3 μs. The only emitted particle is an alpha particle, which must have been absorbed before leaving the source. Hence, it cannot trigger the LAr veto, and 1621 keV becomes effectively a *single* line.

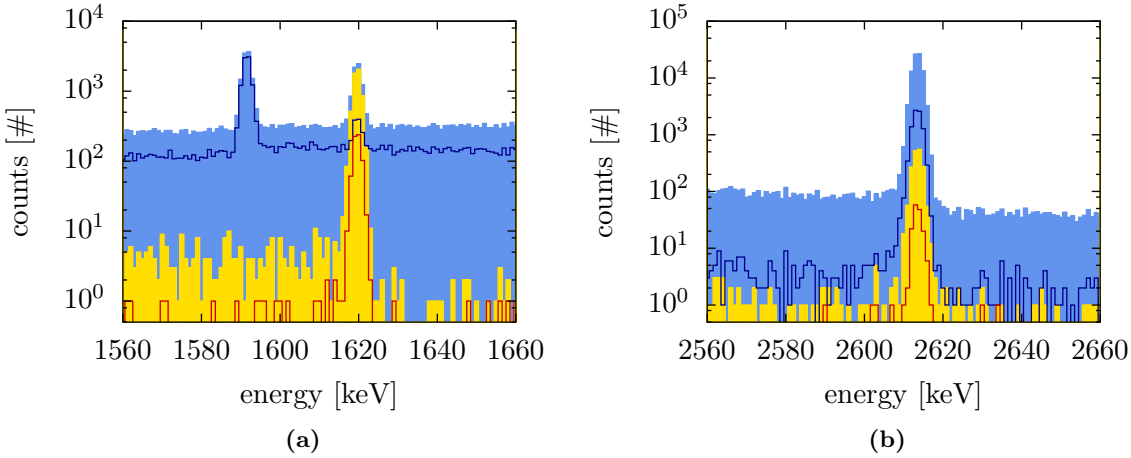

Figure 4.27: **(a)** The double escape peak of ^{208}Tl at 1593 keV, and the 1621 keV full energy peak of ^{212}Bi. **(b)** The full energy peak of ^{208}Tl at 2615 keV. The three peaks illustrate the different rejection principles, by which PSD and LAr veto select their events. See the text for explanation.

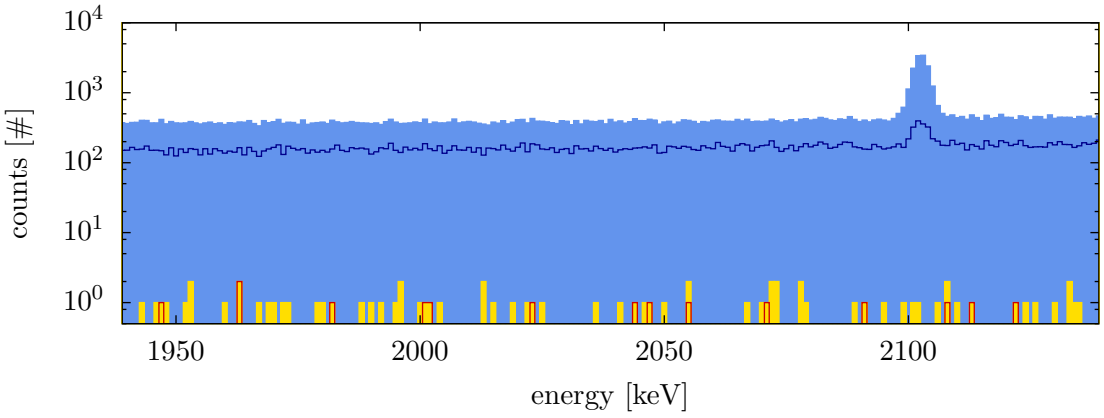

Figure 4.28: The RoI of the $0\nu\beta\beta$-decay around 2039 keV of the internal ^{228}Th spectrum. The LAr veto works very effectively and reduces the Compton 'background' to 0.09% (*suppression factor* 1180). In combination with the PSD, only 5 counts are left in a 70 keV wide window around $Q_{\beta\beta}$ (red contour line). The total *survival probability* is 0.02% (factor 5200). The peak at 2104 keV is a single escape peak of ^{208}Tl.

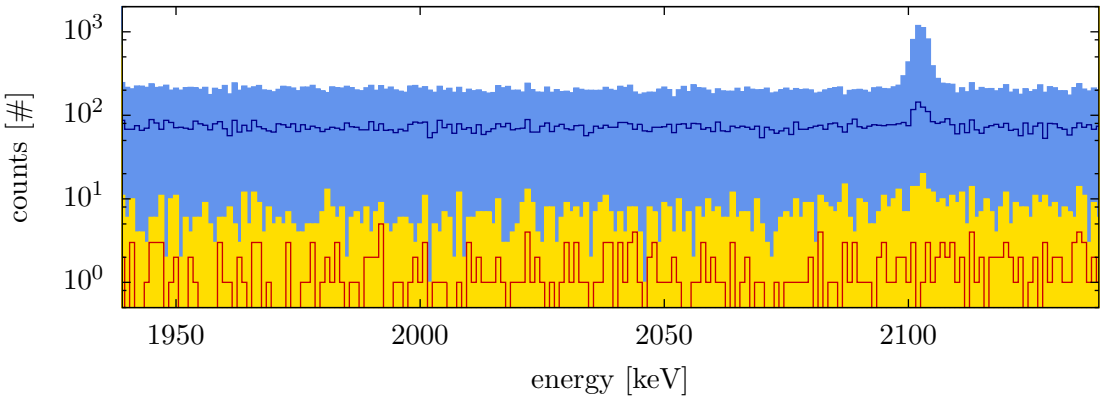

Figure 4.29: The RoI at $Q_{\beta\beta}$ of the external ^{228}Th spectrum. The *survival probability* of the LAr veto is 4% (*suppression factor* 25), and 36% (factor 2.8) for the PSD. The combined suppression of PSD and LAr veto is 0.8% (factor 129). The peak at 2104 keV is the single escape peak of ^{208}Tl.

through the LAr unnoticed. The combined suppression of both cuts is 0.02% (internal) and 0.8% (external). The respective suppression factors are 5200±2300 (internal) and 129±14 (external). The statistical uncertainty of the survival probability for the internal ROI is particularly large (45%), since only 5 counts survive both cuts – of initially 27500 counts in the unsuppressed spectrum.

4.5 Discussion of results

The suppression factors of sources with a contribution to the ROI of the $0\nu\beta\beta$-decay are summarized in table 4.7. These numbers sketch the order of magnitude, by which background rejection in GERDA may be achievable. The large variation of the suppression factors is consistant with our understanding of the underlying physics. Generally, outer sources are suppressed worse by the LAr veto than inner sources, whereas the PSD is largely position independent. More important, however, seems to be the nature of the gamma radiation: For example, the LAr-veto suppression in the ROI for ^{226}Ra is far inferior, than for ^{228}Th; the reason being, that gammas from the ^{226}Ra decay-chain are mostly *single*, and have little excess energy above 2039 keV to trigger the veto. And the contrary is true for the ^{228}Th chain, with its dominating *coincident* 2615 keV line.

An improvement of the LAr suppression could be achieved by increasing the photo-electron yield; which would be particularly beneficial for the ^{226}Ra suppression. So far, the light yield in these measurements is hampered by using only 4-5 out of nine PMTs, and by having the *triplett-lifetime* of the argon excimers reduced by a factor 2-3, due to impurities in the LAr (see chapter 3). Though, in spite of these suboptimal conditions, the LAr suppression works robust. Another limitation to the suppression efficiency are dead volumes, such as the Ge-detector's holder or the dead layer (for p-type diodes).

4.5.1 Orthogonality of LAr veto & PSD

How efficient work LAr veto and PSD combined? If the probabilities for the LAr veto and the PSD to reject an event are independent, the cut techniques are called *orthogonal*

Table 4.7: The suppression factors in the ROI of $Q_{\beta\beta}$ (2004-2074 keV), achieved with the LArGe setup. The *orthogonality ratio* describes the mutual enhancement of the cut techniques, and is described in section 4.5.1.

source	position	suppression factor			orthogonality
		LAr veto	PSD	total	ratio R
^{60}Co	int	27 ± 1.7	76 ± 8.7	3900 ± 3000	1.85 ± 1.44
^{226}Ra	ext	3.2 ± 0.2	4.4 ± 0.4	18 ± 3	1.29 ± 0.24
	int	4.6 ± 0.2	4.1 ± 0.2	45 ± 5	2.39 ± 0.31
^{228}Th	ext	25 ± 1.2	2.8 ± 0.1	129 ± 15	1.83 ± 0.22
	int	1180 ± 250	2.4 ± 0.1	5200 ± 2300	1.83 ± 0.90
mean average					1.84 ± 0.17

to each other. Consequently, the total suppression factor (SF_{tot}) must be the product of the individual suppression for the LAr veto (SF_{LAr}) and the PSD (SF_{PSD}): $SF_{tot} = SF_{LAr} \cdot SF_{PSD}$. If the probabilities are correlated, the total suppression may become either greater (negative correlation) or smaller (positive correlation) than the product. Based on this, we define the *orthogonality ratio* R:

$$R = \frac{SF_{tot}}{SF_{LAr} \cdot SF_{PSD}}$$

A value of $R = 1$ means that the cut techniques are orthogonal; for $R \neq 1$ they are not. The third column of table 4.7 shows the ratio R for the measurements in the RoI of $Q_{\beta\beta}$. All sources hold $R > 1$, although the uncertainties are too large to draw conclusions for each measurement individually. However, the mean average and its statistical uncertainty yield a significant result of $R = 1.84 \pm 0.17$. This means, that the cut techniques combine 'over-orthogonal', i.e. they enhance each other mutually. Conversely, an analogue analysis of the investigated full energy peaks of all sources returns an average of $R = 1.007 \pm 0.015$, with none of the peaks significantly deviating from this value.

The result for the RoI implies, that an event that is classified SSE, is more likely to evoke a LAr veto. Such an event has deposited 2039±35 keV in the RoI in a single interaction. The probability for this to happen via the photoelectric effect is negligible. Pair production is highly MSE, considering that a double escape of the annihilation photons would push most events below the RoI energy. Therefore, these SSE are preferentially Compton-scattered gammas, which leave the crystal immediately after the interaction. Gammas from MSE, on the other hand, have possibly ended their trajectory in the detector via pair production or the photoelectric effect. A quantitative detailed MC study is beyond the scope of this work.

4.5.2 Acceptance for $0\nu\beta\beta$-events

The results for the LAr veto show, that events that deposit all of their energy inside the Ge-diode are not suppressed. The survival probabilities of full energy peaks from *single* gammas match with 100% throughout the measurements, all but two within 1σ. For the 'cleanest' sample of a *single* peak – ^{137}Cs – the survival probability is (99.5±2.7)%. Since $0\nu\beta\beta$-events also confine their energy deposition to the Ge-detector, the acceptance for these events is directly given by the acceptance of the LAr veto. Without a source, the acceptance in LArGe was determined to be 97.3%.

The PSD is fixed to 90% acceptance of DEP events from ^{208}Tl. In both, the DEP and $0\nu\beta\beta$-events, hard bremsstrahlung may be created and either leave the active volume of the Ge-diode, or turn the event to a MSE. For the DEP, this is taken into account for through the calibration (see section 4.2.2). For the $0\nu\beta\beta$-decay the fraction of MSE is higher, due to an increased probability for bremsstrahlung of the energetically higher electrons. Thus, the surviving fraction for $0\nu\beta\beta$-events is expected to be lower, at (86±3)% [69].

It is conceivable, that bremsstrahlung from a $0\nu\beta\beta$-decay leaves the crystal and triggers the LAr veto. In order to miss a 'good' event from the $0\nu\beta\beta$-peak, two conditions must be fulfilled: 1) the missing energy due to the bremsstrahlung must be smaller than the chosen RoI of the peak, say ∼4 keV; 2) the escaped x-ray of ∼4 keV must leave the crystal and

trigger the LAr veto. While the creation of $\lesssim$4 keV bremsstrahlung is highly unlikely, the emitted x-ray would be absorbed in the dead layer of the Ge-detector (for p-type diodes). Even if the x-ray reaches the LAr, it would take a strongly improved photo-electron yield at the Mini-LArGe level (1.24 pe/keV, [37]) to trigger the veto. Therefore, with this effect being negligible, the acceptance for $0\nu\beta\beta$-events by PSD and the LAr veto is decoupled, and hence may be multiplied to obtain the combined acceptance.

4.5.3 Comparison to Monte Carlo predictions

In the PhD thesis by Peiffer [36] a Monte Carlo (MC) simulation of the LAr-scintillation suppression efficiencies was conducted. First, the MC model (using the MaGe simulation package [73]) was verified for various sources by comparison to experimental data from Mini-LArGe. Then, MC simulations were performed in LArGe-geometry, using a 2 kg HPGe diode submerged into one ton active LAr-volume (⌀=90 cm, h=155 cm).

For two sources, the suppression efficiencies in the RoI of $Q_{\beta\beta}$ are provided: The simulation of a point-like ^{208}Tl gamma source inside the LAr and close to the Ge-diode yields a suppression factor of 338±8 (survival probability (0.296±0.007)%). With a correction factor, that accounts for discrepancies between MC predictions and the Mini-LArGe data, the suppression factor turns into a conservative lower limit of ∼145. The second simulated isotope is internal ^{214}Bi, with a suppression factor of 8.0±0.1 (survival probability (12.5±0.2)%), and a corrected lower limit of ∼6.

Now for the LArGe measurements presented in this work, the inner ^{228}Th spectrum, dominated by ^{208}Tl, yields a suppression factor of 1180±250. This exceeds the prediction by a factor 3.5 to 8. On the other hand, the inner ^{226}Ra measurement (^{214}Bi) falls below the prediction with a suppression factor of 4.6±0.2; a factor 0.77 below the conservative lower limit.

A robust explanation for the discrepancy of experiment and MC cannot be given without detailed studies of the MC model. However, the MC implementation is different to the experiment in two major aspects: (1) the weight of the Ge-detector in the simulation is 2.5 times higher than BEGe, and (2) the energy threshold is chosen to be 2.5 keV, instead of $\sim$ 20 keV in the real setup. Moreover, it is conceivable that the correction factor cannot be forthrightly scaled from Mini-LArGe to LArGe geometry, as it is not entirely understood. The comparison shows nevertheless, that the aspired suppression goals have been achieved.

Chapter 5

First background measurements

As LArGe is designed as an ultra-low background setup, the achieved background level is a key benchmark to its success. At the same time it must be demonstrated, that the benefit of LAr-suppression does not come at a higher cost of additional background from the LAr-instrumentation. The measurements presented in this section are the first background measurements in LArGe, yet without applying PSD, and the shielding remaining unfinished.

5.1 BEGe detector without source

An energy spectrum without a source has been taken with the BEGe detector with a total of 18.6 days aquisition time. Since the prototype CC2-preamplifier is build on a conventional non-low-background printed circuit board (PCB), we do not consider this a valid measurement of the LArGe background. The spectrum – shown in figure 5.1 – exhibits all major gamma-lines from the natural decay-chains ^{232}Th and ^{226}Ra, as well as from ^{40}K. At low energies the spectrum is dominated by bremsstrahlung of ^{39}Ar, with a maximum around 100 keV. At higher energies >1.5 MeV the main contribution comes from the Compton continuum of ^{208}Tl. To verify the location of the contaminations, we can use the obtained suppression efficiencies from the previous chapter, in addition to the standard method of line intensity ratios (energy dependent transmission probability). The survival probability of the 2615 keV ^{208}Tl peak after the LAr veto is (8.2±2.1)% (corrected for the pulser acceptance of 97.3%) – a close-up is shown in figure 5.2. By comparison with the survival probability for the internal ^{228}Th source measurement, 2.1% (table 4.6), and the external source, 78%, one can infer that the observed ^{208}Tl contamination is located mostly close to the Ge-diode. This supports the assumption, that the main source of 'background' in this measurement is related with the presumably non-low background PCB. The principle of using the source measurements as a library to locate contaminations can be refined by more sophisticated analysis, e.g. by taking into account other isotopes and/or get support from MC simulations.

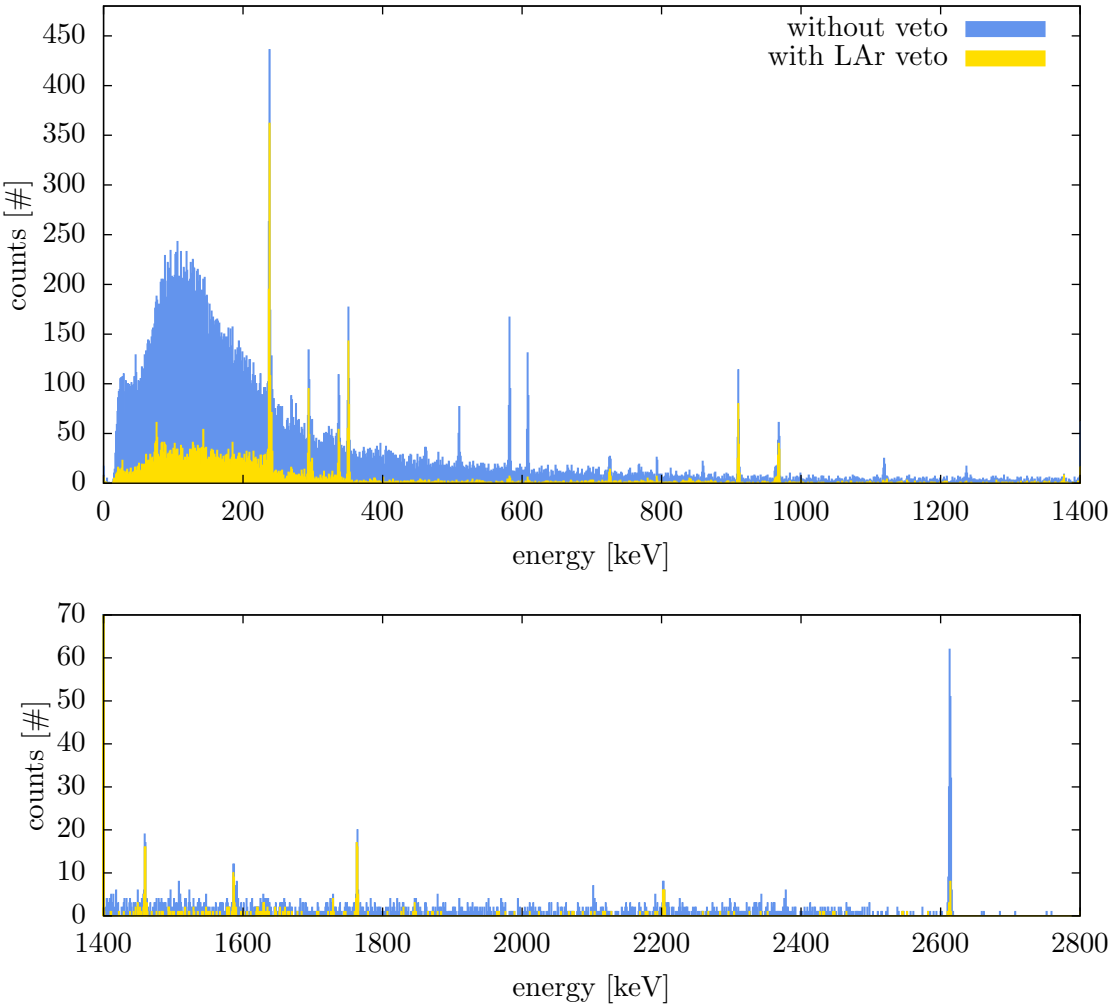

Figure 5.1: Energy spectrum of the BEGe detector without source, split in two parts. At high energies >1.5 MeV the spectrum is dominated by the intrinsic contaminations of the CC2 prototype preamplifier, mainly due to the Compton continuum of the 2615 keV ^{208}Tl-peak. The pulser acceptance for the LAr veto is 97.3%.

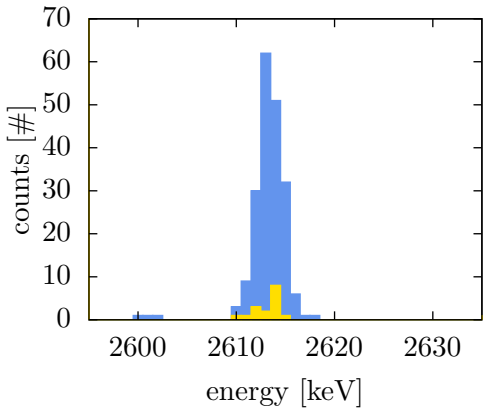

Figure 5.2: The 2615 keV ^{208}Tl-peak in the spectrum of the BEGe detector. The survival probability of (8.2±2.1)% suggests that the contamination is close to the Ge-detector.

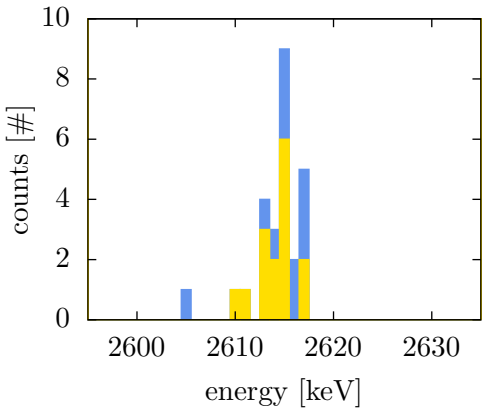

Figure 5.3: The 2615 keV ^{208}Tl-peak in the GTF44 background spectrum. The survival probability of (66±27)% indicates an external location of the background source.

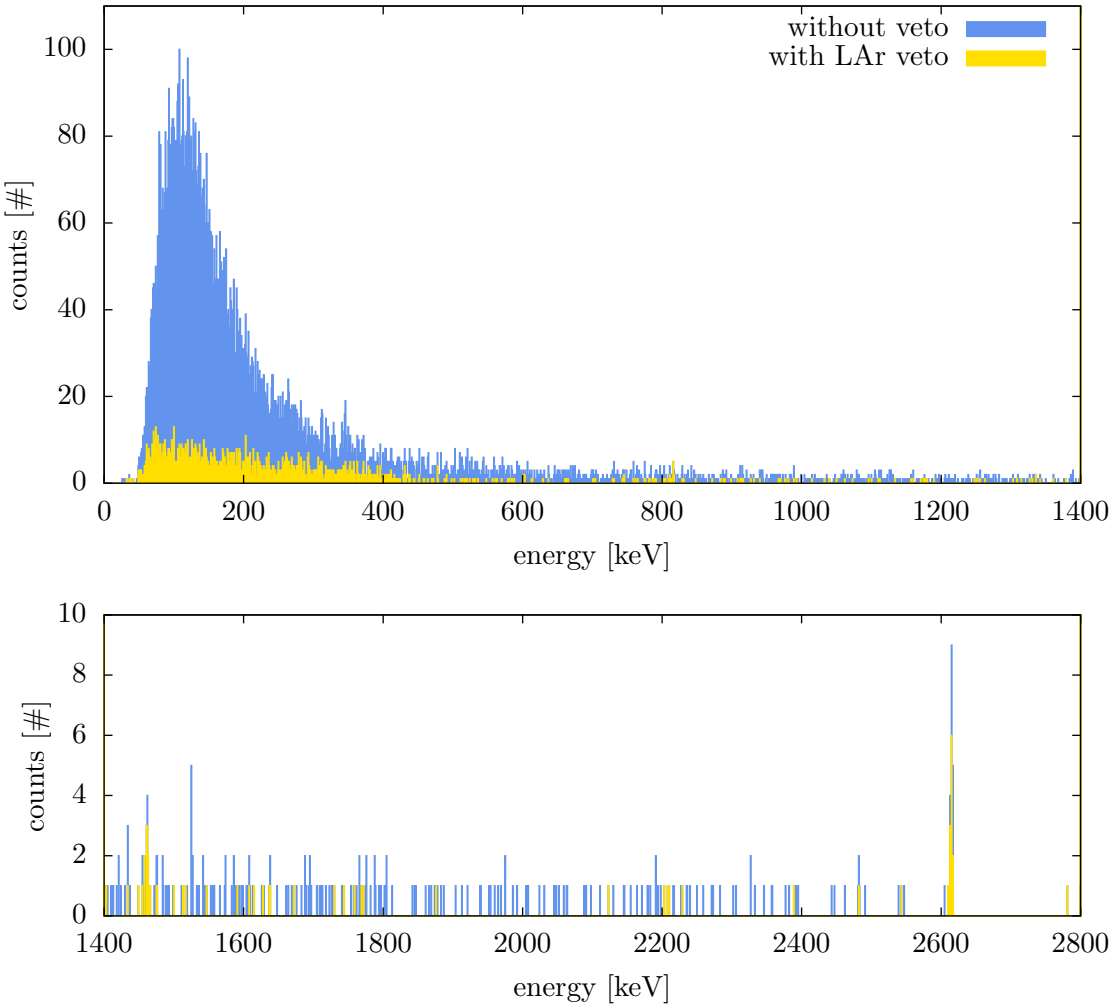

Figure 5.4: The background spectrum of LArGe measured with the GTF44 detector. The total aquisition time is 47.05 days, which corresponds to 116 kg·d exposure. The pulser acceptance for the LAr veto is 91%.

5.2 Background with GTF44

The low-background non-enriched GTF44 detector was inserted into LArGe to achieve a higher sensitivity, with the main intention to study the ^{42}Ar background, which is currently observed in GERDA. GTF44 has a higher mass (m = 2465 g) than BEGe (878 g), and is equipped with a low-background preamplifier. Furthermore, the lead shield of LArGe was build-up on the side to the height of the cryostat's top flange (compare with figure 2.3), and the LAr was exchanged with argon of higher purity from the WARP experiment, to increase the photo electron yield – thus to decrease the LAr-veto's threshold. The full energy spectrum of this background measurement is shown in figure 5.4. The total aquisition time is 47.05 days, which corresponds to 116 kg·d exposure, and the achieved resolution is 3.5 keV FWHM at 1332 keV. Since the measurement is ongoing and very recent data is included, the results presented in this section are preliminary.

Table 5.1: Counts and background rates with the encapsuled GTF44 detector in LArGe. Compton background is subtracted from the full energy peaks. The background index is given for different intervals around $Q_{\beta\beta}$. Uncertainties are given with $\pm 1\sigma$, or 90% confidence interval (see text) [74].

region	energy [keV]	counts [#] without veto	counts [#] with veto	count rate [cts/(kg·d)] without veto	count rate [cts/(kg·d)] with veto
^{40}K	1457 - 1465	14	11	0.095 ± 0.034	0.082 ± 0.030
^{42}K	1523 - 1527	7	0	0.049 ± 0.023	< 0.02
^{208}Tl	2610 - 2619	25	15	0.211 ± 0.043	0.129 ± 0.033
				bg index [cts/(keV·kg·y)]	
RoI	1989 - 2089	14	0	0.44 ± 0.12	$< 7.2 \cdot 10^{-2}$
	1939 - 2139	30	1	0.47 ± 0.09	$0.17 - 6.8 \cdot 10^{-2}$
	1889 - 2189	40	1	0.43 ± 0.07	$0.12 - 4.6 \cdot 10^{-2}$

Again, the dominant background at energies >1.5 MeV is from the 2615 keV line of ^{208}Tl – a close-up of which is shown in figure 5.3. A LAr-veto survival probability of (66±27)% indicates, that the origin of the ^{228}Th contamination is mostly external to the cryostat, presumably from the photomultipliers. The pulser acceptance is 91%. Other background lines are from natural ^{40}K (1461 keV), and ^{214}Bi (1764 keV, 2204 keV) – which are *single* lines, and hence barely suppressed by the veto. A line at 811 keV stems from ^{58}Co (halflife 70.9 days), which was cosmogenically produced in the copper-encapsulation during production, shortly before this measurement started. The background count rates discussed in this chapter are given in table 5.1.

5.2.1 ^{42}Ar abundance

The GERDA commissioning of Ge-detectors is currently ongoing, with the main focus on the study of the background level. A string of three non-enriched GTF Ge-diodes has been deployed, and so far background data have been recorded in different running conditions with a total exposure of 1.7 kg·y [75]. Though the count rate in the RoI at $Q_{\beta\beta} = 2039$ keV during the ongoing commissioning run is significantly lower than the 0.11 cts/(keV·kg·y) observed in the HdM experiment [76], the achieved background index measured with the non-enriched Ge-detectors is yet above the phase I specifications of $<10^{-2}$ cts/(keV·kg·y). At least in the initial commissioning runs, a large fraction of these events is created by β-decays of ^{42}K ($Q = 3.5$ MeV, $T_{1/2} = 12$h). The 1525 keV gamma-line is also seen in the background spectrum of GERDA– see the decay scheme of ^{42}K in figure 5.5. ^{42}K is the progeny of ^{42}Ar, which is a β-emitter with $Q = 600$ keV and $T_{1/2} = 32.9$ y.

The expected ^{42}Ar background contribution has been considered in the GERDA design, based on the best experimental limit available from the DBA experiment, $^{42}\mathrm{Ar}/^{nat}\mathrm{Ar} < 4.3 \cdot 10^{-21}$ g/g (90% confidence level, c.l.) [77]. The measured count rate at 1525 keV in GERDA is almost one order of magnitude higher than when adopting this limit, assuming a homogeneous distribution of ^{42}Ar in the liquid argon. In addition, to explain the high count rate above the line, ^{42}K ions must be created from the ^{42}Ar β-decay and drift towards

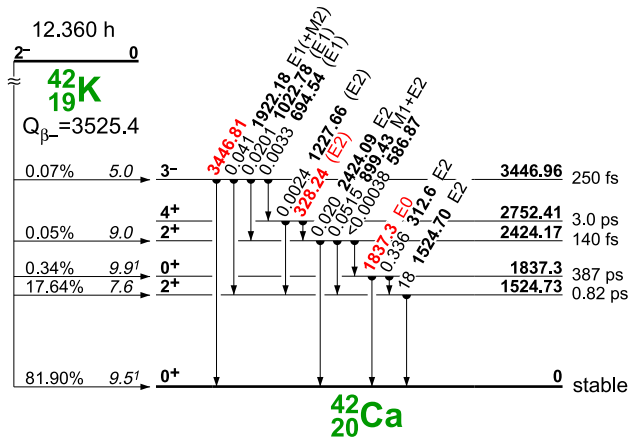

Figure 5.5: The decay scheme of ^{42}K, progeny of the β-emitter ^{42}Ar [72].

the Ge-diodes. In fact, in GERDA we observe that the count rate of ^{42}K depends on the electrical field in the liquid argon close to the detectors.

In parallel to GERDA, we use the LArGe setup to study the ^{42}Ar related background. The encapsulation of the GTF44 detector is grounded, to shield the argon from the electric field, and avoid the drift of ^{42}K ions. A close-up of the energy region around 1525 keV is shown in figure 5.6. In a 5 keV interval (1523 - 1527 keV) around the peak 7 counts are found (without veto). The Compton background is determined in the range 1480 - 1580 keV (26 counts, excluding the peak interval), which leads to an estimated background contribution of b = (1.35±0.27) counts in the peak. Therewith, the *decision threshold* $DT = k_{1-\alpha} \cdot \sqrt{2b} = 2.71$ ($k_{1-\alpha} = 1.645$ for 95% c.l.) [78] is calculated and compared to the number of net-counts n = 5.65 in the peak. Since $DT < n$, the null hypothesis is rejected, and we conclude that the ^{42}Ar signal is significant. The count rate in the peak is (0.049±0.023) cts/(kg·d).

For ^{42}K being distributed across the argon volume, we expect the LAr veto to work efficiently, since it will be triggered by β-particles from the decay. Indeed, we observe no counts in the 1525 keV peak after the veto. Hence, by selecting counts *in coincidence* with scintillation light, we can reject some of the background events without losing signal. Therewith, 22 (out of 26) background counts remain (n = 5.85), and the count rate changes slightly to (0.050±0.023) cts/(kg·d). In contrast, the average count rate over three detectors in GERDA is (0.35±0.05) cts/(kg·d) [79] – a factor 7 higher than measured in LArGe.

Under the assumption that the ^{42}K decays are homogeneously distributed in the LAr, we can calculate the natural ^{42}Ar abundance of this argon sample from the observed 1525 keV signal. For the time being, we can not exclude that the electrical field generated by the PMTs and the grounded cryostat wall (and detector encapsulation) drifts ^{42}K ions away from the detector, such that the apparent ^{42}Ar concentration is lower than the true one. This could also reconcile the results in LArGe with those of GERDA. The dominant production mechanism of ^{42}K is through cosmic rays in the upper atmosphere [80]. Since ^{42}K and ^{42}Ar are in radioactive equilibrium, we obtain the abundance directly from the specific activity A_{spec} of ^{42}K in LAr,

$$A_{spec} = \frac{n}{\epsilon_{det} \cdot \epsilon_{br} \cdot t \cdot m} = (2.2 \pm 1.0) \cdot 10^{-8}\, Bq/g$$

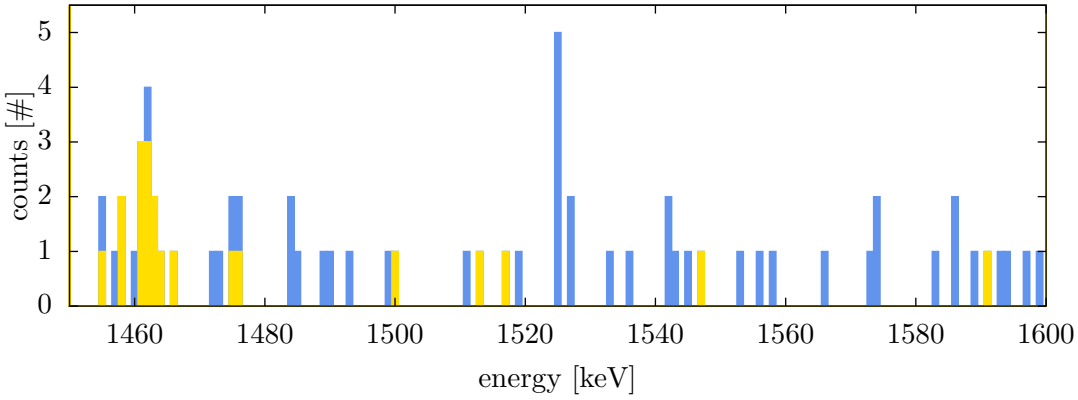

Figure 5.6: Close-up of the energy region around the 1525 keV ^{42}K-peak. None of the 7 counts in the peak (1523-1527 keV) survives the LAr veto cut. The peak at 1460 keV is from ^{40}K.

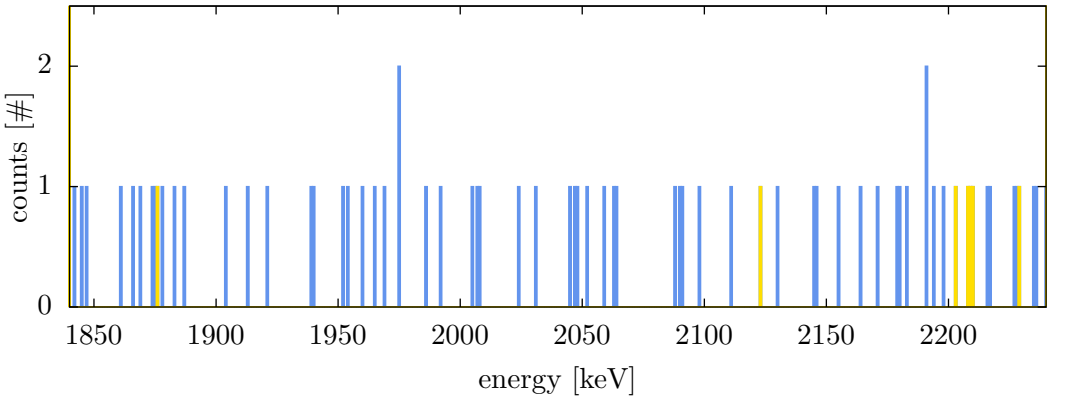

Figure 5.7: The LArGe background in the RoI of the $0\nu\beta\beta$-decay. In the vetoed spectrum (yellow) only one count is present in a 300 keV interval around $Q_{\beta\beta} = 2039$ keV, and no count in a 100 keV interval. A ^{214}Bi peak appears at 2204 keV. The exposure is 116 kg·d (47.05 days).

The detection efficiency ϵ_{det} was determined independently by two MC simulations, yielding an average of $\epsilon_{det} = (2.80 \pm 0.35) \cdot 10^{-4}$ [81]. The branching ratio of the 2+ state is $\epsilon_{br} = 17.64\%$ [72], t is the aquisition time, and m the total argon mass (1.34 tons). Translated into molecular concentration, this gives

$$^{42}Ar/^{nat}Ar = (2.2 \pm 1.0) \cdot 10^{-21}\, g/g \tag{5.1}$$

The measurements in GERDA and LArGe are the first measurements of the ^{42}Ar abundance in natural argon. The result is below the current upper limit $< 4.3 \cdot 10^{-21}$ g/g from the DBA experiment and the most recent theoretical prediction of $\sim 10^{-20}$ g/g [80]. The currently ongoing measuring program in LArGe aims to clarify the question, whether the ^{42}K decays are homogeneously distributed, and whether there are positive and negative ^{42}K ions produced in the ^{42}Ar β-decay in liquid argon. Furthermore, LArGe can contribute the investigation, e.g. by measuring the ^{42}Ar concentration in different argon batches, and test the common assumption of a homogenous ^{42}Ar mixture in the atmosphere.

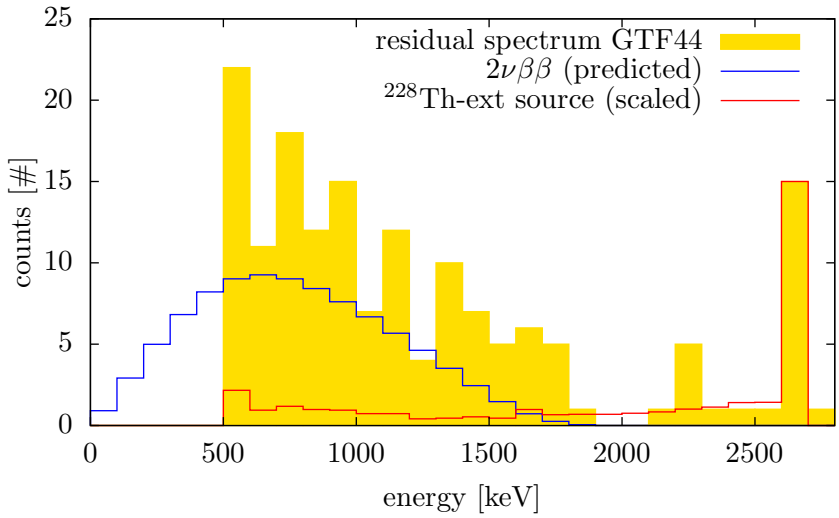

Figure 5.8: Residual spectrum of GTF44, after subtracting the 811 keV and 1460 keV lines, and truncated below the analysis range (yellow). Also, the expected contribution from the $2\nu\beta\beta$-decay, and the Compton background from ^{208}Tl. Half of the counts in the residual spectrum are due to $2\nu\beta\beta$-events.

5.2.2 Background index at $Q_{\beta\beta}$

A close-up of the RoI around $Q_{\beta\beta}$ is shown in figure 5.7. In the vetoed spectrum (yellow) only one count is present in a 300 keV interval around $Q_{\beta\beta}$, and no count in a 100 keV interval – more numbers are given in table 5.1. For the resulting background index after the veto cut, the 90% confidence intervals are determined for 'the mean of a Poisson variable in the absence of background' – according to [74]. The achieved background index is $< 7.2 \cdot 10^{-2}$ cts/(keV·kg·y), with precise limits depending on the chosen energy interval. Yet, the lower limits of all confidence intervals cover the aspired background index of $\leq 10^{-2}$ cts/(keV·kg·y), which is the design goal of LArGe and GERDA phase I. Lower backgrounds are possible with LArGe, when the shielding is completed, and a PSD is applied.

5.2.3 $2\nu\beta\beta$ spectrum

The low background raises the question, whether the $2\nu\beta\beta$-spectrum is observable in the background data; and if the $2\nu\beta\beta$-decay is considered as the signal, what is the signal-to-background ratio? The 'residual spectrum' (yellow) is shown in figure 5.8. It is the vetoed background spectrum with the main gamma lines subtracted, namely 811 keV and 1460 keV. The bin width is chosen 100 keV in order to reduce statistical fluctuations. Since at low energies the ^{39}Ar bremsstrahlung dominates, we confine the analysed range from 500 keV to 2100 keV above the $2\nu\beta\beta$ endpoint. The blue histogram depicts the theoretical prediction for the $2\nu\beta\beta$-spectrum [82, 34] of the GTF44 detector. To get an estimation of the Compton contribution from the 2615 keV line, a spectrum of an external ^{228}Th-source is scaled to fit the background peak (red).

The total number of background counts in the analysed range is 135, out of which 69 events are predicted from $2\nu\beta\beta$. Hence, we obtain a signal-to-background ratio of $S/B =$

69/(135-69) = 1.05, i.e. half of the observed events are expected to stem from the $2\nu\beta\beta$-decay. Out of the remaining background events 13.3 can be attributed to the ^{208}Tl line, the others are not allocated. This would be the first observation of the $2\nu\beta\beta$-decay in natural germanium. Preliminary results from ongoing studies using PSD indicate, that S/B can be further increased to $\sim$5.6, while attributing all residual background to ^{208}Tl [83].

With detectors isotopically enriched to 86% ^{76}Ge (natural abundance 7.44%), the S/B-ratio would be strongly enhanced: based on the presented background level, one would obtain S/B=12 (without PSD). In comparison, the signal-to-background ratio of the Heidelberg-Moscow double-beta decay experiment is roughly $S/B \sim 2$ [34].

Chapter 6

Conclusions & Outlook

LArGe is a GERDA low-background test facility to study novel background suppression methods in a low-background environment, for possible applications in GERDA phase II and beyond. In case that the background goals of GERDA phase I can not be met without instrumenting the LAr, the GERDA collaboration considers to implement a LAr veto already in phase I. This work adresses the design, construction, and commissioning of LArGe, including the detection of argon scintillation light. It is the first time that naked Ge-detectors are operated in a low-background environment with 1 m^3 instrumented LAr. The LAr-scintillation veto has been studied in combination with the pulse shape discrimination (PSD) technique of the BEGe detector. First background results were obtained with the low-background coaxial detector GTF44 (without PSD), including the first measurement of the ^{42}Ar concentration in LAr, and indications for the $2\nu\beta\beta$-decay in a non-enriched detector.

Achieved background suppression

The background suppression efficiency was studied for different gamma sources (^{137}Cs, ^{60}Co, ^{226}Ra, ^{228}Th) in different locations (close-by and external), which represent characteristic background sources to GERDA. The strongest suppression factors were obtained for nearby ^{228}Th, with a combined suppression of PSD and LAr veto by a factor ∼5200, and for nearby ^{60}Co, with a suppression of ∼3900. The suppression capability proved robust against a diminished photo-electron yield due to a limited argon purity and the failure of some of the PMTs. Another application for the LAr veto is background diagnostics. For example, one can discriminate *nearby* background sources from sources *far away*, even on the basis of low statistics – this was shown for the ^{208}Tl background in the BEGe and GTF44 spectra. Moreover, the source measurements provide templates for the analysis of background contributions, as it was utilized in the $2\nu\beta\beta$ analysis.

First results with a low-background detector

First measurements of the LArGe background index yield an excellent preliminary result of (0.12-4.6)·10^{-2} cts/(keV·kg·y) (90% c.l.). The confidence interval coincides with the design goal of GERDA phase I < 10^{-2} cts/(keV·kg·y), without having applied PSD, and

with a partially incomplete outer shielding. Still, it is currently the best background level available in $0\nu\beta\beta$-experiments. In parallel to GERDA, the first measurement of the natural ^{42}Ar abundance in LAr was obtained with the result $^{42}Ar/^{nat}Ar = (2.2 \pm 1.0) \cdot 10^{-21}\, g/g$, assuming a homogeneous distribution of the ^{42}Ar progeny ^{42}K in the LAr. So far, only an experimental upper limit $< 4.3 \cdot 10^{-21}$ g/g [77], and a theoretical value of $\sim 10^{-20}$ g/g [80] have been available. Compared to LArGe, the observed ^{42}Ar signal in GERDA is a factor 7 higher, which might pose a challenge to reach the required background at $Q_{\beta\beta}$. LArGe is the only facility next to GERDA with the sensitivity to that concentration level, and is used in a coherent measurement program to study the ^{42}Ar background of GERDA. A preliminary analysis of the LArGe background after 116 kg·d exposure indicates the observation of the $2\nu\beta\beta$-signal in the non-enriched GTF44 detector. This would be the first measurement of $2\nu\beta\beta$ in a natural germanium detector.

The achievements of LArGe show, that an instrumentation of GERDA with a LAr veto is an attractive and powerful method to suppress residual background signals, if GERDA is limited by backgrounds which deposit part of their energy in LAr. An active LAr shield is a design option for phase II, and presumably essential for an ultimate $0\nu\beta\beta$-experiment with $\mathcal{O}(1\,\text{tonne})$ of enriched germanium to explore the 10 meV mass range.

Appendix A

Photographs of the LArGe assembly

Figure A.1: The LArGe shield during the installation in the northern part of the GDL at LNGS, 2005.

Figure A.2: Insertion of the cryostat into the shield. The cryostat is wrapped in Styropor® for better insulation.

Figure A.3: Grinding of the cryostat inner wall at MPIK Heidelberg (June 2009).

Figure A.4: A view into the cryostat after etching (July 2009).

Figure A.5: The first wavelength-shifter coating-machine with a freshly laminated piece of mirror foil (March 2008).

Figure A.6: Cutting of VM2000 mirror foil during the LArGe assembly in GDL (August 2009).

Figure A.7: Lining of the cryostat with mirror foil. A thin layer of two-component epoxy resin (Araldit) is applied...

Figure A.8: ... and the VM2000 pieces are attached. Care must be taken to avoid air bubbles, which can contaminate the argon.

Figure A.9: A view into the cryostat with completed fitting at assembly.

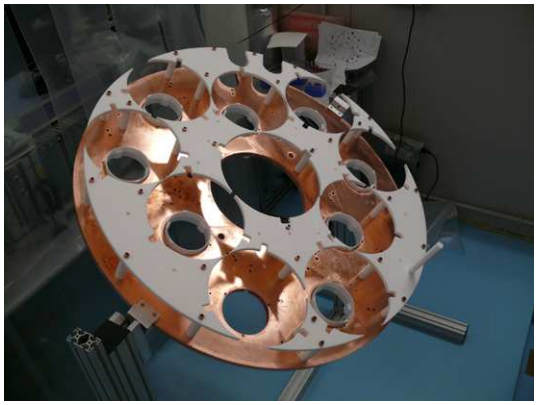

Figure A.10: The PMT support structure in the assembly mount. The Teflon® plates and collars are attached to the copper plate.

Figure A.11: Insertion of a PMT. Each PMT is hold by three thin Teflon® brackets, which grab the edge of the photocathode.

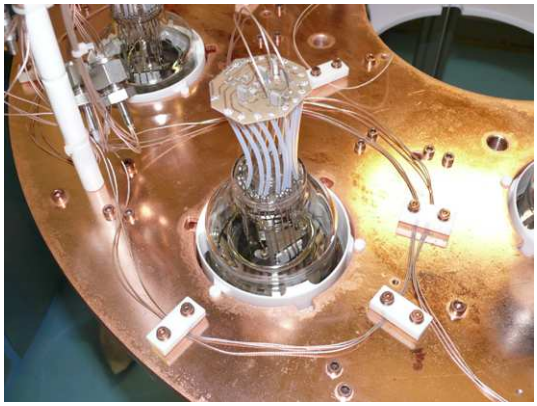

Figure A.12: Top view of a PMT and its voltage divider. The cables are guided on the copper plate by Teflon® clamps.

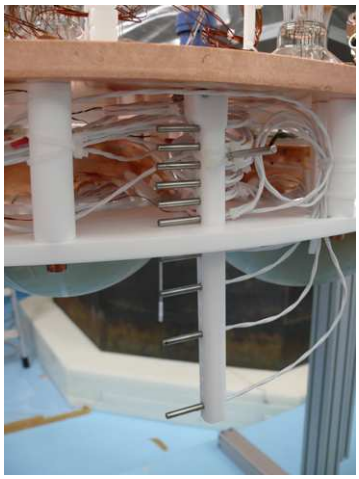

Figure A.13: Twelve PT1000 temperature sensors are attached at the side to monitor the LAr filling level.

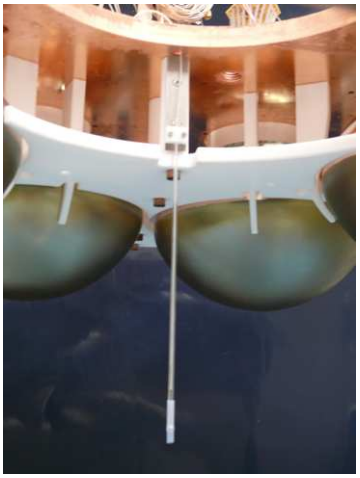

Figure A.14: Three subrasil glass diffusors with an inner optical fibre point downwards from the center hole of the copper plate. They are needed for PMT calibration with a UV LED.

Figure A.15: The PMT support structure ready for insertion into the cryostat.

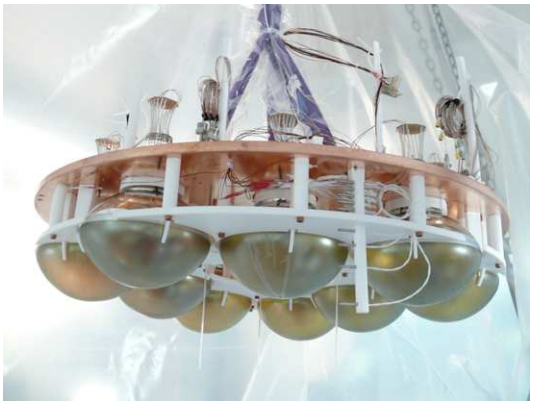

Figure A.16: On the hook ...

Figure A.17: ... and on its way ...

Figure A.18: ... to the final position. The copper plate rests on a metal rim in the cryostat.

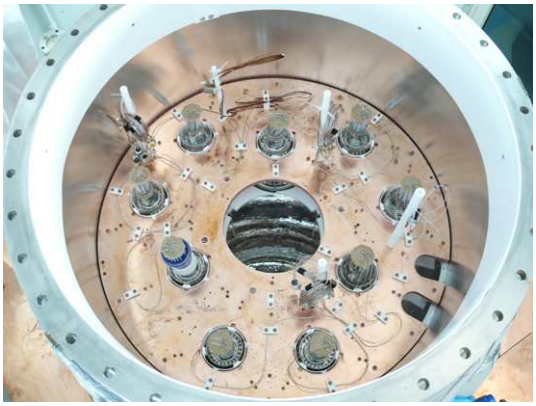

Figure A.19: A view from the top onto the PMT plate in the cryostat.

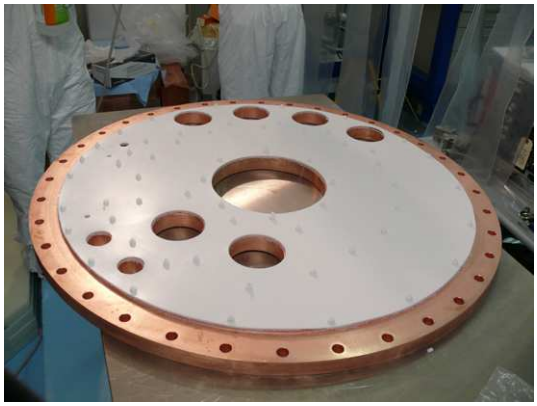

Figure A.20: The bottom side of the 'top flange' of the cryostat. Various thin layers of copper and Teflon sheets form a sandwhich for thermal insulation.

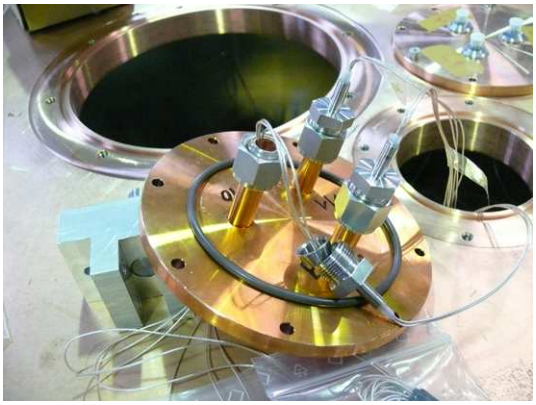

Figure A.21: PMT 'feedthroughs': The three cables of each PMT are glued into a Swagelok® connector, three of which are fixed on the cable flanges.

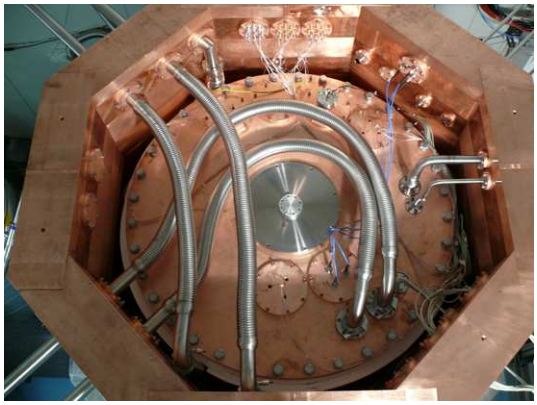

Figure A.22: Top view of the closed cryostat in the shielding. The tubes from the cryogenic system are already installed.

Figure A.23: Orbital welding of the cryotubes on site, after one part has been pushed through the shielding.

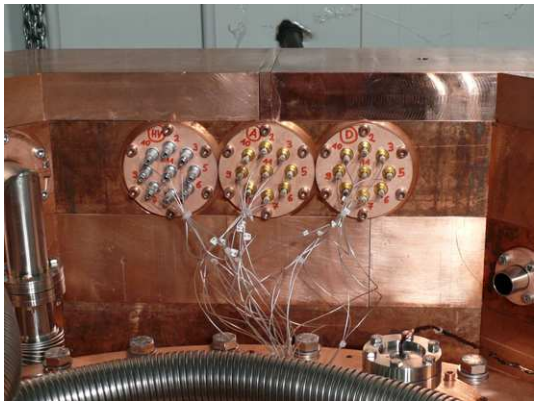

Figure A.24: PMT cable flanges on the shielding: For each PMT there is one HV cable, and two signal cables.

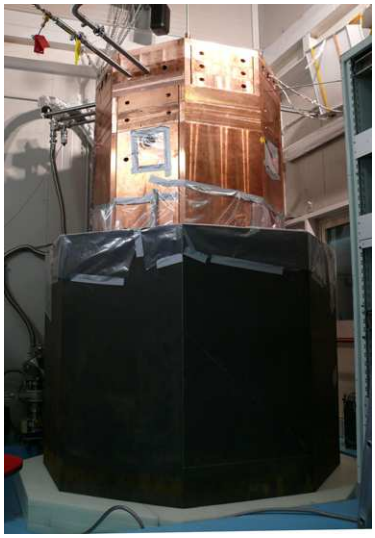

Figure A.25: LArGe from the outside, after insertion of the cryostat.

Figure A.26: The 400 l nitrogen dewar for the active cooling system on a scale, and the 120 l substitue dewar (both still unconnected).

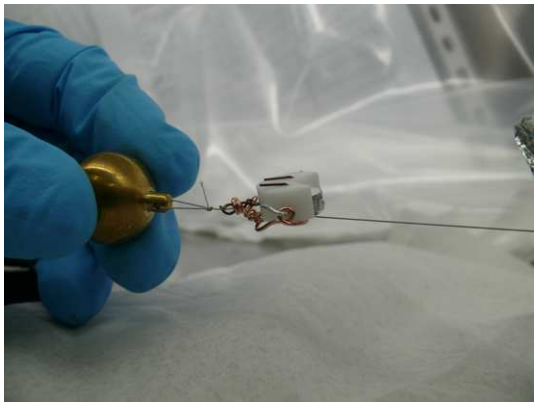

Figure A.27: A ^{148}Gd alpha source on its Teflon holder, and a brass weight.

Figure A.28: The alpha-source manipulator mounted on the 'access cylinder' of the cryostat.

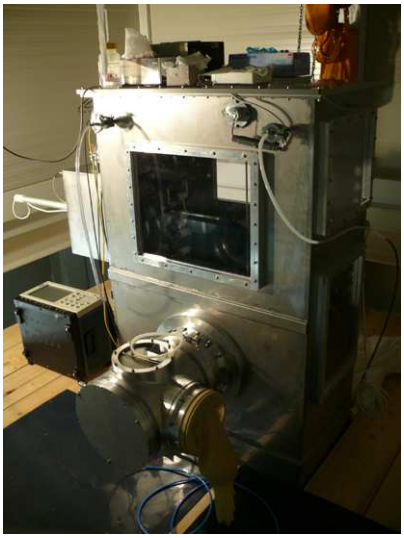

Figure A.29: The main lock with the intermediate lock at the forefront.

Figure A.30: The LArGe setup with fully installed cryogenic system, lock, and a scaffold with a working plattform.

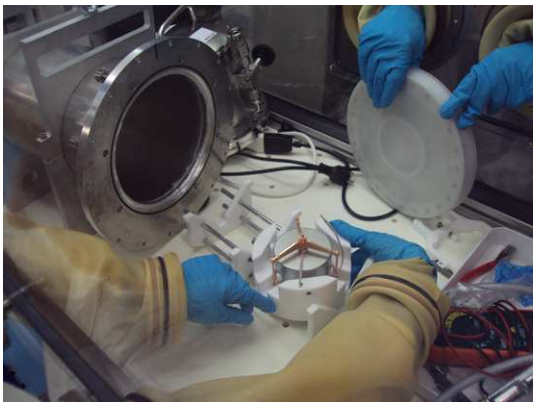

Figure A.31: The BEGe detector in a clean-bench, being prepared for transfer in the transportation lock (on the left).

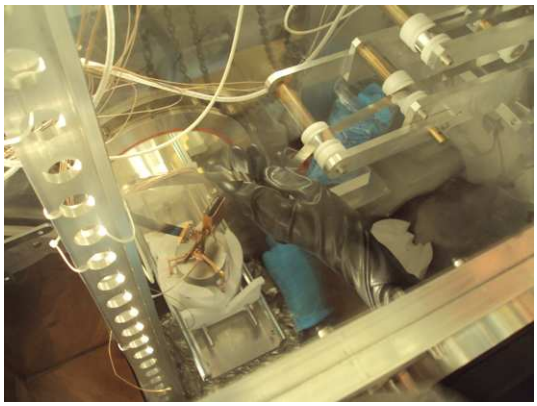

Figure A.32: A view into the main lock, while preparing the detector string of BEGe for submersion into the cryostat.

Figure A.33: The electronics of the DAQ system for PMT measurements.

Figure A.34: The *Corno Grande* mountain; part of the cosmic-ray shielding of the LNGS underground facility.

Appendix B

The ^{238}U decay chain

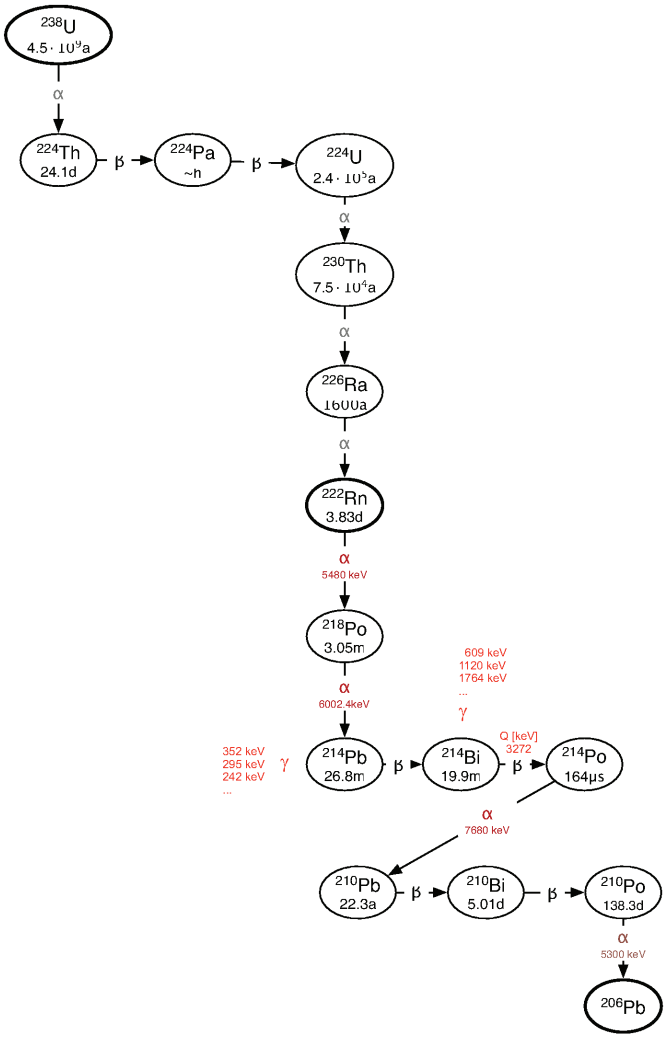

Figure B.1: A simplified version of the natural ^{238}U decay chain. Background relevant gamma lines are displayed in red colour [36].

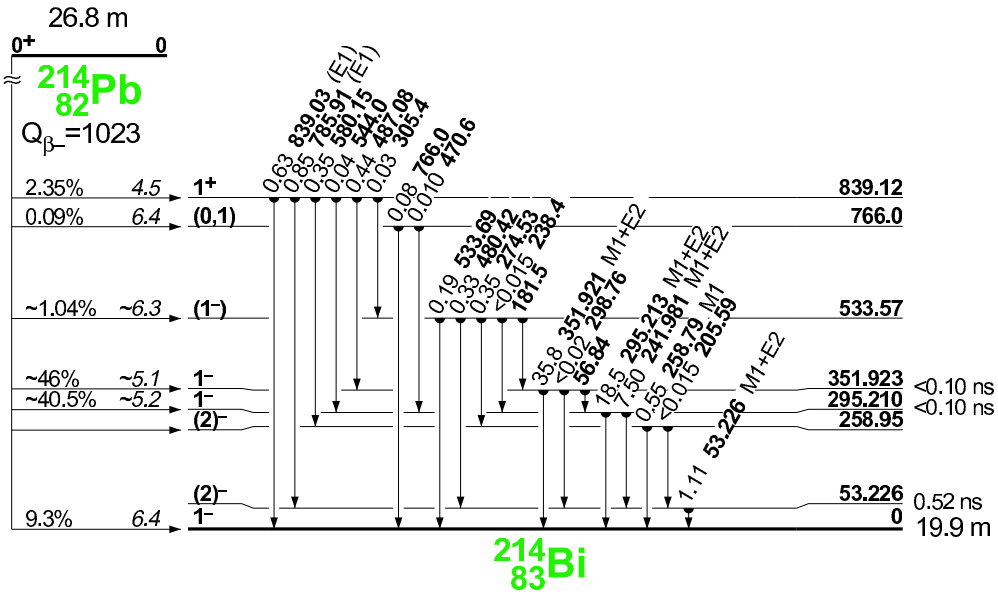

Figure B.2: The decay scheme of ^{214}Pb [72].

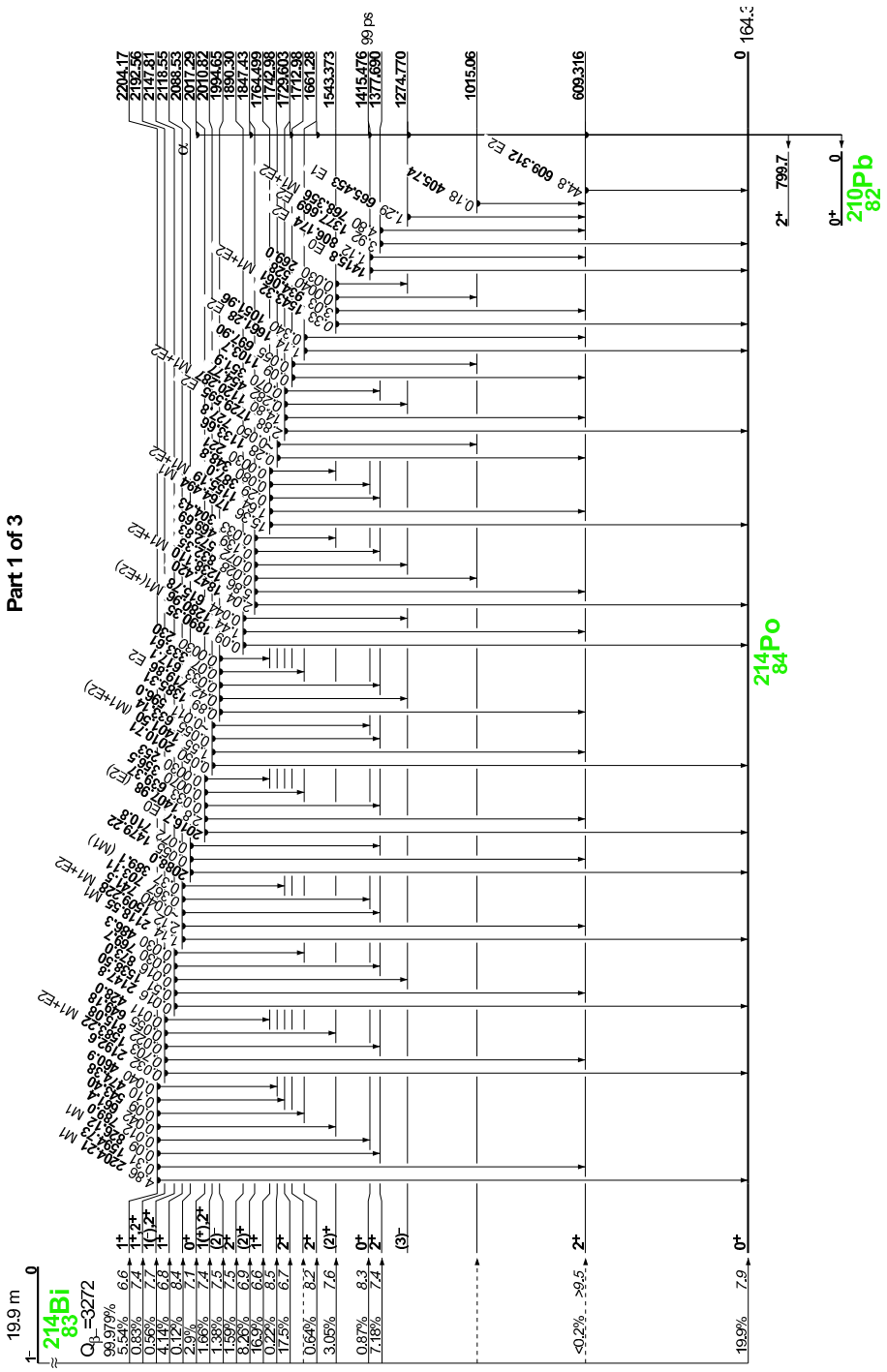

Figure B.3: The decay scheme of ^{214}Bi, part 1 of 3 [72].

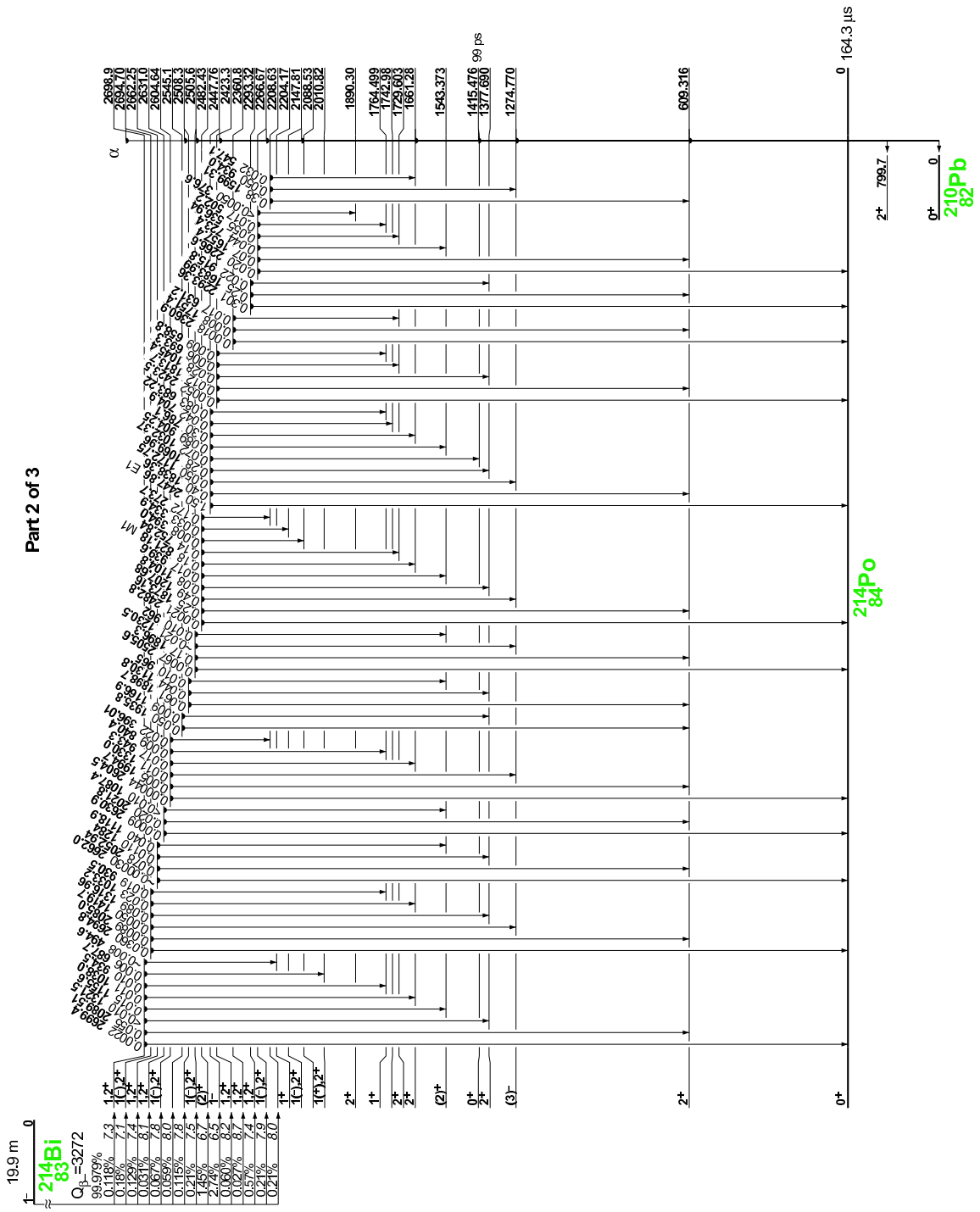

Figure B.4: The decay scheme of ^{214}Bi, part 2 of 3 [72].

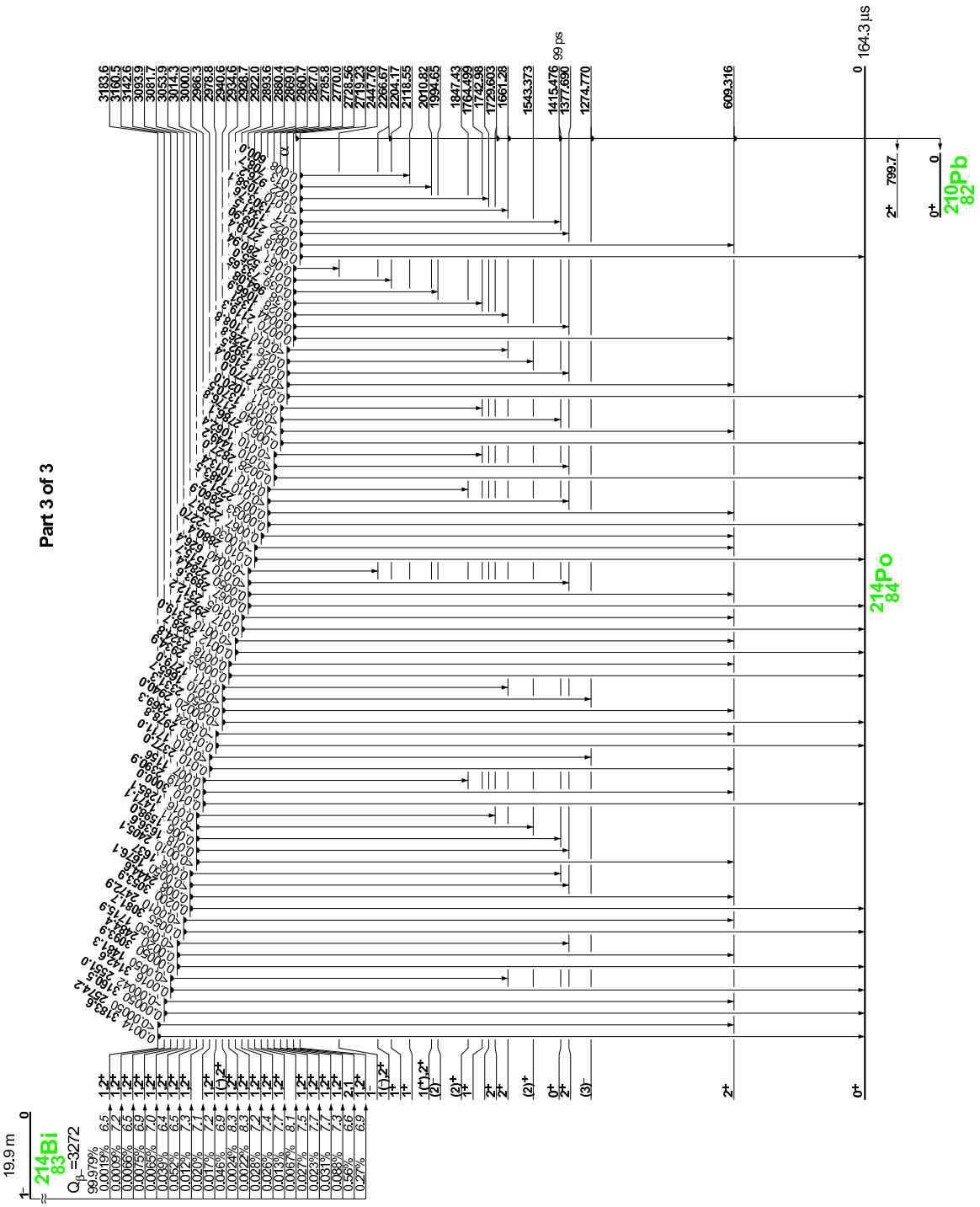

Figure B.5: The decay scheme of ^{214}Bi, part 3 of 3 [72].

Appendix C

The ^{228}Th decay chain

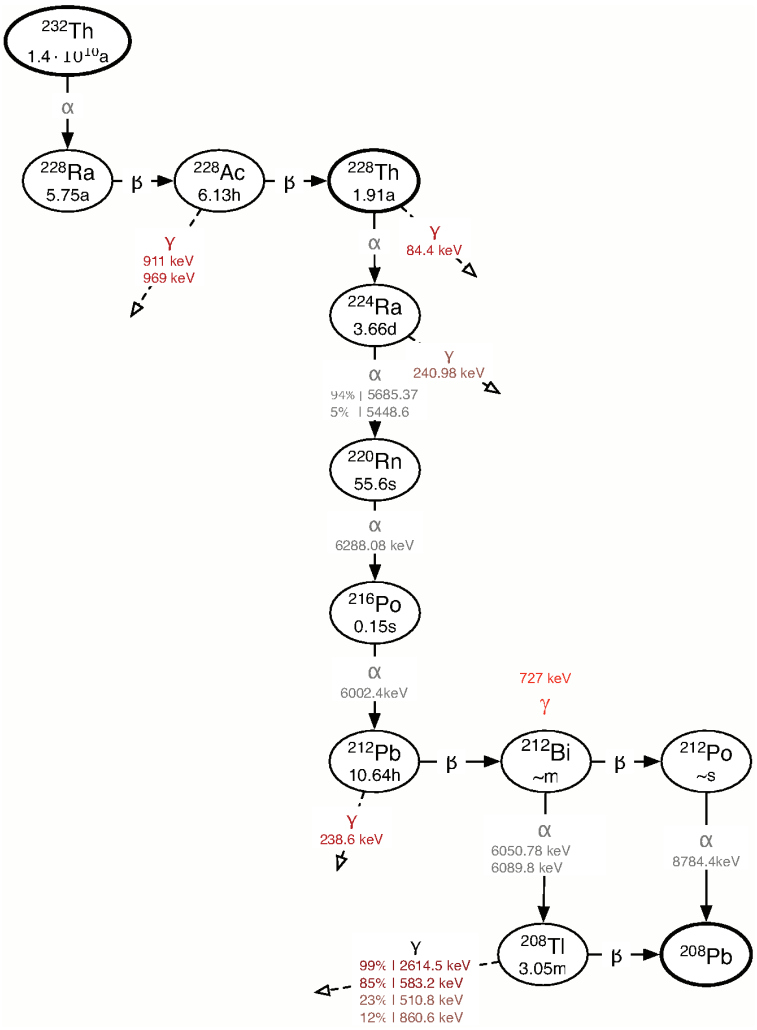

Figure C.1: The natural ^{232}Th decay chain. Background relevant gamma lines are displayed in red colour [36].

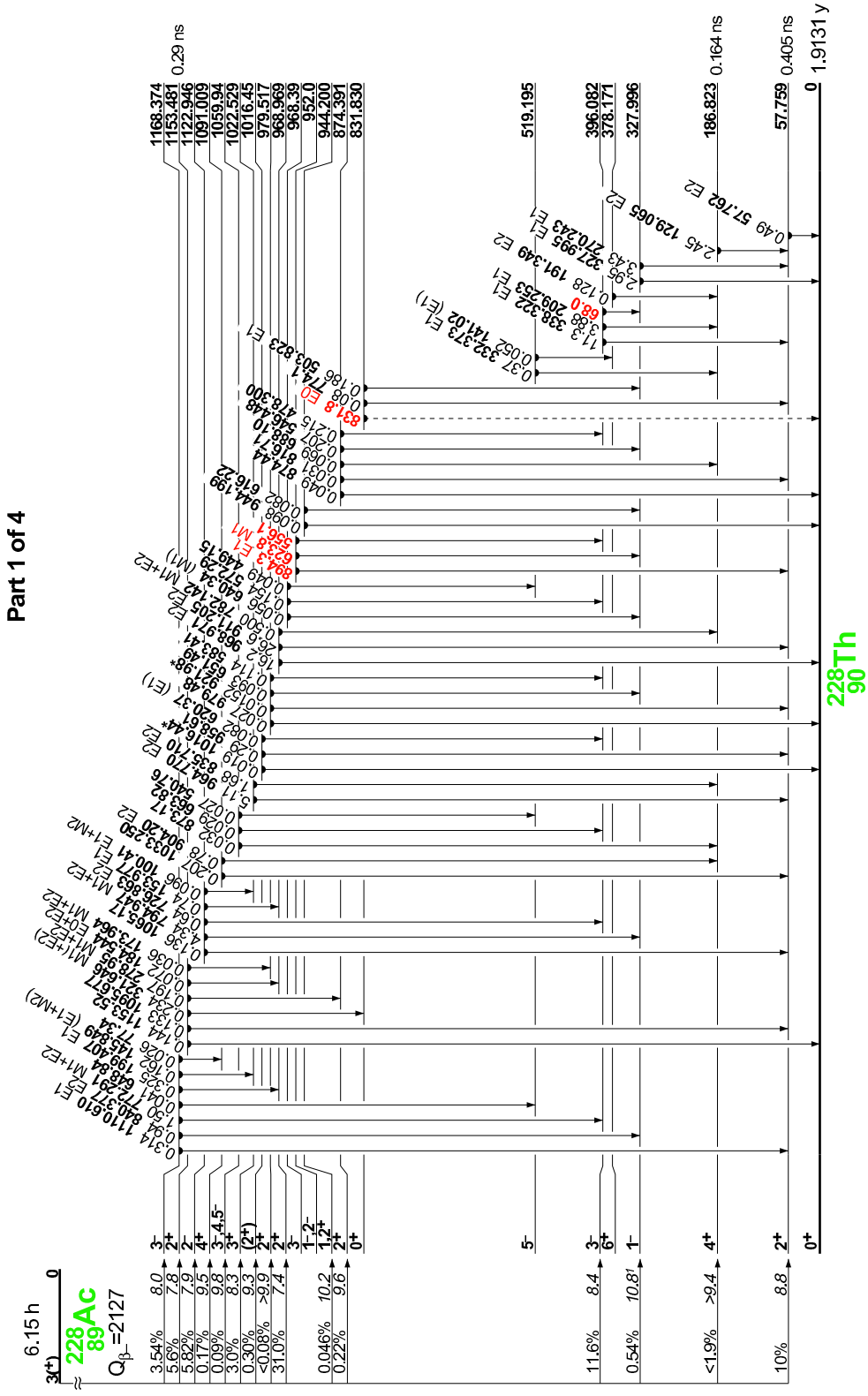

Figure C.2: The decay scheme of ^{228}Ac, part 1 of 4 [72].

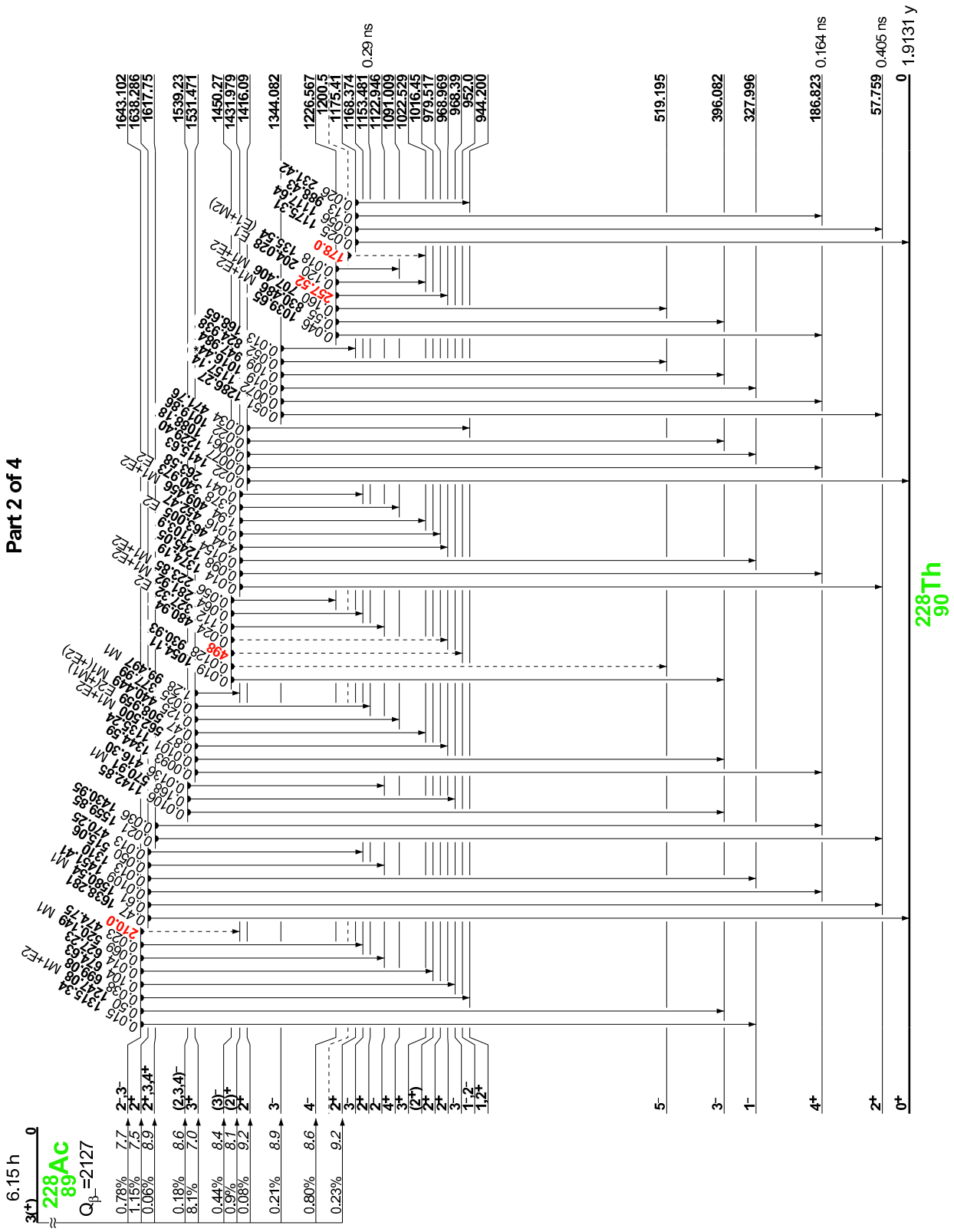

Figure C.3: The decay scheme of ^{228}Ac, part 2 of 4 [72].

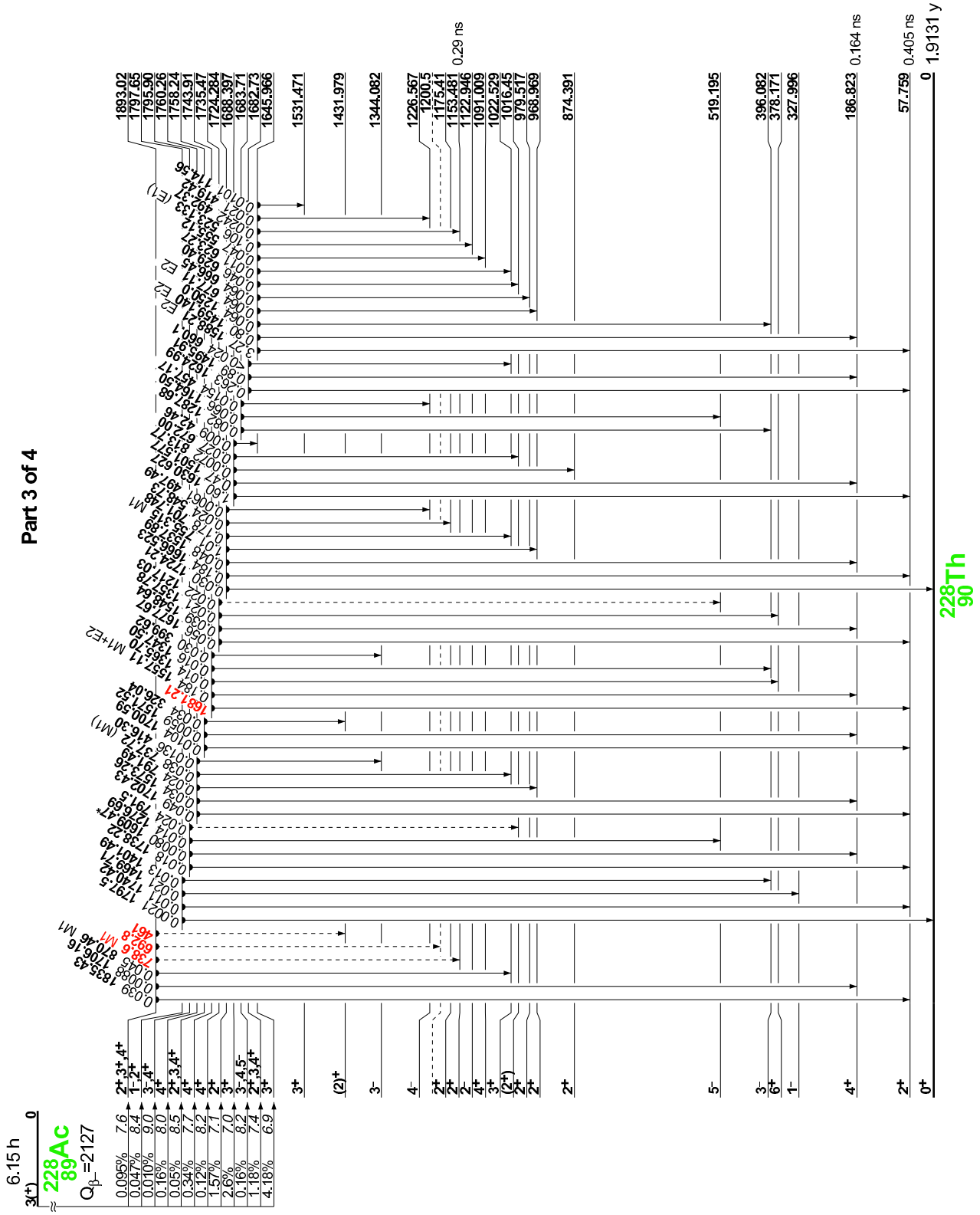

Figure C.4: The decay scheme of ^{228}Ac, part 3 of 4 [72].

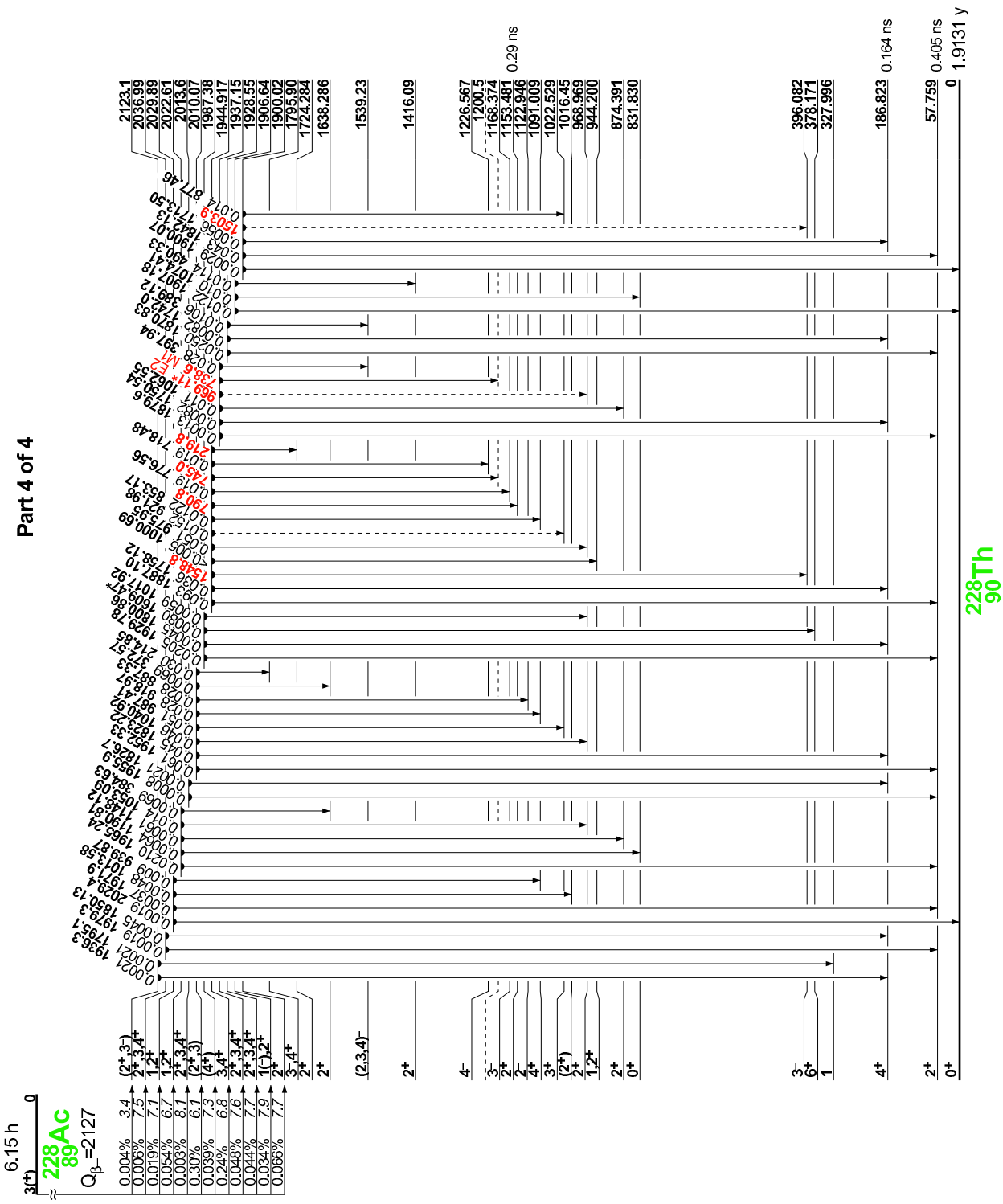

Figure C.5: The decay scheme of ^{228}Ac, part 4 of 4 [72].

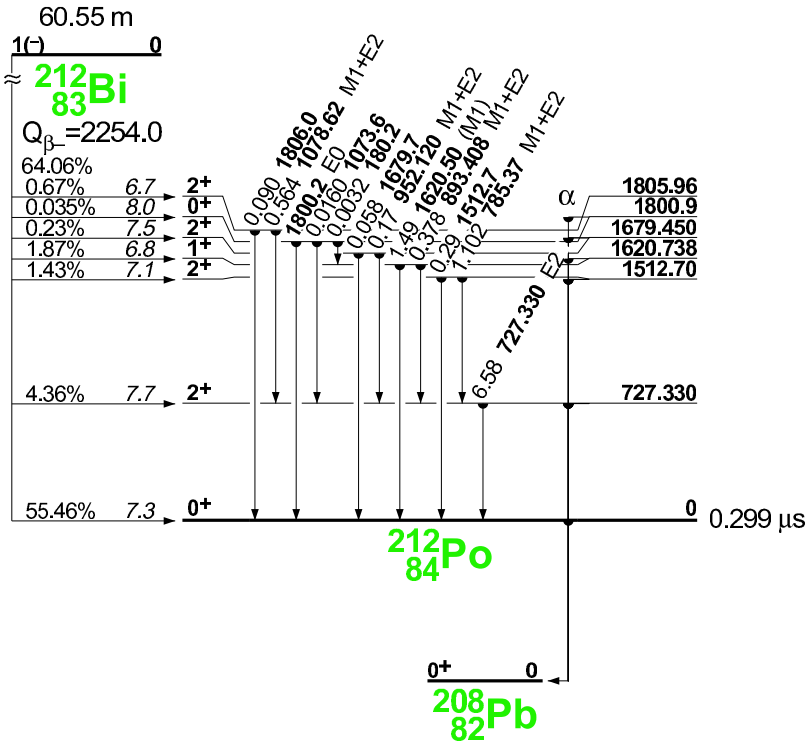

Figure C.6: The decay scheme of ^{212}Bi [72].

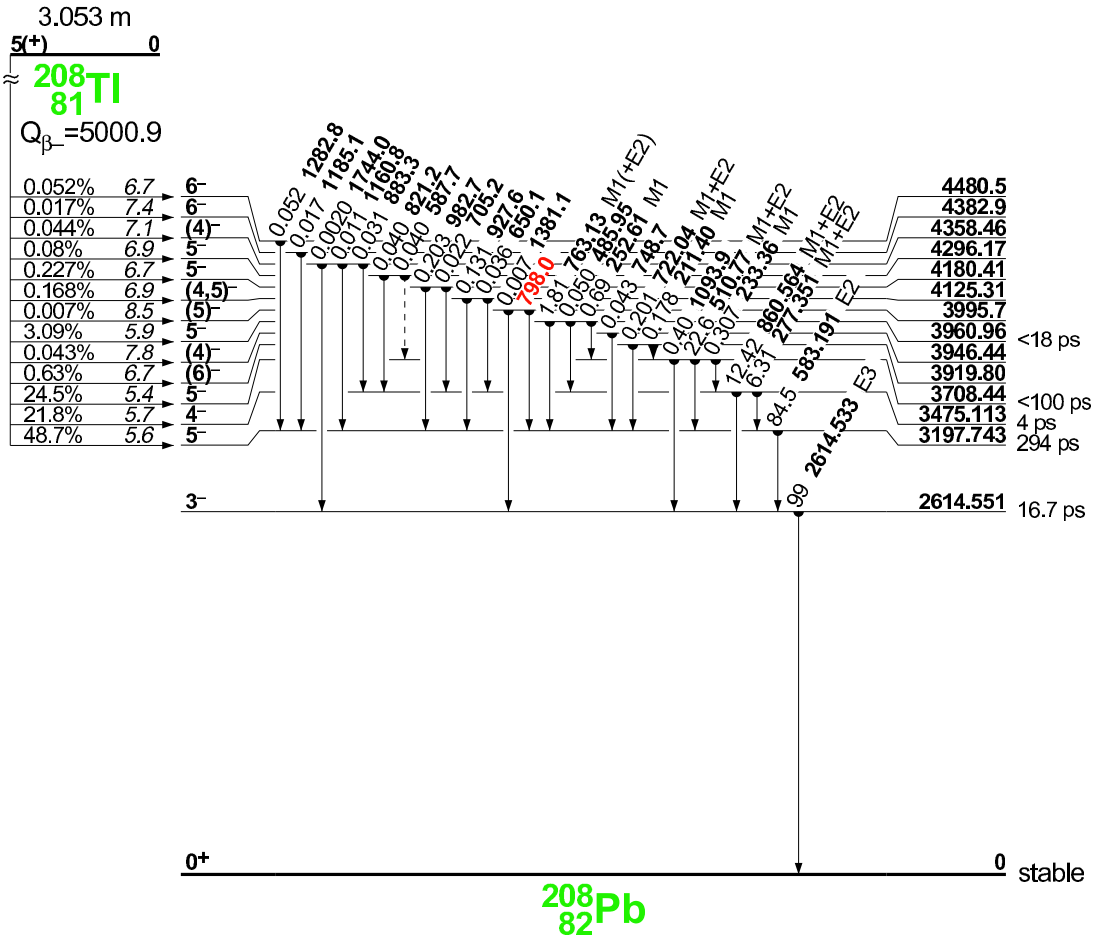

Figure C.7: The decay scheme of ^{208}Tl [72].

Bibliography

[1] F. Reines, C. L. Cowan et al., *Detection of the free neutrino: A confirmation*, Science, 124 (1956), 103, 1956

[2] R. Davis, D. S. Harmer, K. C. Hoffman, *Search for neutrinos from the sun*, Phys. Rev. Lett., 20 (1968), 1205-1209, 1968

[3] J. N. Bahcall, M. H. Pinsonneault, *What do we (not) know theoretically about solar neutrino fluxes?*, Phys. Rev. Lett., 92 (2004), 121301, 2004

[4] B. T. Cleveland et al., *Measurement of the solar electron neutrino flux with the homestake chlorine detector*, Astrophys. J., 496 (1998), 505-525, 1998

[5] Y. Fukuda, T. Hayakawa, K. Inoue et al., *Solar neutrino data covering solar cycle 22*, Phys. Rev. Lett., 77 (1996), no. 9, 1683-1686, 1996

[6] W. Hampel et al., for the GALLEX collaboration, *GALLEX solar neutrino observations: results for GALLEX*, IV. Phys. Lett. B, 447 (1999), 127-133, 1999

[7] M. Altmann et al., for the GNO collaboration, *GNO Solar neutrino observations: results for GNO*, I. Phys. Lett. B, 490 (2000), 16-26, 2000

[8] J. N. Abdurashitov et al., for the SAGE collaboration, *Measurement of the solar neutrino capture rate by SAGE and implications for neutrino oscillations in vacuum*, Phys. Rev. Lett., 83 (1999), 4686-4689, 1999

[9] R. Becker-Szendy, C. B. Bratton, D. Casper et al., *Electron- and muon-neutrino content of the atmospheric flux*, Phys. Rev. D, 46 (1992), no. 9, 1992

[10] H. Gallagher, *Experimental Evidence for Atmospheric Neutrino Oscillations: MACRO, Soudan 2 and the Future*, Nuclear Physics B - Proceedings Supplements, 143 (2005), 79-86, 2005

[11] B. Pontecorvo, *Mesoniums and antimesoniums*, J.Exp.Theoret.Phys., 33 (1957), 549, English translation: Sov.Phys.-JETP 6 (1958) 429, 1957

[12] SNO Collaboration, *Direct Evidence for Neutrino Flavor Transformation from Neutral-Current Interactions in the Sudbury Neutrino Observatory*, arXiv:nucl-ex/0204008v2, 2002

[13] Y. Fukuda et al., for the Super-Kamiokande collaboration, *Evidence for Oscillation of Atmospheric Neutrinos*, Phys. Rev. Lett. 81 (1998) 1562-1567, 1998

[14] The KamLAND Collaboration, *Measurement of neutrino oscillation with KamLAND: Evidence of spectral distortion*, Phys. Rev. Lett. 94 (2005) 081801, 2005

[15] M. H. Ahn et al., for the K2K collaboration, *Measurement of Neutrino Oscillation by the K2K Experiment*, Phys. Rev. D 74 (2006) 072003, 2006

[16] P. Adamson et al., *Measurement of neutrino oscillations with the MINOS detectors in the NuMI beam*, Phys. Rev. Lett. 101 (2008) 131802, 2008

[17] Z. Maki, M. Nakagawa, S. Sakata, *Remarks on the Unified Model of Elementary Particles*, Progress of Theoretical Physics, 28 (1962), no. 5, 870-880, 1962

[18] L. Wolfenstein, *Neutrino oscillations in matter*, Phys. Rev. D, 17 (1978), 2369-2374, 1978

[19] S. P. Mikheyev, A. Y. Smirnov, *Resonance enhancement of oscillations in matter and Solar Neutrino spectroscopy*, Soviet Journal of Nuclear Physics, 42 (1985), 913-917, 1985

[20] M. Apollonio et al., *Limits on Neutrino Oscillations from the* CHOOZ *Experiment*, Phys. Lett. B 466 (1999) 415, 1999

[21] C. Kraus et al., *Final results from phase II of the Mainz neutrino mass searching tritium β-decay*, The European Physical Journal C, 40 (2005), no. 4, 447-468, 2005

[22] V.M. Lobashev, *Study of the tritium beta-spectrum in experiment Troisk-ν-mass*, Progress in Particle and Nuclear Physics, 48 (2002), 123-131, 2002

[23] C. L. Bennett, M. Halpern, G. Hinshaw et al., *First year wilkinson microwave anisotropy probe (wmap) observations: Preliminary maps and basic results*, The Astrophysical Journal, 148 (2003), 2003

[24] D. N. Spergel, L. Verde, H. V. Peiris et al., *First year wilkinson microwave anisotropy probe (wmap) observations: Determination of cosmological parameters*, The Astrophysical Journal, 148 (2003), 175, 2003

[25] R. N. Mohapatra, G. Senjanovic, *Neutrino mass and spontaneous parity nonconservation*, Phys. Rev. Lett., 44 (1980), no. 14, 912-915, 1980

[26] W. Buchmuller, R. D. Peccei, T. Yanagida, *Leptogenesis as the origin of matter*, Annual Review of Nuclear and Particle Science, 55 (2005), 311.
URL `http://www.citebase.org/abstract?id=oai:arXiv.org:hep-ph/0502169`

[27] S. R. Elliott, P. Vogel, *Double beta decay*, Annual Review of Nuclear and Particle Science, 52 (2002), no. 1, 115-151, 2002

[28] W. Maneschg, A. Merle, W. Rodejohann, *Statistical analysis of future neutrino mass experiments including neutrino-less double beta decay*, 2009 EPL 85 51002, 2009

[29] H. V. Klapdor-Kleingrothaus et al., *Latest results from the Heidelberg-Moscow double beta decay experiment*, Euro. Phys. J. A 12 (2001) 147-154, 2001

[30] C. E. Aalseth et al., for the IGEX Collaboration, *Recent results of* IGEX ^{76}*Ge double-beta decay experiment*, Phys. of Atomic Nuclei 63 (2000) 1225, 2000

[31] H. V. Klapdor-Kleingrothaus, I.V. Krivosheina, O. Chkvorets, *Search for neutrinoless double beta decay with enriched* ^{76}*Ge in Gran Sasso 1990-2003*, Physics Letters B, 586 (2004), 198-212, 2004

[32] C. E. Aalseth et al., *Comment on 'Evidence for Neutrinoless double beta decay'*, Mod. Phys. Lett. A17:1475-1478, 2002

[33] GERDA collaboration, GERDA *The GERmanium Detector Array for the search of neutrinoless* $\beta\beta$ *decays of* ^{76}*Ge at LNGS*, 2004
URL `http://www.mpi-hd.mpg.de/gerda/public/`

[34] H. V. Klapdor-Kleingrothaus et al., *Latest results from the HEIDELBERG-MOSCOW double beta decay experiment*, Eur. Phys. J. A 12, 147-154, 2001

[35] Laboratori Nazionali del Gran Sasso,
URL `http://www.lngs.infn.it/`

[36] P. Peiffer, *Liquid argon as active shielding and coolant for bare germanium detectors: A novel background suppression method for the* GERDA $0\nu\beta\beta$ *experiment*, PhD-thesis, Universität Heidelberg, 2007

[37] P. Peiffer et al., *Pulse shape analysis of scintillation signals from pure and xenon-doped liquid argon for radioactive background identification*, JINST 3 P08007, 2008

[38] S. Schönert et al., *Pulse shape analysis of scintillation signals from pure and xenon-doped liquid argon for radioactive background identification*, JINST 007P-0608, 2008

[39] GERDA collaboration, GERDA *Technical Proposal*, version 0.1, 2005
URL `http://www.mpi-hd.mpg.de/gerda/public/`

[40] C. Motta et al., *LLBF: LENS prototype at Gran Sasso*, Nucl. Phys. B (Proc. Suppl.) 118 (2003) 451

[41] I. Barabanov, V. Gurentsov, *MC simulations of the background index of LArGe*, GSTR-07-012, internal GERDA report, 2007

[42] G. Heusser, M. Laubernstein, H. Neder, *Low-level germanium gamma-ray spectrometry at the* μ*Bq/kg level and future developments towards higher sensitivity*, Proceedings of International Conference on Isotopes in Environmental Studies - Aquatic Forum, 2004

[43] G. Heusser, *Studies of* γ*-ray background with a low level germanium spectrometer*, Nuclear Instruments and Methods in Physics Research B58 (1991) 79-84, 1990

[44] G. Zuzel, *LArGe safety and operational manual*, internal GERDA document, 2010

[45] H.E.S.S. colaboration, F. Aharonian et al., *Calibration of cameras of the H.E.S.S. detector*, Astroparticle Physics, 22 (2004), 109.
URL `http://www.citebase.org/abstract?id=oai:arXiv.org:astro-ph/0406658`

[46] D. Budjáš, *Germanium detector studies in the framework of the* GERDA *experiment*, PhD-thesis, Universität Heidelberg, 2009

[47] M. Barnabé Heider, D. Budjáš, K. Gusev, S. Schönert, *Operation and performance of a bare broad-energy germanium detector in liquid argon*, JINST 5 P10007, 2010

[48] S. Riboldi et al., *A low-noise charge sensitive preamplifier for Ge spectroscopy operating at cryogenic temperature in the Gerda experiment*, Proceedings for the IEEE-NSS conference, Knoxville (TN), USA, 2010

[49] M. Barnabé Heider, *Performance and stability tests of bare high purity germanium detectors in liquid argon for the GERDA experiment*, PhD-thesis, Universität Heidelberg, 2009

[50] S. Schönert et al. for the GERDA collaboration, GERDA *Progress report to the LNGS scientific committee*, LNGS-EXP 33/05 add. 11/10, 2010
URL `http://www.mpi-hd.mpg.de/gerda/public/`

[51] MIZZI Computer Software GmbH
URL `www.mizzi-computer.de`

[52] A. Hitachi, T. Takahashi, T. Hamada et al. *Scintillation response of liquid argon to fission fragments*, Phys. Rev. B, 23 (1981), no. 09, 4779-4781, 1981

[53] S. Kubota, M. Hishida, M. Suzuki et al. *Dynamical behavior of free electrons in the recombination process in liquid argon, krypton, and xenon*, Phys. Rev. B, 20 (1979), no. 8, 3486-3496, 1979

[54] B. Raz, J. Jortner, *Wannier type impurity excited states in liquid rare gases*, Chem. Phys. Lett. 4 (1970) 511., 1970

[55] C. Amsler et al., *Luminescence quenching of the triplet excimer state by air traces in gaseous argon*, JINST 3 P02001, 2008

[56] M. Suzuki, J. Ruan, S. Kubota, *Time dependence of the recombination luminescence from high-pressure argon, krypton and xenon excited by alpha particles*, Nucl. Instr. Meth. 192 (1982) 565

[57] T. Doke, A. Hitachi, J. Kikuchi et al., *Absolute scintillation yields in liquid argon and xenon for various particles*, Jpn. J. Appl. Phys., 41 (2002), 1538-1545, 2002

[58] M. Suzuki, *Recombination luminescence from ionization tracks produced by alpha particles in high pressure argon, krypton and xenon gases*, Nucl. Instr. Meth. A 215 (1983) 345, 1983

[59] M. J. Carvalho, G. Klein, *Alpha-particle induced scintillation in dense gaseous argon: emission spectra and temporal behaviour of its ionic component*, Nucl. Instr. and Meth. 178 (1980) 469, 1980

[60] A. Hitachi et al., *Effect of ionization density on the time dependence of luminescence from liquid argon and xenon*, Phys.Rev.B 27 (1983) 5279, 1983

[61] T. Doke et.al., *Let dependence of scintillation yields in liquid Argon*, Nucl. Instrum. Meth. A 269 (1988) 291., 1988

[62] P. Laporte et al., *Argon, Krypton and Xenon excimer luminescence: From the dilute gas to the condensed phase*, J. Chem. Phys. 91 (1989) 1469, 1989

[63] C. Amsler et al., *Luminescence quenching of the triplet excimer state by air traces in gaseous argon*, arXiv:0708.2621v1 [physics.ins-det], August 2007

[64] WArP collaboration, *Effects of Nitrogen contamination in liquid Argon*, arXiv:0804.1217v1 [nucl-ex], April 2008

[65] WArP collaboration, *Oxygen contamination in liquid Argon: combined effects on ionization electron charge and scintillation light*, arXiv:0804.1222v1 [nucl-ex], April 2008

[66] T. Pollmann, *Pulse shape discrimination studies in a liquid Argon scintillation detector*, diploma thesis, Universität Heidelberg, 2007

[67] S. Schönert, private communication, March 2010

[68] M. Agostini, *Characterization of a Broad Energy Germanium detector through advanced pulse shape analysis techniques for the* GERDA *double-beta decay experiment*, Universitá degli Studi di Padova, 2009

[69] M. Agostini et al., *Signal modeling of high-purity Ge detectors with a small read-out electrode and application to neutrinoless double beta decay search in* ^{76}Ge, 2010
URL `http://arxiv.org/PS_cache/arxiv/pdf/1012/1012.4300v1.pdf`

[70] D. Budjáš et al., *Pulse shape discrimination studies with a Broad-Energy Germanium detector for signal identification and background suppression in the* GERDA *double beta decay experiment*, JINST 4:P10007, 2009

[71] J. Stein, F. Scheuer, W. Gast, A. Georgiev, *X-ray detectors with digitized preamplifiers*, B 113 (1996) 141-145

[72] R. B. Firestone, *Table of Isotopes*, Wiley-Interscience, Ebook, 1996

[73] R. Henning et al.: *The MaGe Simulation Package for the Majorana and Gerda Experiments*, http://www.lbl.gov/nsd/resources/annualreportcontributionsall/henning3.pdf

[74] Particle Data Group, *Review of Particle Physics*, Regents of the University of California, 2010
URL `http://pdg.lbl.gov`

[75] GERDA collaboration, *The* GERDA *experiment*, 2011
URL `http://www.mpi-hd.mpg.de/GERDA/`

[76] H. V. Klapdor-Kleingrothaus et al., *Data acquisition and analysis of the* ^{76}Ge *double beta experiment in Gran Sasso 1990-2003*, Nucl. Intr. Meth. A522, 371-406 (2004)

[77] A. S. Barabash et al., *Liquid Argon Ionization Detector for Double Beta Decay Studies*, arXiv:nucl-ex/0309001v1, 2003

[78] ISO 11929-7, *Determination of the Detection Limit and Decision Threshold for Ionising Radiation Measurements – Part 7: Fundamentals and General Applications*, ISO, Geneva, 2005

[79] S. Schönert, private communication, February 2011

[80] A. J. Peurrung et al., *Expected atmospheric concentration of* ^{42}Ar, Nuclear Instruments and Methods in Physics Research A 396 (1997) 425-426, 1997

[81] I. Barabanov, A. Klimenko, private communication, February 2011

[82] H. Primakoff, S. P. Rosen, *Double Beta Decay*, Rep. Progr. Phys. 22:121, 1959

[83] A. Smolnikov, private communication, February 2011

Acknowledgements

This thesis is the outcome of almost four years of work in the labs of Mpik and Lngs. During this time I worked, suffered, and celebrated together with several people on this project, and I was supported by many more, all of whom I wish to thank here.

My sincere thanks go to Prof. Wolfgang Hampel, who agreed to become my doctoral adviser, and who has always backed me up when I needed his support. And with him, I thank Prof. Wolfgang Krätschmer, both for their generous patience in the past weeks.

I thank my supervisor Stefan Schönert for giving me the opportunity to work in this auspicious project. His guidance and countless ideas helped me throughout the work, without him this thesis would not have been possible.

The LArGe team has been the backbone of the project, who build and operated the detector in numberless hours at Heidelberg and Gran Sasso. I am very grateful to have worked with so many skilled and persistent people: Anatoly Smolnikov, Stefan Schönert, Albert Gangapshev, Grzegorz Zuzel, Herbert Strecker, Michael Reisfelder, Dušan Budjáš, Matteo Agostini, Marik Barnabé Heider, Konstantin Gusev, Alexander Klimenko, Alexey Lubashevskiy, and Christian Bauer. My special gratitude goes to Anatoly, for sharing his expertise, advise, and kindness with me throughout the years. And I thank Peter Peiffer, for preparing the ground and introducing me to the Mini-LArGe work.

I wish to thank my division at Mpik, in which I found great colleagues and lasting support. Here my special thanks go to our director Manfred Lindner and spirited Anja Berneiser, for their significant share in creating such excellent working conditions. I thank Ute Schwan for her frequent support in the chemistry lab, and Josefa Oehm for entrusting me with her brandnew cleanroom. In addition, I thank Hardy Simgen, Erich Borger, Florian Kaether, Erhard Burkert, Daniel Schmidt and all others, who have advised and helped me with the various issues of the daily experimentalist's life. In recognition of their help and support I would like to mention my proficient colleagues from the various workshops at Mpik, in particular Volker Mallinger, Theo Apfel, Klaus Jänner, Jörg Baumgart, and the people from the 'Fuchs workshop', whose storehouse we blocked for too many weeks.

Furthermore, I like to extend my thanks to the Gerda collaboration and the staff at Lngs for becoming my second 'working home' for a long and invigorating time. Particularly helpful for my work at Gran Sasso were Bernhard Schwingenheuer, Matthias Junker, Matthias Laubenstein, Marco Balata, Stefano Nisi, and many more.

Lastly, I owe my loving gratitude to my wife Silvina Martin. Her caring support und understanding gave me strength throughout the most difficult times of this thesis, for which she has renounced a lot. A big thank also goes to my family, to my mother Edda and my brother Frank, who have encouraged me unremittingly throughout the years. Thank You all!